Circularly Polarized Antennas for GNSS Applications

by

Umniyyah Ulfa Hussine

Thesis submitted in accordance with the requirements for the award of the degree of
Doctor of Philosophy of the University of Liverpool

January 2021

Abstract

Global navigation satellite system (GNSS) is developing rapidly. Modern GNSS technology is facing challenges for researchers to explore. One hot topic is the multi-system GNSS device. The motivation for the antenna designers is to miniaturize the size of the antenna and meanwhile keep its standard performance. It is a challenging task for an antenna array design to achieve a wide bandwidth, high gain, small size, good coverage, and simple fabrication technique all at the same time. This thesis develops several different novel compacts, high gain, and wide bandwidth circularly polarized (CP) antenna capable of providing wide coverage for GNSS frequency bands from 1.16 GHz to 1.6 GHz to cover the GPS L1-L5 bands, GLONASS G1, G2 and G3 as well as the Galileo E5a, E5b, E6, and E1bands.

In the first part of the thesis, the author proposed a new broadband antenna to cover the GPS L1-L5 bands, GLONASS G1, G2 and G3 as well as the Galileo E5a, E5b, E6, and E1bands. The antenna is composed of four parasitic elements that are excited by coupling with the elliptical crossed dipole in the center. By adjusting the size of the parasitic element and the edge of the dipoles, the coupling strength can be optimized. The antenna employs a single feed and two orthogonally elliptical printed dipoles. The dipoles are crossed through a 90° phase delay line of a vacant-quarter printed ring to achieve CP radiation. The main problem of an antenna equipped with a metallic reflector is often addressed by including a quarter-wavelength space between the radiating elements and the reflector to obtain optimal antenna characteristics. These can be circumvented by using an artificial magnetic conductor

(AMC) surface instead of a metallic reflector. The second contribution is the development of two novel broadband antennas using two different material of AMC substrate which is FR-4 and Rogers RT6006. By combining the crossed dipole radiators and the finite AMC surfaces, low-profile multiband CP antennas that are nearly completely matched to a single 50 Ω source and have high radiation efficiencies have been implemented. The proposed antenna has a 10-dB return loss over 1.153 – 2.36 GHz and achieves a peak realized gain of 5.86 dBi. The interesting features of the AMC-based crossed dipole antennas are not only their ability to achieve high efficiency with a low profile but also to generate additional resonances and the corresponding additional CP radiation features. These were utilized to add other operating bands or to broaden the antenna bandwidth. Jamming is the act of intentionally directing electromagnetic energy towards a communication and navigation system to disrupt or prevent signal transmission. GNSS jammers broadcast their interference signal in the frequency band used for satellite navigation. Consequently, the final contribution of the work is a novel wideband CP anti-jamming antenna array with the capability of generating multiple steerable beam directions and enables effective jammer suppression with negligible phase distortion. A 2 × 2 antenna array exhibits a wide bandwidth from 0.995-2.333 GHz and has a peak gain of 7.6 dBi. In order to have a compact system, a total antenna array miniaturization has been achieved.

Collectively, these contributions advance the state-of-the-art in GNSS adaptive antennas in terms of performance, precision, and practicality.

Acknowledgement

First of all, I thank GOD ALMIGHTY who has given me the mental and physical strength and confidence to do this work. This thesis would not have seen the light without the support and guidance of many people who are acknowledged here. I would like to express my deep gratitude to my supervisor, Professor Yi Huang for offering me this opportunity. His kind support, fruitful advice, critical discussions, and vast experience have motivated me during the whole time of my studies. I would also like to thank my second supervisor Dr. Jiafeng Zhou who has endorsed this life changing opportunity for me.

I would like to offer my personal and special thanks to my husband, Sidek Ismail and my children, Sarah, Khayra and Rayyan. I would never have succeeded without their love, tolerance, support, encouragement, and patience. You have always supported me with no expectation of a reward. Your continuous help and understanding have made my life full of love and I am grateful for everything you have done. I would also like to express my appreciation to my parents, Siti Rugayah Tibek and Hussine Hangah and my brother, Farid Ismat who have encouraged me over the years.

Thanks to all my friends here in Liverpool and also in Malaysia who had been with me in the very crucial moments of my studies and for boosting my morale. I am very grateful for all their support and effort to cheer me up.

I would also thank my brilliant and lovely colleagues and friends in the RF group for many fruitful discussions and enjoyable moments and providing such a lovely environment for research. Special thanks are also paid to Dr. Chaoyun Song for valuable advice, contribution, and collaboration in editing the published papers of this research and for the friendly support. Particular thanks should also be paid to Mark and John from the Electrical Workshop for always being very kind to me and fabricating my antennas and circuits very quickly and beautifully. Thanks to Rogers Corporation for providing us with free samples of PCB boards.

Finally, the financial support from the Ministry of Higher Education Malaysia and the University of Science Islam Malaysia (USIM) is gratefully acknowledged.

Table of Contents

List of Tables

List of Figures

List of Acronyms

AR	Axial Ratio
AMC	Artificial Magnetic Conductor
AUT	Antenna Under Test
CDMA	Code Division Multiple Access
CP	Circular Polarization
CS	Control Segment
CST	Computer Simulation Technology
DC	Direct Current
DRA	Dielectric Resonator Antenna
EM	Electromagnetic
FDMA	Frequency Division Multiple Access
FBW	Fractional Bandwidth
GEO	Geostationary Orbits
GLONASS	GLObal Navigation Satellite System
GNSS	Global Navigation Satellite Systems
GPS	Global Positioning System
HF	High Frequency
HIS	High Impedance Surface
HPBW	Half-Power Beam Width
IEEE	Institute of Electrical and Electronics Engineers
IGSO	Inclined Geosynchronous Orbits
LF	Low Frequency
LHCP	Left Hand Circularly Polarized
LNA	Low Noise Amplifier
LP	Linear Polarization
MEO	Medium Earth Orbit
OC	Operational Control Segment
PCB	Printed Circuit Board

PEC	Perfect Electric Conductor
PNT	Position, Navigation, and Timing
PPS	The Precise Positioning System
PRN	Pseudo Random Noise
PVT	Position, Velocity, and Timing
QZSS	Quasi-Zenith Satellite System
RFI	Radio Frequency Interference
RHCP	Right Hand Circularly Polarized
RX	Receiving Antenna
SAR	Specific Absorption Rate
SDR	Software-Defined Radio
SIW	Substrate Integrated Waveguide
SNR	Signal to Noise Ratio
SPS	The Standard Positioning Service
SS	Space Segment or Satellite Segment
STAP	Space-Time Adaptive Processing
SV	Satellite Vehicle
TX	Transmitting Antenna
UHF	Ultra-High Frequency
US	User Segment
VSWR	Voltage Standing Wave Ratio

List of Publications

[1] **U. U. Hussine**, Y. Huang and C. Song, “A new circularly polarized antenna for GNSS applications,” in Proc. 2017 11th European Conference on Antennas and Propagation (EUCAP), 2017, pp. 1–3.

[2] C. Song, Y. Huang and **U. U. Hussine**, “A broadband circularly polarized cross-dipole antenna for GNSS applications,” in Proc. 2015 Loughborough Antennas & Propagation Conference (LAPC), 2015, pp. 1–4.

[3] **U. U. Hussine**, O. A. Mobayode, Y. Huang and B.Liu, “A novel circularly polarized antenna for GNSS applications using optimization technique” (*to be submitted*)

CHAPTER 1:

INTRODUCTION

1.1 BACKGROUND

Since the deployment of the Global Positioning System (GPS) by the United States and a similar GLObal Navigation Satellite System (GLONASS) system by the Soviet Union around 1990 [1]–[3], GPS applications have proliferated globally, not only in the military arena but also in commercial and consumer markets. While the importance of GPS antenna relative to GPS receiver is obvious and remains, the performance and cost issues have fundamentally changed.

Application of GLONASS has been minuscule after the dissolution of the Soviet Union. The recent recovery of the Russian economy propelled by the oil boom has enabled the revitalization of GLONASS, which restarted full constellation operation in April 2011. In 2002, the European Union started to develop Galileo.

Originally targeted to start operation in 2008, Galileo suffered from years of delays due to financial and technical troubles. In 2011, its delayed plan was to have full global coverage in 2019. China began to develop Compass (Beidou) in the late 1990s, but has been fast moving in recent years, and is positioned to have a full-fledged Global Navigation Satellites System (GNSS) within a few years [4].

Additionally, GPS, GLONASS, and Compass are also being augmented by Geostationary Earth Orbit (GEO) satellites to complement their Medium Earth Orbit (MEO) satellites. Several other countries have also started their regional satellite navigation systems, such as Japan’s Quasi Zenith Satellite System (QZSS). All these satellite-based systems constitute the GNSS, with GPS, GLONASS, Galileo, and Compass being the four cornerstones with global coverage. The upcoming availability of so many satellites, and over such a wide frequency range, in GNSS constellations, as well as the move toward more unified code-division multiple-access (CDMA) approach, in the near future, will offer superior performance and lower life-cycle cost, as well as new features and capabilities. These game-changing events are also enabled by newly available low-cost software-defined radio (SDR) technologies and the unprecedented global economy. To meet the anticipated market needs, GNSS receivers covering two or more GNSS systems have been developed and deployed at fairly low costs.

1.1.1 Radio Frequency (RF) Performance Parameters of GNSS Antennas

The impact of the fundamental changes from GPS to GNSS has been recognized and taken advantage of by receiver manufacturers. Several GNSS receivers have recently shown up in the marketplace, and they can easily adapt to large future changes in GNSS waveforms since they are based on SDR technology. In the commercial world, SDR development and application have been growing rapidly since about 2000. On the other hand, SDR antenna development has not had such success as the receiver. In this context, RF performance parameters of GNSS receive antennas will be discussed, highlighting changes from those for conventional GPS.

1.1.1.1 Operating Frequencies and Bandwidths

Table 1.1 displays signals and constellations of the four major GNSS systems: GPS, GLONASS, Galileo, and Compass, with the data on maximum bandwidths largely derived from [4] and [5] for interoperability issues. GNSS spectra are spread densely across 1146 to 1616 MHz, covering a frequency bandwidth of 470 MHz. Obviously, future GNSS antennas will strive to cover more bands and constellations like antennas driven by the receivers.

Since the receivers will be increasingly more able to cover the entire GNSS spectrum and take advantage of it, it is desirable and sometimes necessary that their antennas' operating frequencies and bandwidths be consistent with those of the receivers. Additionally, large bandwidths are needed to mitigate detuning due to changes in the antenna’s installation environment. In practical applications, there is also a growing trend for GNSS antennas toward multifunction that covers not only GNSS but also some satellite communications such as satellite radio, Iridium, etc.

Table 1.1: Frequency and Constellations of GNSS Systems

	GPS	**GLONASS**	**Galileo**	**COMPASS / Beidou**
Country	USA	Russia	European Union	China
Constellation	24 MEO	24 MEO	30 MEO	27 MEO 5 GEO 3 IGSO
Coding	CDMA	FDMA / CDMA	CDMA	CDMA
Carrier Frequency (MHz)	L1: 1575.420 L2: 1227.600 L5: 1176.450	G1: 1602.000 + k × 0.5625* G2: 1246.000 + k × 0.4375* G3: 1204.704 + k × 0.4230*	E1: 1575.420 E5a: 1176.450 E5b: 1207.140 E5: 1191.795 E6: 1278.750	B1: 1559.052~1591.788 B2: 1162.220~1217.370 B3: 1250.618~1286.423

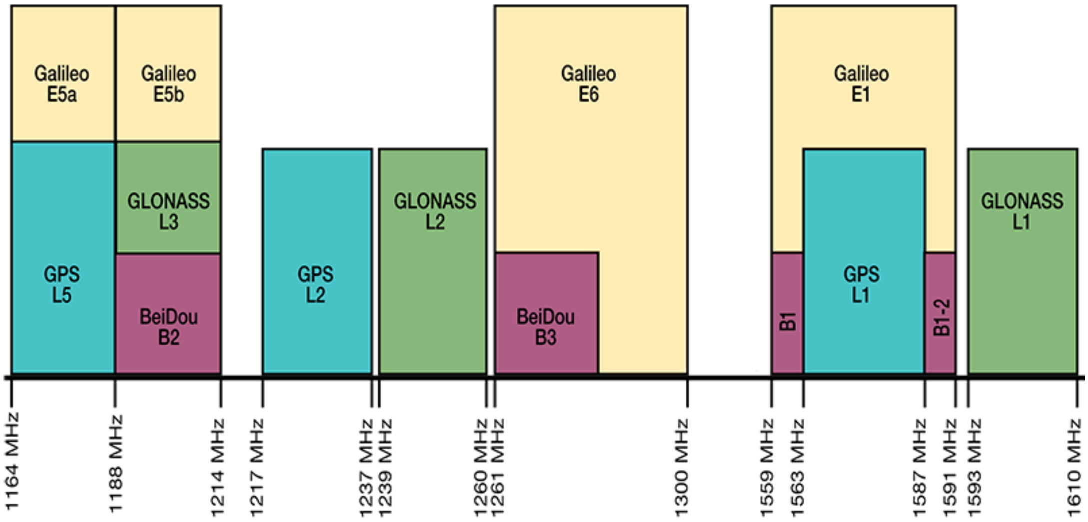

Figure 1.1: GNSS Frequency Bands [6].

These satellite systems are fundamentally similar, and one can typically develop technology that generally applies to all of them. The research presented in this work, which focuses on the receiver antenna and its associated signal processing that applicable to any GNSS system so long as the antenna and antenna electronics are designed for the required frequencies. In this work, the term “GNSS antenna” will be frequently used to refer to an antenna designed for any one or multiple satellite navigation systems. The frequency bands for these GNSS systems and performance requirements of a GNSS antenna prototype are shown in Figure 1.1 [6] and Table 1.2 respectively.

Table 1.2: Performance Requirements of a GNSS Antenna Prototype

Parameter	**Requirement**
Resonant Frequency or Operational Frequency	E1 – E6; L1, L2, L5; G1 – G3; B1 – B3 1.16 to 1.30 GHz and 1.52 to 1.61 GHz GPS, GLONASS, Galileo and BeiDou/COMPASS
Bandwidth (VSWR < 2:1)	At least 103 MHz on L1 band
Polarization	Right Hand Circular Polarization (RHCP)
Axial Ratio	0 dB to 3-dB at boresight
Gain Variation	Less than 15 dB from Zenith to 10° elevation angle
Zenith Gain	Greater than 0 dBic (desired)
Desired to Undesired Ratio (D/U)	Minimum 20 dB at 45° Elevation angle

1.1.1.2 Radiation Pattern and Polarization

Polarization can be defined as the track of the electric field vector for travelling EM waves. An antenna can be classified as linear polarization (LP), elliptical polarization (EP) and circular polarization (CP). Right hand circular polarization (RHCP) and left-hand circular polarization (LHCP) are two types of circular polarization. The axial ratio (AR) can be defined to measure the level of CP. The AR is 0 dB for a perfect CP antenna. Usually, when the AR is less than 3 dB, the antenna is a CP antenna.

Figure 1.2 depicts two ideal elevation gain patterns, one before and one after 2010, to highlight the fundamental changes. The polar patterns are in spherical and rectangular coordinates, with the z-axis pointing to the zenith. The gain pattern optimizes gain and coverage for satellites over $0° < \theta < \theta_c$ and mitigates problems due to multipath from satellite platform, ionosphere, troposphere, and platform environment, as well as interferences and noises over $\theta_c < \theta < 180°$. The sharp turn at elevation “cutoff angle” θ_c is a major design difficulty; a real-world GNSS antenna generally has a smooth cardioid pattern with hemispherical coverage. θ_c is a crucial parameter varying between applications but is moving higher toward the zenith with the advent of GNSS [6].

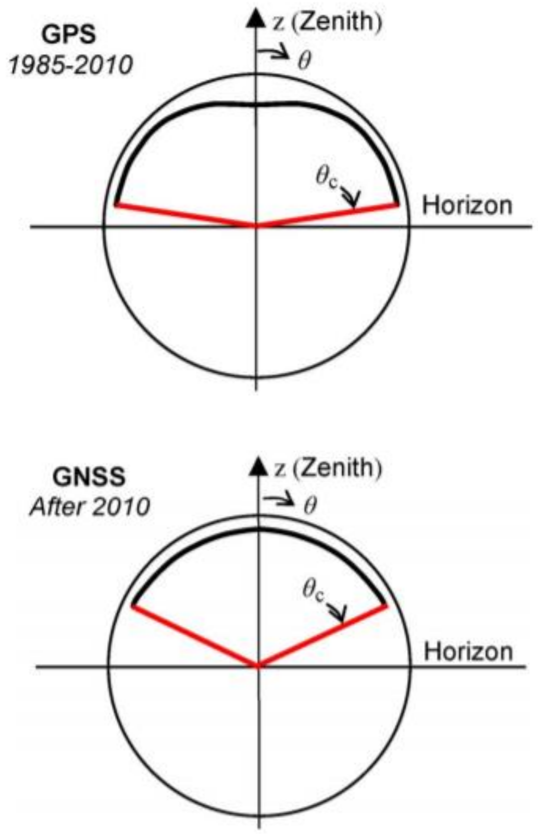

Figure 1.2: Ideal antenna gain patterns for GPS antennas (1985–2010) and GNSS antennas (after 2010) [6].

A minimum antenna gain, G_{min} in RHCP is desired over angles $\theta < \theta_c$. Generally, G_{min} > -10 dBic in RHCP is needed to provide sufficient signal-to-noise ratio (SNR) for detection. But this low gain requirement can be further relaxed by up to 10 dB or so by using various software and hardware techniques for applications with the lower precision requirement. At elevation angles below θ_c, i.e., 180° > θ > θ_c, a vanishingly small gain is desired to mitigate terrestrial multipath and interference signals generally strong near the horizon.

The ideal gain pattern and spatial coverage vary from application to application. Before 2010, conventional GPS generally called for 80° > θ_c > 70° for terrestrial applications and 100° > θ_c > 80° for airborne applications. After 2010, GNSS applications are expected to move toward a higher cutoff elevation angle, probably about 70° > θ_c > 50° for terrestrial applications and 80° > θ_c > 60° for airborne applications.

1.1.1.3 Multipath Mitigation and Interference Suppression

The multipath rejection performance of an antenna can be investigated with the help of a desired (D) to undesired (U) signal ratio. In general, the multipath due to the ground reflections can be mitigated by passing the D signals at positive elevation angles into a reasonable gain GNSS antenna and by attenuating the U signals at the corresponding negative elevation angles with the help of an antenna radiation pattern.

The antenna is primarily a spatial filter to elevate the SNR of line-of-sight signals from selected satellites, by suppressing multipath and interference signals. A GNSS antenna with higher cutoff angle θ_c above the horizon and a good axial ratio (or low cross polarization) would have higher antenna gain over noise temperature to detect low line-of-sight CDMA signal desired, as demonstrated in the QZSS tests. To suppress multipath and interference signals below the cutoff angle C, choke ring, resistive loading, conducting ground plane, or metamaterials are placed at the rim of high-performance GPS antennas. The anticipated change in θ_c would affect their design methodology and usage in GNSS antennas, as they are generally bulky, heavy, and expensive.

1.1.1.4 *Phase Center Stability (PCS)*

Stability of a GNSS antenna's phase center over frequency and spatial angles is a serious problem for high performance GNSS antennas, especially as they strive to cover more GNSS bands and wider bandwidth. This is an ultimate performance parameter as well as a limitation posed by the GNSS antenna [7], which will be addressed later.

The observed values in navigation and positioning system are based on the phase center, PC of receiver antenna; thus, the accuracy of positioning system was directly affected by the precision of PC [8]. In reflector antenna system, only by accurately measuring the PC position of feed can be ensured that the PC of the feed antenna is installed on the focus of the reflector [9]. In interferometer direction finding antenna system, the direction of an incoming wave is determined by measuring the phase difference among the phase center of each array element. In large phased array antenna system, such as the Synthetic Aperture Radar (SAR), PC is used as the benchmark for imaging [10]; thus, the image quality is directly related to the precision of PC.

The far-field equiphase surface of any practical antenna cannot be an ideal sphere because of the radiation mechanism of antennas. The PC can be considered as the curvature center of the antenna main beam equiphase surface. However, the curvature center in any angular range of the main beam could be different [10]. Thus, phase center stability (PCS) is introduced to represent the size of such an area that contains all or most of these different curvature centers in the main beam.

Circularly polarized patch antenna is frequently used in satellite navigation system [8]. Thus, design of circularly polarized patch antenna with high phase center stability is of great significance and application value [11].

1.1.2 GNSS Antenna Fundamentals

In this chapter, GNSS antenna performance requirements and antenna properties that affect functionality and performance of a GNSS antenna are presented. The antenna is a crucial front-end component of a GNSS receiver system. In general, the function of any receiver antenna is to capture the electromagnetic signals from free-space and convert them into electrical signals in order to be processed by the receiver. At the receiver, the RF signal strength of a signal received from the GNSS satellite is very weak and these GNSS signals can arrive from any direction.

The following are some of the important GNSS antenna properties that affect the performance and functionality of the GNSS antenna:

- Radiation characteristics at the center frequency in the GNSS frequency bands,
- Antenna polarization,
- Axial ratio,
- Bandwidth,
- Desired to undesired ratio (D/U ratio) (e.g., gain pattern shape),
- Antenna phase center, and
- Multipath mitigation.

1.1.2.1 Resonant Frequency

The resonant frequency or operating frequency is a frequency at which capacitive and inductive reactance of an antenna cancel out each other. Usually, a resonant frequency of interest can be achieved by tuning an antenna to a particular frequency. In reality, there can be a shift in the resonant frequency of a microstrip type due to the antenna packaging, ground plane size and input feeds.

Real and imaginary parts of the normalized impedance in a complex plane can be represented on a Smith Chart, where the real part varies from 0 to ∞, and the imaginary part of impedance varies from -∞ to ∞. The end points located on the left and right side on horizontal axis of a Smith Chart refers to the short circuit and open circuit respectively. Similarly, the top and bottom most points on the vertical axis represents the inductive and capacitive nature of the circuits, respectively. In order to obtain a good impedance match at the antennas the input impedance should be at the center of Smith Chart. The point at which the antennas impedance intersects the horizontal axis and close to the center of the Smith Chart, indicates the resonant frequency of an antenna.

1.1.2.2 Return Loss (RL) and Voltage Standing Wave Ratio (VSWR)

VSWR is a scalar measurement that characterizes the amount of signal reflected from the antenna with respect to the signal incident, at the antenna terminal due to the impedance mismatch. VSWR corresponding to a perfect mismatch is infinity, and a perfect match is 1. However, a perfect match is difficult to achieve in reality. The "loss" obtained due to the mismatch can also be described as a return loss (RL). VSWR is an important measure to characterize the GNSS antenna performance. Due to a very small delay of any reflections VSWR measure less than 2:1, (corresponds to a RL of -9.5 dB) is used for most GNSS applications. A lower VSWR may be suitable for certain high performance GNSS applications. Equations correspond to RL and VSWR are given in equations (1.1) and (1.2) [12].

$$Return\ Loss(RL)in\ dB = 10\ \log_{10}\left[\left(\frac{VSWR-1}{VSWR+1}\right)^2\right] \tag{1.1}$$

$$or$$

$$Return\ Loss(RL)in\ dB = -20\log_{10}|\Gamma| \tag{1.2}$$

$$SWR\ or\ VSWR = \frac{(1-|\Gamma|)}{(1+\ |\Gamma|)} \tag{1.3}$$

where,

Reflection coefficient, $\Gamma = \frac{Z_L - Z_O}{Z_L + Z_O}$;

Characteristic Impedance, Z_O ;

Load Impedance, Z_L is zero, infinity, and equal to Z_O; for the short, open, and matching circuits, respectively.

1.1.2.3 Antenna Bandwidth (BW)

BW of an antenna is defined as, "the range of frequencies within which the performance of the antenna, with respect to some characteristic, conforms to a specified standard" [13]. Based upon the application type, there are several measurements to define an antenna bandwidth [14], of which VSWR (e.g., < 2:1) and axial ratio (e.g., < 3 dB) are two important BW definitions for the GNSS antenna application. The GNSS antenna designed here should have a minimum bandwidth of 103 MHz at VSWR < 2:1 (or RL < -9.5 dB) around its center frequency (i.e., 1600 MHz).

The desired frequency band for GNSS antenna is from 1.16 GHz to 1.6 GHz to cover the GPS L1 - L5 bands, GLONASS G1, G2 and G3 as well as the Galileo E5a, E5b, E6, and E1bands.

1.1.2.4 Antenna Polarization

Polarization of an electromagnetic field is defined as a curve traced by the tip of an instantaneous electric field vector as the wave is propagating away from the observation point [14][15]. Elliptical polarization is a more common type of polarization with the linear and CP as its extreme cases. The polarization of a GNSS antenna describes how the antenna is sensitive to the polarization of the wave incident upon it. In general, GNSS use RHCP to minimize the effect of polarization fading and Faraday rotation. Moreover, CP minimizes the signal fluctuations due to the orientation mismatches between the transmitter and the receiver antennas. Therefore, to obtain the maximum RF signal reception from SV's, the designed GNSS antenna should be RHCP.

In wireless communication, electromagnetic (EM) waves are the means of transferring information between the transmitter and receiver. A general Transverse Electromagnetic (TEM) wave has electric field, E and magnetic field, H components perpendicular to each other and perpendicular to the direction of propagation. Further, it can be characterized at an observation point by frequency, magnitude, phase, and polarization [3].

In the case when the two filed components, E_x and E_y are equal, then the polarization will be linear at angle of 45°. Furthermore, when the magnitude of E_x is negligible, a vertical polarization is obtained. Similarly, a horizontal polarization achieved when $E_y \approx 0$. If $E_x \neq E_y$, then the polarization is given at an angle of:

$$\gamma = \tan^{-1}\frac{E_y}{E_x} \tag{1.4}$$

A schematic illustration for a linearly polarized wave is shown in Figure 1.3 [16].

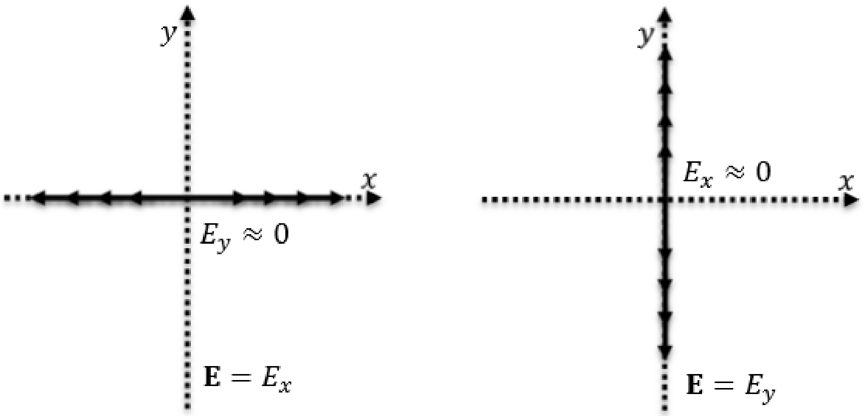

Figure 1.3: Horizontal and vertical linear polarization [16].

For a wave with a phase of $\delta = \pm 90$ and $E_x = E_y$, the field vector moves in a circular path as can be seen from Figure 1.4 and the polarization is said to be circular. However, if $E_x \neq E_y$, which is more common, then the field vector rotates in elliptical path and the polarization is said to be elliptical as illustrated in Figure 1.5 [16]. When the wave rotates in a clockwise direction, towards the observer, an

LHCP radiation is accomplished. On the other hand, if the wave rotates in an anti-clockwise direction, a RHCP radiation is obtained.

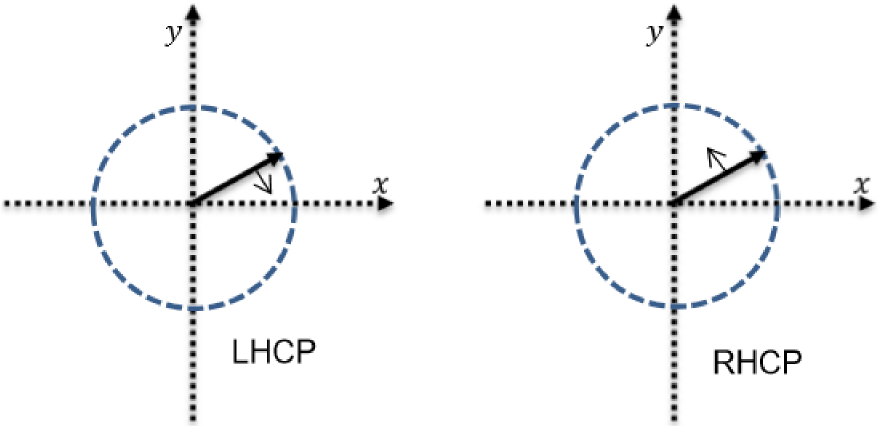

Figure 1.4: Left-handed and Right-handed circular polarization [16].

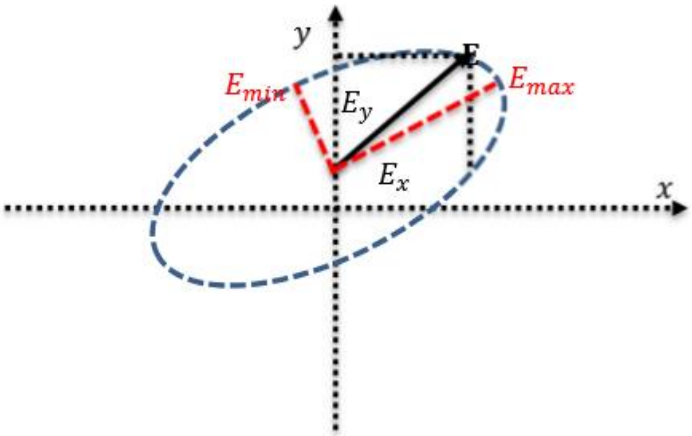

Figure1.5: Elliptical polarization [16].

Circular polarization is defined by the Axial Ratio (AR), which is the ratio of the maximum and minimum semi axes of the ellipse and is given in decibels by [17]:

$$AR = 20\log_{10}\frac{E_{max}}{E_{min}} \tag{1.5}$$

from which it can be noticed that $1 \leq AR \leq \infty$. A pure circular polarisation can be achieved when AR = 1 or 0 dB, which is difficult to achieve in practice. Therefore, a frequency range over which AR ≤ 3 dB is considered and defined as:

$$AR_{BW} = \frac{f_2 - f_1}{f_{min}} \tag{1.6}$$

where, f_2 and f_1 are the boundary frequencies for AR ≤ 3 dB and f_{min} is the frequency of minimum value of AR.

CP antennas offer a distinct advantage over their LP counterpart. That is, there is no need to establish a similar orientation between the transmitter and the receiver. As a result, the probability of linking a transmitted CP wave is higher since it can be received in the horizontal, vertical as well as any plane in-between. In contrast, LP wave is capable of radiating in one plane only, which is particularly inefficient for mobile and satellite applications. Moreover, a CP wave that is transmitting in all planes is less susceptible to unwanted reflection and absorption. Reflecting surfaces may scatter the wave with a different phase, which results in a weak LP signal.

However, a CP wave can be received regardless of the reflected plane. Additionally, CP antennas are capable of reducing the Faraday rotation effects, which means that a linearly polarized wave may be rotated by an unknown amount depending on the thickness and temperature of the ionosphere, as well as the frequency and therefore causes a reduction of 3 dB in the signal strength of linearly polarized antennas [18], [19]. On the other hand, CP antennas tend to lose their polarization and become elliptically polarized in the case of non-normal incident. In addition, CP waves lose their sense if reflected by a PEC, with 180° reflection phase, which may change a RHCP wave into a LHCP wave or vice versa. Therefore, CP antennas are not recommended for indoor radio communications [19].

1.1.2.5 Antenna Axial Ratio (AR)

AR of the polarization ellipse is the ratio of its major to minor axes length [14][15]. An AR close to one (0 dB) indicates good CP where, AR greater than one indicates RHCP and less than one indicates LHCP, and an AR close to infinity indicates good linear polarization. Calculations for AR are shown in equation (1.7) [20].

For GNSS applications, the AR is usually specified at the antenna boresight because the AR will increase along with the increase in boresight angle (which decreases with the increase in elevation angle). Low AR is desirable for most of the elevation angles. At the upper hemisphere elevation angles (above 10°), the boresight AR should be less than 3 to 6 dB for a high performance GNSS application. AR should be between 0 dB to 1 dB for the high-end GNSS application antennas like choke ring and geodetic quality antennas [21].

$$Axial\ Ratio, AR = \frac{E_{major}}{E_{minor}} = \left[\frac{E_{RHCP} + E_{LHCP}}{E_{RHCP} - E_{LHCP}}\right] \tag{1.7}$$

where,

E_{major} and E_{minor} are the length of the major and minor axes of the polarization ellipse,

E_{RHCP} and E_{LHCP} are the complex RHCP and LHCP antenna responses (in volts)

$$E_{RHCP} = \frac{1}{\sqrt{2}}\left(E_{\theta} + E_{\varphi}\right) \tag{1.8}$$

$$E_{LHCP} = \frac{1}{\sqrt{2}}\left(E_{\theta} - E_{\varphi}\right) \tag{1.9}$$

E_{θ} and E_{φ} are the linear field components along θ and φ directions (in volts) and θ and φ are spherical coordinates.

1.1.2.6 Antenna Pattern

The upper hemisphere GNSS antenna radiation pattern should have sufficient and uniform gain and efficiency to effectively receive the GNSS SV signals at the various azimuth and elevation angles in the upper hemisphere [22]. For most GNSS applications, the antenna should have a uniform radiation pattern over the upper hemisphere with a sharp roll off at the lower elevations to reduce the multipath and lower hemisphere interference [22]. GPS receivers typically use a mask angle of 10° at the lower elevation angles to minimize multipath and atmospheric effects [23].

1.1.2.7 Desired to Undesired Ratio

The multipath rejection performance of an antenna can be investigated with the help of a desired (D) to undesired (U) signal ratio; in general, the multipath due to the ground reflections can be mitigated by passing the D signals at positive elevation angles into a reasonable gain GNSS antenna and by attenuating the U signals at the corresponding negative elevation angles with the help of an antenna radiation pattern. In this research, D/U is calculated by taking the antenna RHCP gain (in dB) difference between the positive and negative elevation angles [24].

1.1.2.8 Antenna Phase Reference

The antenna phase response will vary as a function of the azimuth and elevation angle. The antenna phase response can be measured with respect to an Antenna Reference Point (ARP) where the measured antenna phase response can then be used to compensate for these antenna phase variations, with respect to the ARP, depending upon the performance requirement [25].

1.1.3 Design Challenges: Size Constraints, Feed Network, and Cost

Challenges facing the design of GNSS receive antennas stem from two major premises: the greatly enlarged. Bandwidth requirement and the constraints by the platform on which the antenna operates. Feed network and cost are other major challenges. These are discussed as follows.

1.1.3.1 *Size Constraint*

Antenna size constraint and simultaneous broad banding are conflicting requirements facing fundamental physical limitations, established in a rigorous analysis six decades ago [26], which relates the fundamental limitation of the gain bandwidth of an antenna to its electrical size. Also, for a GNSS antenna, its platform (in a broad sense including the platform's immediate environment) dictates how, and how well, the antenna can mitigate problems due to multipath signals from satellite platform, ionosphere, troposphere, and terrestrial environment, as well as natural and human-made interferences and noises.

1.1.3.2 *Feed Network*

The feed network bridges between a coaxial cable and the radiating aperture, providing excitation to generate RHCP. Since the GNSS antenna needs to detect extremely low GNSS signals, about 25 dB below noise level on Earth, the use of LNA close to the antenna is highly desirable. LNA elevates the signal strength so that it would not be attenuated away before reaching the receiver, usually via a cable 1 to 3 m long, which adds more noise as well.

Additionally, the LNA augments frequency filtering and further enhances SNR. Because of the high-performance benefit and low cost, use of LNA as part of GNSS antenna is ubiquitous today. For high performance, a user may select antenna and LNA separately. With the transition from the narrowband and mostly single band, GPS to the multiband broadband GNSS, feed network design will be fundamentally changed not only by performance considerations but also by production cost issues. This challenge will be even more serious in the more complex feed network of anti-interference GNSS arrays with the fixed or adaptive gain pattern.

1.1.3.3 Cost

The cost of a GNSS antenna is a fundamental design consideration driven by the market. A testimony is the patch antenna, whose widespread use is not only due to its low-profile, platform-compatible structure, and medium to small size, but also for its low cost enabled by its simple feed. However, the patch antenna’s performance and cost advantages will be challenged by other antennas in the new multiband/broadband GNSS scenario.

1.1.4 Basic GNSS Antenna Approaches

It is also desirable to know the basic antenna approaches for GNSS antennas. The answers can be found in several books [17], [19], [27]–[30] covering GNSS antennas, as well as in general antenna books, outside the GNSS context, under the category of antennas of CP with a broad symmetrical unidirectional beam and a peak directivity of 3 – 10 dBi (A higher directivity leads to a narrower beam, and thus a higher cutoff angle θ_c above the horizon).

Wang *et al*. in [6] summarized the basic antenna types applicable to GNSS and a broad overview of their characteristics in Table 1.3. Patch antennas are the most common and have a very wide range of variations, e.g., slot-loaded patch antennas, stacked patch antennas, E-patch antennas, etc. However, the patch antenna is a resonant antenna, thus inherently narrowband; many elaborate efforts have been made to add more bands and bandwidth.

The four-element ring arrays consist of four radiating elements fed with a four-way hybrid or beam-former of 0° - 90° - 180° - 270° to effect RHCP. Each radiating element can be a slot, a conducting patch of some shape such as a triangle, a Vivaldi element, an H-slot antenna, or an F or inverted-F antenna, etc. As a multiband GNSS antenna, it is necessary that the element radiators have some inherent broadband or multiband potential.

The spiral antenna and the quadrifilar helix antenna are also common GNSS antennas. Planar spiral antennas have several variations, mostly for changing their bidirectional radiation to unidirectional. The traveling-wave (TW) antenna is one technique that overcomes this problem by employing the spiral or other broadband planar radiators and having a closely spaced conducting ground plane [31], [32].

Table 1.3: Basic Antenna Types Used in GNSS and Their General Characteristics [6]

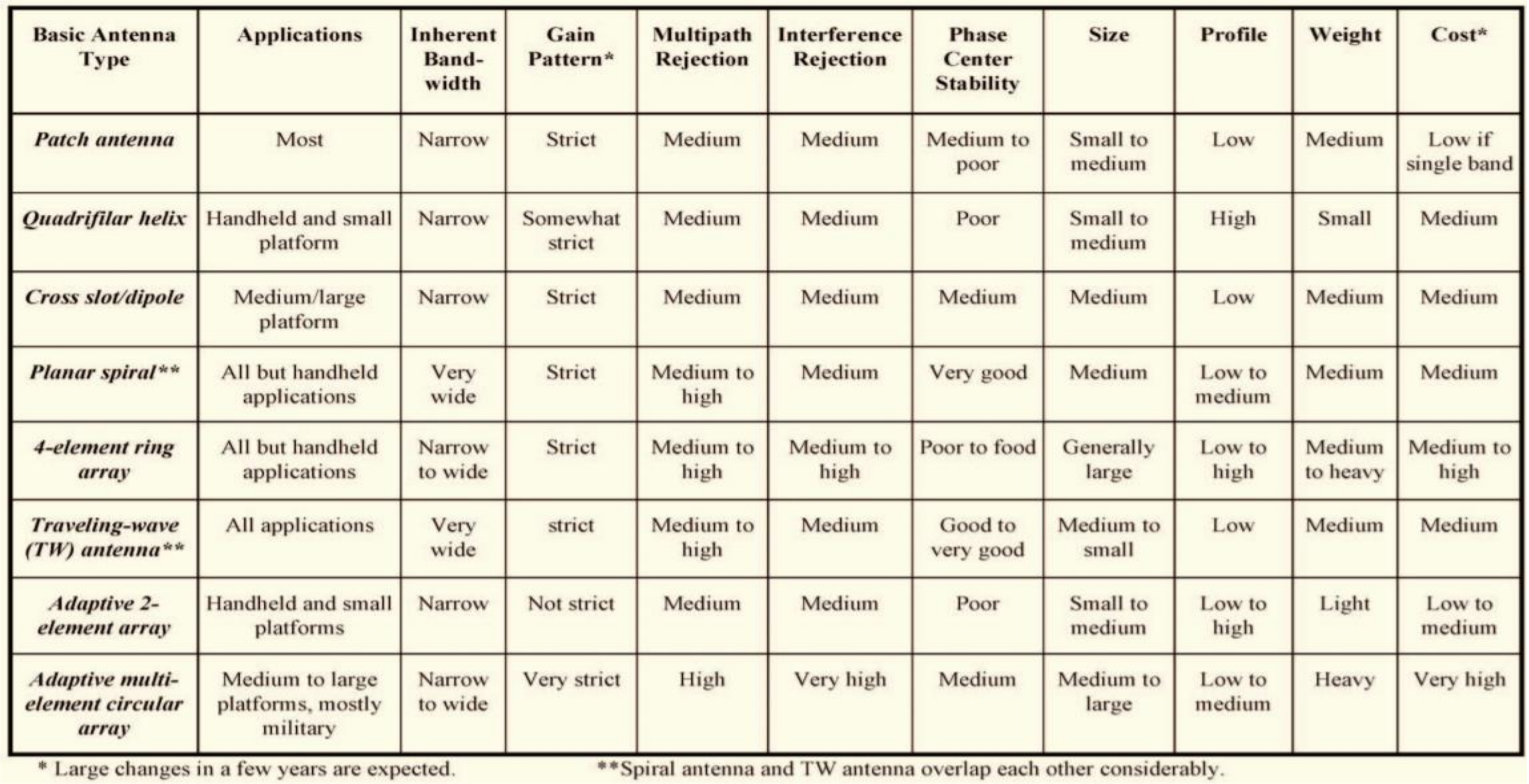

Basic Antenna Type	Applications	Inherent Band-width	Gain Pattern*	Multipath Rejection	Interference Rejection	Phase Center Stability	Size	Profile	Weight	Cost*
Patch antenna	Most	Narrow	Strict	Medium	Medium	Medium to poor	Small to medium	Low	Medium	Low if single band
Quadrifilar helix	Handheld and small platform	Narrow	Somewhat strict	Medium	Medium	Poor	Small to medium	High	Small	Medium
Cross slot/dipole	Medium/large platform	Narrow	Strict	Medium	Medium	Medium	Medium	Low	Medium	Medium
Planar spiral**	All but handheld applications	Very wide	Strict	Medium to high	Medium	Very good	Medium	Low to medium	Medium	Medium
4-element ring array	All but handheld applications	Narrow to wide	Strict	Medium to high	Medium to high	Poor to food	Generally large	Low to high	Medium to heavy	Medium to high
Traveling-wave (TW) antenna**	All applications	Very wide	strict	Medium to high	Medium	Good to very good	Medium to small	Low	Medium	Medium
Adaptive 2-element array	Handheld and small platforms	Narrow	Not strict	Medium	Medium	Poor	Small to medium	Low to high	Light	Low to medium
Adaptive multi-element circular array	Medium to large platforms, mostly military	Narrow to wide	Very strict	High	Very high	Medium	Medium to large	Low to medium	Heavy	Very high

* Large changes in a few years are expected. **Spiral antenna and TW antenna overlap each other considerably.

1.2 RESEARCH MOTIVATION AND OBJECTIVES

Modern GNSS technology is facing more challenges and new fields for researchers to explore. One hot topic is the multi-system GNSS device. Many research groups have demonstrated that a multi-system GNSS receiver (e.g., GPS and Galileo) will usually provide more observations than a single-system receiver which provides higher positioning precision. Accordingly, such a multi-antenna system requires compact design which brings a new challenge for the antenna engineers.

Meanwhile, compact design always makes the commercial GNSS antenna more competitive compared with larger size antenna with similar performance. Smaller is always better. The motivation for the antenna designers is to miniaturise the size of the antenna and meanwhile keep its standard performance.

The objective of this research is to design, simulate and investigate the performance of a circularly polarized antenna prototype, which is expected to operate at GNSS frequency bands from 1.16 GHz to 1.6 GHz to cover the GPS L1-L5 bands, GLONASS G1, G2 and G3 as well as the Galileo E5a, E5b, E6, and E1bands with good multipath mitigation. A printed dipole design is chosen for this prototype because of the following merits: ease of fabrication and mounting, multipath performance, relatively low profile, easy integration with active components.

1.3 CONTRIBUTIONS AND ORGANIZATION OF THIS THESIS

This thesis consists of seven chapters that mainly focus on design, optimization, and measurement of novel broadband antennas for GNSS applications. The structure of the thesis and the outcome and achievements of each chapter is discussed briefly in this section to give a better view of the work. The chapters are organized as follows:

- Chapter 1 introduces the background of this work, including the motivation and objectives of the research in this thesis.
- Chapter 2 is an overview and fundamentals of GNSS system and a brief introduction about interference, jamming attack and jamming effect on GNSS. The history of the system and communication are discussed.
- Chapter 3 gives an overview of the development on GNSS receiver antenna design using the different type of antennas and its design parameters with a detailed literature review of the state-of-art for these applications. Then, it discusses the antenna diversity systems, and the existing crossed-dipole antenna designs for GNSS applications in detail.
- Chapter 4 introduces a new broadband with broad beamwidth antenna to cover the GPS L1-L5 bands, GLONASS G1, G2 and G3 as well as the Galileo E5a, E5b, E6 and E1bands (1.08 GHz – 1.69 GHz). This broadband antenna demonstrates a significant improvement on bandwidth and radiation pattern by using the parasitic elements and loaded monopoles that are excited by coupling with the elliptical crossed dipole in the center of the antenna.
- Chapter 5 presents a new way of designing a dual-band CP antenna by integrating a CP radiator with a finite AMC surface. The antenna demonstrates

a low-profile broadband characteristic and excellent CP radiation for GNSS frequency bands.

- Chapter 6 introduces a new optimized antenna that more compact from the previous antenna discussed in Chapter 4 and 5. This chapter also presents a new antenna array configuration combining a 4-elements antenna array and a 5-elements antenna array to provide wide coverage. The anti-jamming performance of the antenna with respect to differently polarized jammers as well as its positioning capability are also presented.
- Finally, Chapter 7 provides a summary of the major contributions of this thesis. In addition, some future work recommendations for this research topic are suggested.

CHAPTER 2:

GNSS SYSTEM OVERVIEW

2.1 INTRODUCTION

The role of the Global Positioning Satellite System (GNSS) has become indispensable in our lives. Because of its significance, research is very active in this sector and obtaining higher reliability, and higher accuracy is essential to sustain the integrity of the position, velocity, and time (PVT) solutions. Initially, a military satellite system that was later provided partially to the public, GNSS system has seen explosive growth in the number of users. There are also many industry sectors that rely on it such as precise timing, precise positioning used in geodesy and structural engineering, aviation, land and maritime navigation, etc. [3].

This chapter starts with a general introduction of the GNSS system's sectors followed by the GNSS observables, the generic structure of the receiver and finally a summary of the GNSS errors which will pave the way towards the main objectives of this research. Interference and jamming are then overviewed; where their types, causes, sources, effects, and mitigation techniques are described.

2.1.1 GPS Fundamentals

Operated by the United States, GPS is the best-known satellite-based radio navigation and positioning system among the GNSS, which provides accurate and instantaneous Position, Velocity and Timing (PVT) services for an unlimited number of civilian and military users in all weather conditions. A GPS receiver needs at least four visible satellites to calculate the three-dimensional position and time solution. Any GNSS including GPS system is mainly made up of three major segments (see Figure 2.1):

- Space Segment (SS) or Satellite
- Segment Control Segment (CS) or Operational Control Segment (OC)
- User Segment (US)

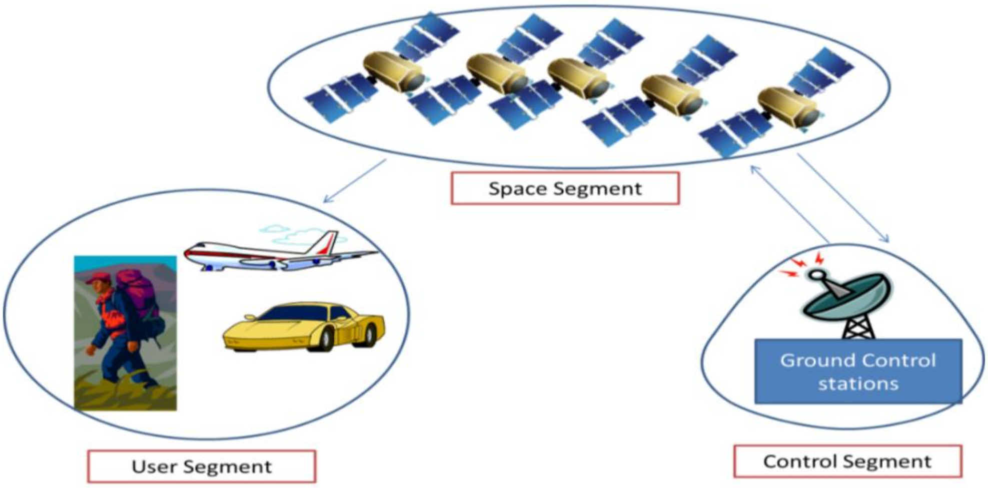

Figure 2.1: GPS segments.

2.1.1.1 *Space Segment (SS)*

GPS constellation as shown in Figure 2.2 consists of 24 operational satellites in six orbital planes with four satellites in each plane. It has been recently upgraded to 27 by the US air force [33]. The number of satellites can increase up to 30. The ascending nodes of the orbital planes are separated by 60 degrees, and the orbital planes are inclined 55°. The orbit of each GPS satellite is nearly circular with a semi-major axis of 26578 km and a period of about twelve hours. The satellites continuously orient themselves to ensure that their solar panels stay pointed towards the Sun, and their antennas point toward the Earth. Each satellite carries four atomic clocks, is the size of a car and weighs about 1000 kg [34].

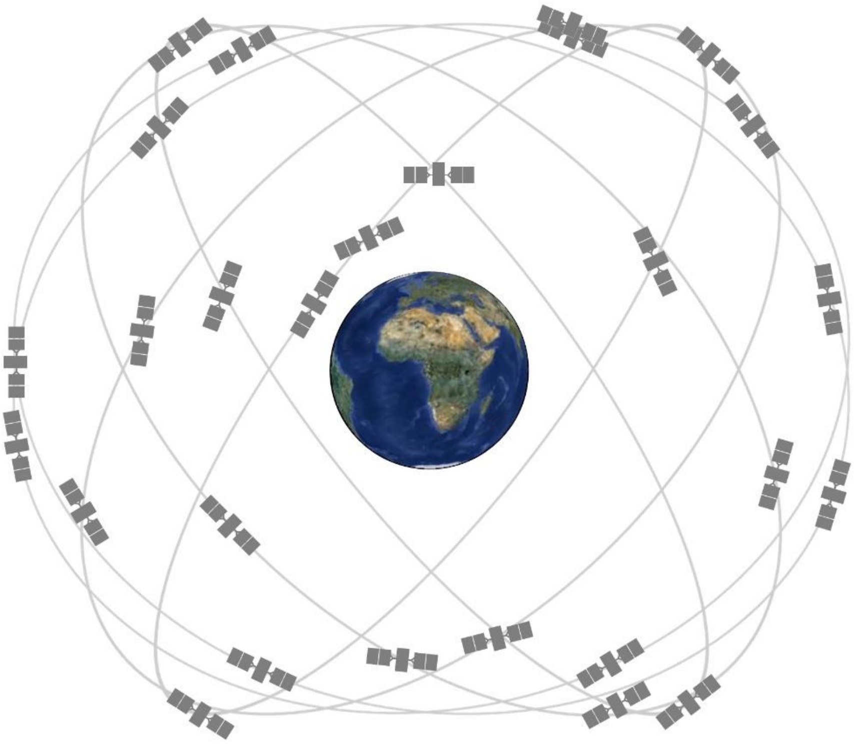

Figure 2.2: Expandable 24-slot satellite constellation[33].

2.1.1.2 Control Segment (CS)

The control segment of GPS is made up of a network of tracking stations positioned across the Earth as shown in Figure 2.3 with a master control station (MCS) located at Colorado Springs, Colorado, USA. This MCS is staffed around the clock. There are 16 monitoring stations located throughout the globe. Six of them are operated from Air Force bases and ten from the National Geospatial-Intelligence Agency (NGA) [33]. They are located around the Earth, and their positions are known very precisely. These stations are equipped with very sophisticated GPS receivers and a cesium oscillator for tracking all the satellites in view. The MCS remotely operates these ground control stations.

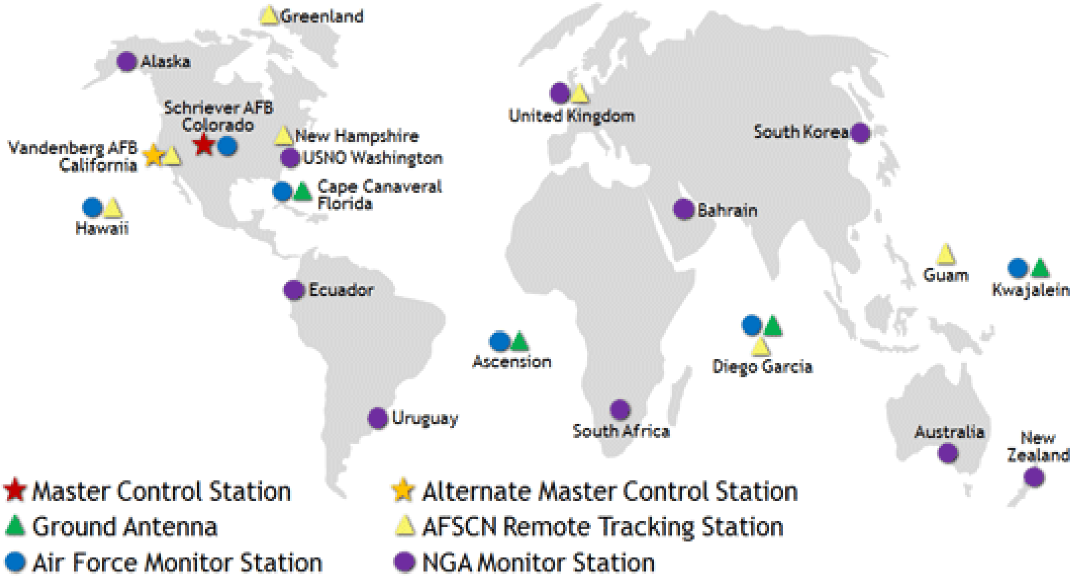

Figure 2.3: Locations of the different sections of the control segment around the world [33].

Among the tasks of the control segment are: (a) monitoring and maintaining satellite orbits and health by maneuvering and relocation, (b) maintaining GPS time,

(c) predicting satellite ephemerides and clock parameters and (d) updating satellite navigation messages periodically [3].

2.1.1.3 User Segment (US)

The user segment consists of users (individuals, commercial or military) with different radio receivers that receive signals from GPS satellites and estimate their position, velocity, and time. Users of GPS can be classified into civil and military. The user segment is experiencing exponential growth since inauguration due to decreasing prices of the receiver and the increasing application of GPS in daily life. When a GPS receiver is activated, it will acquire the GPS satellite signals [35]. The signal is processed, and the receiver position is determined by the intersection of the spheres created by the satellite pseudoranges. A minimum of four satellites with good geometry is required. Three satellites are required for the position fix, while the fourth is required to account for the receiver clock offset. An in depth look at the user segment can be found in [36] and [1].

2.1.2 GLONASS Fundamentals

GLONASS is a Russian version of a GNSS that provides the three-dimensional PVT services across the globe in all weather conditions, similar to GPS made up of a, satellite Space Segment, monitoring Control Segment, and User Segment. The Space Segment has eight, equally spaced satellites (a total of 24) in three orbital planes. Each satellite takes 11 hours, 15 minutes and 44 sec to complete an orbit with 64.8° inclination to each other [37]. The GLONASS transmission frequency is determined by its channel number, K and its frequency bands are calculated using the following expression.

$$f_{L1}\,(K) = f_{L1} + K\Delta f_{L1} \tag{2.1}$$

$$f_{L2}\,(K) = f_{L2} + K\Delta f_{L2} \tag{2.2}$$

where,

$f_{L1} = 1602\,MHz\ and\ \Delta f_{L1} = 562.5\ kHz\ for\ L1\ sub\ band\ and$

$f_{L2} = 1246\,MHz\ and\ \Delta f_{L2} = 437.5 kHz\ for\ L2\ sub\ band$

The Control Segment consists of a satellite tracking and command stations network located across Russia to monitor the satellites and provide the corrections to the orbital parameters and navigation data as needed [37]. The User Segment is equipped with receiver equipment to receive and process the GLONASS signals transmitted by the satellites to determine the user PVT solution. GLONASS historically has used FDMA in similar frequency bands as GPS (i.e., L1, L2, L5), and is now developing a CDMA-based GLONASS GNSS.

2.1.3 Galileo Fundamentals

Galileo is the European GNSS, which is planned to provide highly accurate global positioning services to various users. Once deployed completely, the Galileo Space segment will consist of 27 operational satellites and three spare operational satellites (total 30) in three circular MEO orbit planes inclined at 56° and 29,601.297 km semi major axis. The Control Segment and User Segment are similar to GPS and GLONASS as discussed earlier.

2.1.4 Signal Characteristics

These satellite systems are fundamentally similar, and one can typically develop technology that generally applies to all of them. The research presented in this work, which focuses on the receiver antenna and its associated signal processing that applicable to any GNSS system so long as the antenna and antenna electronics are designed for the required frequencies. In this work, we will frequently use the term “GNSS antenna” to refer to an antenna designed for any one or multiple satellite navigation systems. Each GNSS satellite uses an array of transmit antennas to broadcast RHCP Electromagnetic (EM) energy with a radiation pattern that aims to evenly cover the entire visible portion of the earth. As mentioned above, this signal is quite weak, and it is modulated with unencrypted Pseudo Random Noise (PRN) code and navigation data. In this section, these three properties of the GNSS signal: its RHCP nature, its low signal strength, and its use of PRN codes will be discussed.

2.1.4.1 RHCP Electromagnetic (EM) Energy

EM energy propagates through free space, such as the space between the GPS satellites and our antenna, at the speed of light. EM energy also propagates along conductive structures, such as ground-planes and the coaxial cables that deliver the energy from the antenna to the receiver, at near the speed of light. The waves that travel from the satellites to our antenna take the form of transverse electromagnetic plane waves.

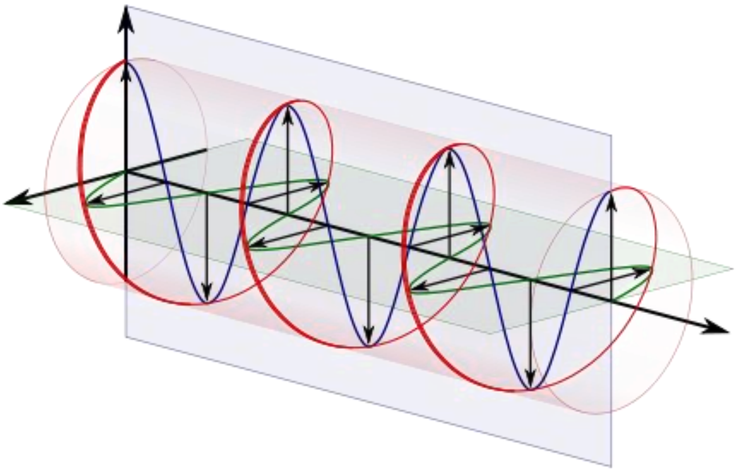

Figure 2.4: An RHCP wave where the red spiral traces the RHCP energy, and the blue and green sinusoidal waves trace the contributions from the x-axis and y-axis field components [38].

In the case of GNSS, these electromagnetic plane waves are RHCP. An RHCP wave can be decomposed into two orthogonal electric field components, which called as an x-axis field and a y-axis field for some arbitrary coordinate system in the plane parallel to the plane wave. These two field components are orthogonal not only in space but also in time, with the x-axis field lagging the y-axis field by 90°, as can be seen in Figure 2.4. The red spiral traces the RHCP energy while the blue and green sinusoidal waves trace the contributions from the x-axis and y-axis field components.

2.2 INTERFERENCE AND JAMMING

As mentioned earlier, interference and jamming signals prevent RF front-end from functioning correctly. It has been reported in [2] that no matter what tracking and acquisition have been implemented in the digital part of the receiver, they will be rendered useless. The latter condition is true if the GPS signals were totally corrupted by the nonlinear behavior of the front-end. Spectral characteristics such as the carrier frequency and bandwidth, f_{int} and B_{int} respectively, can lead to a broad classification of interferences. A higher-level classification would include in-band and out of band signals.

Table 2.1: Classification of Interferences Based on Spectral Characteristics

Class	**Spectral Characteristics**
Out-of-band interference	$f_{int} > f_{IF} + \frac{B_{IF}}{2}$ or $f_{int} < f_{IF} - \frac{B_{IF}}{2}$
In-band interference	$(f_{IF} - \frac{B_{IF}}{2} < f_{int} < f_{IF} + \frac{B_{IF}}{2})$
Wideband interference	$B_{int} \approx B_{IF}$
Narrowband interference	$B_{int} \ll B_{IF}$

The former would encompass any signal whose carrier frequency is close but outside the GPS band while the latter would encompass signals found inside the GPS band. A more specific classification for the in-band interferences would differentiate between the bandwidths of different interference sources and categorize them into narrowband and wideband interferences.

The different classifications are demonstrated in Table 2.1 where B_{IF} and f_{IF} correspond to the GPS signal's bandwidth and center frequency after the IF stage [39]. Most interference signals are generated by licensed emitters that do not transmit in the L1 band; nonetheless, harmonics of these signals find their way into the GPS L1 band.

A summary of the different types of interference signals based on their modulation types as well as their potential sources is shown in Table 2.2. Some of the most common interference and jamming sources are demonstrated in Figure 2.5.

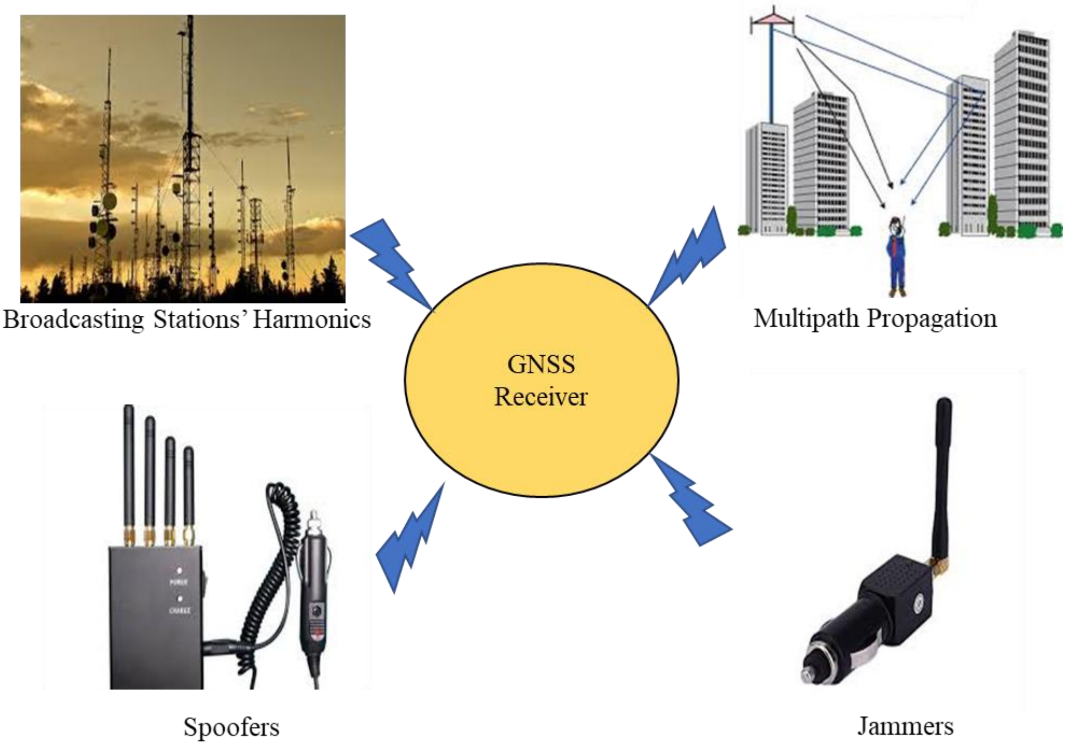

Figure 2.5: Common interference and jamming source.

Table 2.2: Types of RF Interference and Their Probable Sources

Class	**Type**	**Potential Sources**
Narrowband	Continuous Wave (CW)	Intentional CW jammers or near-band unmodulated transmitter's carriers
Narrowband	Swept CW	Intentional swept CW jammers or frequency modulation (FM) stations transmitters' harmonics
Narrowband	Phase/ frequency modulation	Intentional chirp jammers or harmonics from an amplitude modulation (AM) radio station, citizens band (CB) radio, or amateur radio transmitter
Wideband	Pulse	Any type of burst transmitters such as radar or ultra-wideband (UWB)
Wideband	Wideband - matched spectrum	Intentional matched-spectrum jammers, spoofers, or nearby pseudolites
Wideband	Wideband - phase/frequency modulation	Television transmitters' harmonics or near band microwave link transmitters overcoming the front-end filter of a GPS receiver
Wideband	Wideband - bandlimited Gaussian	Intentional matched bandwidth noise jammers

2.2.1 Jamming Attack on GNSS

GNSS anti-jamming was always considered a priority of the military sector, unfortunately, due to primarily, the growing demand of personal privacy devices (PPDs), [40]–[43] jamming is being viewed as a threat to the public; especially with the increasing dependence on the GNSS system. Jamming attacks have a sole objective of preventing the receiver from providing the desired solution. Although jamming is illegal and therefore criminalized, it has been reported that offenders have been using jammers to prevent stolen vehicles from being tracked or simply to remain undetected. Equally, PPDs are becoming cheaper and easier to acquire leading to the increased threat of GNSS outages for the everyday consumer [44][45]. Therefore, the struggle against jamming has been moved from the battlefield to the streets. Different types of GNSS Jammer are shown in Figure 2.6 [40].

Figure 2.6: Privacy GNSS jammer [40].

A GNSS jamming signal is typically transmitted on or around the GPS L1 frequency, which is 1575.42 MHz. It is not necessarily required to be very complex or powerful due to the fact that the GPS signals are extremely weak.

The jamming signal can effortlessly overwhelm the GPS receiver’s front-end and prevent the actual signal from being processed. Unfortunately, this occurs because the spreading gain (approximately 30 dB) is not yet applied to the signal. At that time, even after the spreading gain is applied, the jamming signal is also amplified therefore preventing further processing of GPS signals. The gain of the amplifier adjusts itself to the jamming signal, which is more powerful.

2.2.2 Jamming Effect on GNSS

Several studies [40], [41] have explored the effects of jamming and especially PPDs on Global Navigation Satellite Systems (GNSS) performance. Jamming deteriorates the positioning solution accuracy, leads to the total loss of lock on the satellite signals and therefore impairs the positioning availability. It has been reported that the typical front end is saturated in case of broadband additive white Gaussian noise (AWGN) signals, high power narrowband and pulsed signals. Contrarily, the front-end was not saturated when low power narrowband, spoofing and meaconing signals were applied. Several authors have studied the effects of jamming on acquisition and tracking [46]–[49]. Acquisition success is documented in [49]; where it has been identified that CW has the most damaging effect compared to swept CW and broadband noise which come in second place such that 10 and 15 dB Jamming to Signal Ratios (JSR) is required to prevent acquisition respectively.

2.3 ANTI-JAMMING TECHNIQUE

Successive detection is followed by mitigation if the receivers are equipped for it. A multitude of techniques has been proposed for anti-jamming and interference suppression. They can be classified mainly into single antenna-based techniques, which perform jamming mitigation based on receiver processing, whether in pre-correlation or post-correlation, and antenna array-based techniques, which benefit from the presence of the array to spatially mitigate the jamming signals by electronically controlling the radiation pattern of the array. Since all the mitigation techniques used by single antenna systems are present in the receiver, then it is appropriate to imply that they are all applicable in multi-antenna systems.

2.3.1 Single Antenna Receiver-based Solutions

Mitigation solutions in the front-end of the receiver are usually accomplished either using spectral or temporal excision. Mitigation of certain types of interference such as pulsed interference can be accomplished using a technique called pulse blanking. It is an appropriate technique aimed at mitigating pulsed interference. Interference excision is implemented in the time domain on the samples obtained from the ADC that are above a certain threshold. Alternatively, frequency excision is implemented in the front-end; it is based on determining the frequencies occupied by the interference signal.

Typically, a jammer is used to jam the signals of specific GNSSs and not all systems at the same time. Nevertheless, such jammers can be acquired at an expensive cost. A solution for this problem is to switch to another GNSS when service denial is sensed, such as GPS, GLONASS, GALILEO and BEIDOU (which has limited coverage). Switching from one GNSS to another requires more advanced hardware such as multiple frequency antennas and multi-constellation capable receivers.

2.3.2 Antenna Array Based Solutions

An antenna array is a group of antennas for which the outputs are combined to create an overall radiation pattern that is different from that of each antenna element individually [50]. These antennas are arranged in space depending on the array geometry. They are processed such that the radiation pattern of the array increases the gain towards a selected direction while rejecting signals emitted from other directions [51].

Thus, the interference signal(s) are rejected in space, rather than in the frequency or time domain. Interference mitigation is significantly enhanced by using an adaptive antenna array (also known as a smart antenna) through the capabilities of spatial filtering techniques. These techniques frequently attain high anti-jamming (AJ) margins. They are effective against both narrow and especially broadband interference signals that single antenna systems cannot combat [52].

Hence, adaptive arrays improve SNR in the presence of jamming which enables signal tracking in environments that would otherwise lack code and carrier phase observables. The most common techniques applied in adaptive spatial filtering are null steering and beamforming.

2.3.2.1 Null Steering

Null steering, also known as side lobe canceller (SLC), is based on the fact that the GPS signal power is lower than the noise floor. Null Steering considers any signal with a power level higher than that of the satellite to be an interference signal. Accordingly, the antenna's beam is steered away from that source and a null is directed towards it. The objective is to decrease the output power subject to the constraint that one antenna element is always on while trying to maintain unit gain in all other directions. The rest of the channels have their output phase and amplitude adjusted in order to block jammers.

2.3.2.2 Beamforming

Beamforming, on the other hand, enhances signal reception by directing beams towards desired signals. The desired antenna outputs are weighted using different sets of complex beamforming coefficients. In the case of GNSS, multiple beams are required; one for every satellite. Maximizing the power of the beam achieved by beamforming will also utilize the available degrees of freedom to shape the spatial null and minimize GNSS signal cancellation.

Therefore, the probability that GPS signals will be preserved increases. It is a known disadvantage of null steering that there will be a probable reduction in the received GNSS signal's energy level and especially if the signal's Direction of Arrival (DoA) is close to the interferer's DoA [53].

2.4 SUMMARY

In this chapter, GNSS antenna technologies and overview have been reviewed. It has been clearly shown that the research of GNSS antenna is of great significance to the modern industry and it will still be an important research topic for the coming decades. The studies of antenna for GNSS applications have been highlighted and discussed in detail. The information presented in this chapter is useful to gain a better understanding on the state of art in antenna designs and meanwhile identify the research challenges and problems for us to overcome in this work.

CHAPTER 3:

GNSS RECEIVER ANTENNA DESIGN: OVERVIEW AND STATE OF THE ART

3.1 INTRODUCTION

Global navigation satellite systems (GNSSs), including global positioning system (GPS), GLObal NAvigation Satellite System (GLONASS), Galileo, and Compass, will be fully deployed and operational in a few years [6]. An antenna for a GNSS receiver requires broadband characteristics for such as impedance matching and 3-dB axial ratio (AR) bandwidths, right-hand circularly polarized (RHCP) radiation, a wide CP radiation beamwidth (> 100°) facing the sky, and a high front-to-back ratio.

The use of a variety of single and dual-band CP antennas in the GNSS frequency bands has been reported: e.g., crossed dipole [54]–[58], monopole [59]–[62], slotted [63]–[68], patch [69]–[74] and dielectric resonator [75]–[79] antennas. However, most of these antennas have insufficient 3-dB AR beamwidth to meet the requirements of GNSS applications, owing to the lack of techniques to broaden the CP radiation beamwidth.

3.2 GNSS ANTENNA: OVERVIEW

A CP antenna for multi-frequency operation can be achieved by using multi-layer patches. By using a multi-layer structure, it is easier to achieve a multi-frequency CP operation. The dimensions of each patch mainly determine the resonant frequencies. The geometry of the proposed antenna is shown in Figure 3.1.

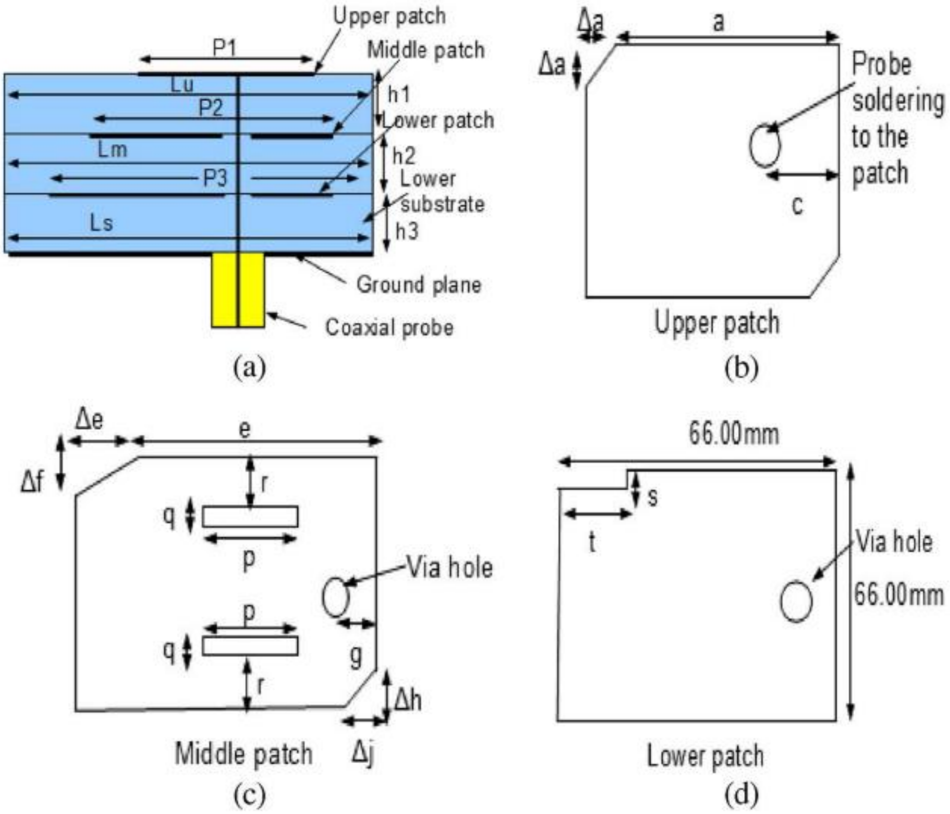

Figure 3.1: Geometry of the stacked patch CP antenna (a) side view (b) upper patch (c) middle patch and (d) lower patch [70].

A single probe feed of 50Ω input impedance is connected to the upper patch through via holes in the middle and lower patches while the middle and lower patches are excited through electromagnetic coupling. The via has contributed a capacitive coupling to negate the inductance effect due to the inner conductor of the probe. The use of slit on the edge of the lower patch introduces the dual orthogonal mode necessary for CP radiation pattern. Both the middle and upper patches are perturbed by corner truncation which produces near degenerated resonant mode resulting in CP.

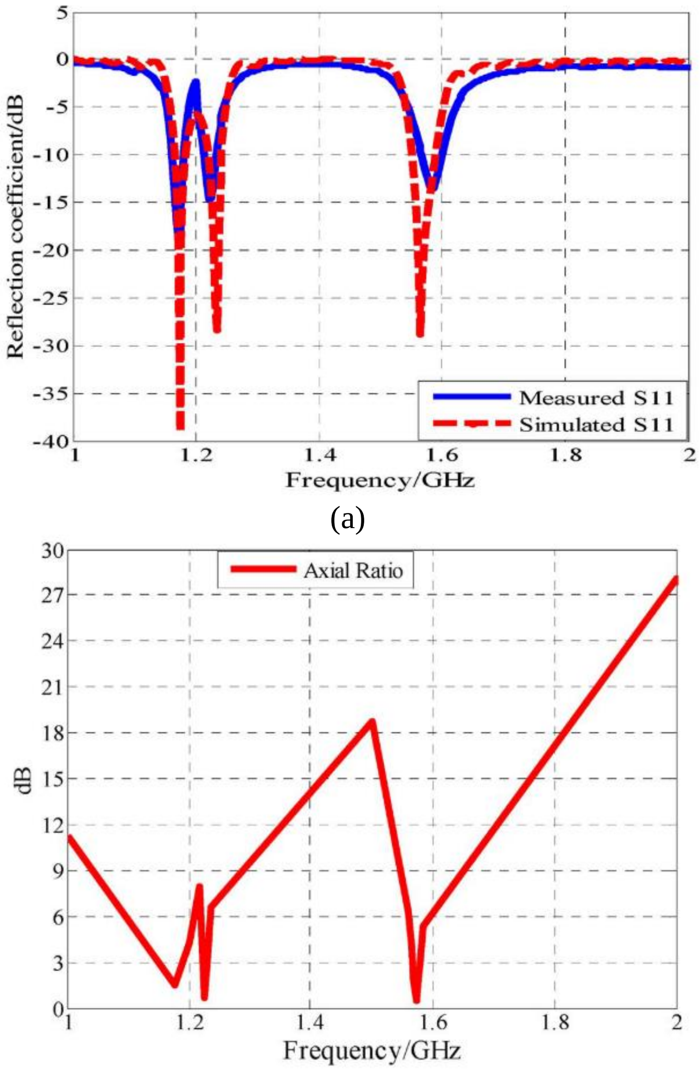

(a)

(b)

Figure 3.2: (a) Measured and simulated reflection coefficients of the antenna and (b) Simulated axial ratio of the proposed antenna [70].

Falade et al. [70] have proposed a design on stacked patches with a single feed for GPS frequency bands. The lower, middle, and upper patches are designed to resonate at L5, L2, and L1 frequency bands respectively. The patches are etched on three different substrates. The lower substrate has a thickness of h_3 = 1.524 mm and relative permittivity ε_r = 3.38, the middle and upper substrates are similar with a thickness of h_2 = h_1 =1.6 and permittivity of ε_r = 4.4.

The measured value of 10 dB impedance bandwidth for GPS L1, L2, and L5 frequency bands are 22 MHz (2.0%), 18 MHz (1.5%), and 30 MHz (2.0%), respectively are shown in Figure 3.2. The simulated axial ratio at broadside direction illustrates that the minimum axial ratio coincides with the resonant frequencies in the three bands. The 3-dB axial ratio bandwidth is 40 MHz (3.40%) in L5 frequency band, 10 MHz (0.81%) in L2 frequency band, and 13 MHz (0.83%) in L1 frequency band.

CP can also be generated by using a dielectric resonator antenna [75]–[77], [80]–[82]. A hybrid antenna comprising a dielectric resonator antenna (DRA) and four feed slots as shown in Figure 3.3 has been investigated and analyzed to enhance the AR bandwidth in order to cover the current GNSS frequency bands in one antenna [77]. The cylindrical DRA has a radius of 31.75 mm, a height of 22 mm and a permittivity of 10. It has been designed to resonate around 1.575 GHz. CP is generated by a 90° phase feed network. The slots have to be arranged and their dimensions optimized to ensure proper coupling to the dielectric resonator and to have good impedance matching. A substrate made of FR4 was chosen to accommodate the feed circuit of the DRA, and the slots were etched in the ground plane. The ground plane dimensions are 160 × 160 mm^2, and the slot length is 36 mm, and its width is 8.8 mm. The coordinates of the slots are 4 mm along the x-direction and 19.4 mm in the y-direction. The feed line is 12.9 mm long and 11 mm away from the slot center. The prototype of the DRA and its performance are shown in Figures 3.3 and 3.4. However, the disadvantage of the hybrid DRA over other GNSS antennas is its bulky in size.

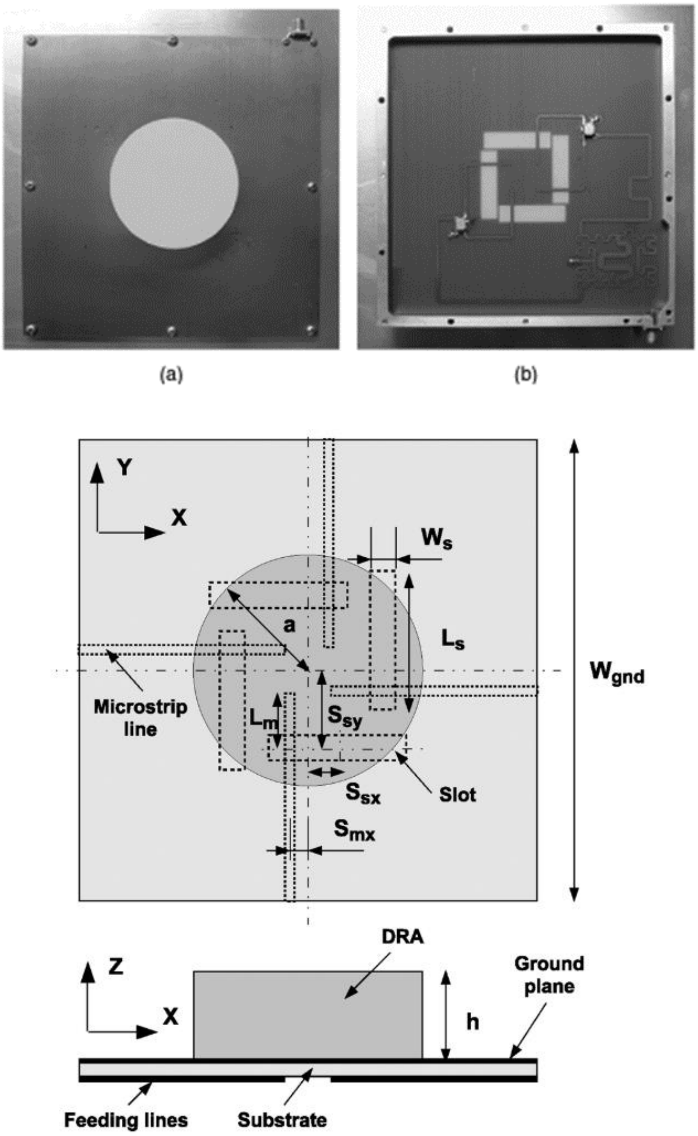

Figure 3.3: The diagram of the hybrid DRA[77].

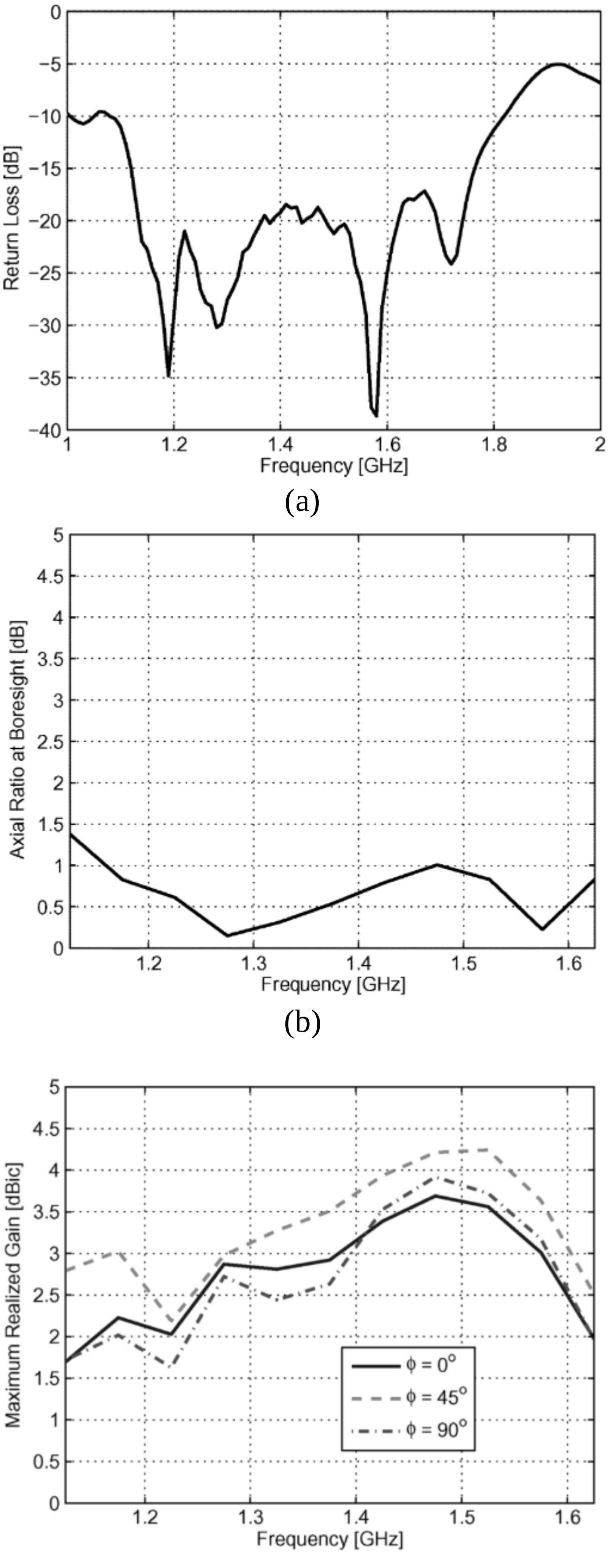

(a)

(b)

(c)

Figure 3.4: Hybrid DRA performance measured (a) S_{11} (b) maximum radiation gain and (c) axial ratio [77].

Two novel broadband single-feed printed compact wideband circularly polarized antennas as described in [59], consisting of L-shaped monopole and tilted cross on the ground plane with and without a slanted branch. By introducing a protruding cross at the ground, wideband CP is generated. The antenna has a very compact structure with a dimension of 88 × 88 mm^2 on the substrate. The antenna uses FR-4 substrate 1.6 mm thick with a permittivity of 4.4.

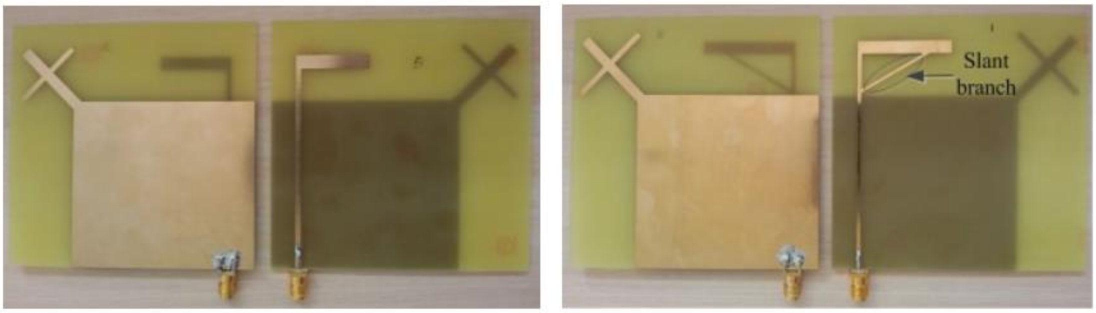

(a) (b)

Figure 3.5: Fabricated prototype of (a) antenna 1 (b) antenna 2 [59].

The geometry of the proposed broadband planar antenna with broadband CP is shown in Figure 3.5. All the metallic components of the antenna are printed on the same side of the substrate. The antenna consists of a square ground with a cross-shaped branch at its corner. The simulated and measured reflection coefficient and boresight AR of two antennas are compared in Figure 3.6 (a) and (b).

In Figure 3.6 (a), antenna 1 exhibits simulated (excluding the cable model) and measured -10 dB impedance bandwidths of 54.71%, from 1.130 to 1.981 GHz, and 55.10%, from 1.160 to 2.042 GHz, respectively. Besides, antenna 2 exhibits simulated (excluding the cable model) and measured -10 dB impedance bandwidths of 68.70%, from 1.096 to 2.243 GHz, and 70.44%, from 1.122 to 2.344 GHz, respectively. The results reveal that the slant branch is useful to improve the impedance matching. Figure 3.6 (b) shows that antenna 1 has measured 3-dB AR bandwidths at dual bands 1.356 -1.637 GHz (18.78%) and 1.794 - 2.487 GHz (32.38%). Also, antenna 2 has measured 3dB AR bandwidths at dual bands 1.270 - 1.600 GHz (23.00%) and 1.750 - 2.450 GHz (33.33%). The measured results agree well with the simulated results with the inclusion of the cable model. If the feed cable was excluded, 1.130 - 1.981 GHz (54.71%) and 1.096 - 2.243 GHz (68.70%) CP bands for two antennas are predicted in simulation, which is broad enough to cover GNSS spectra.

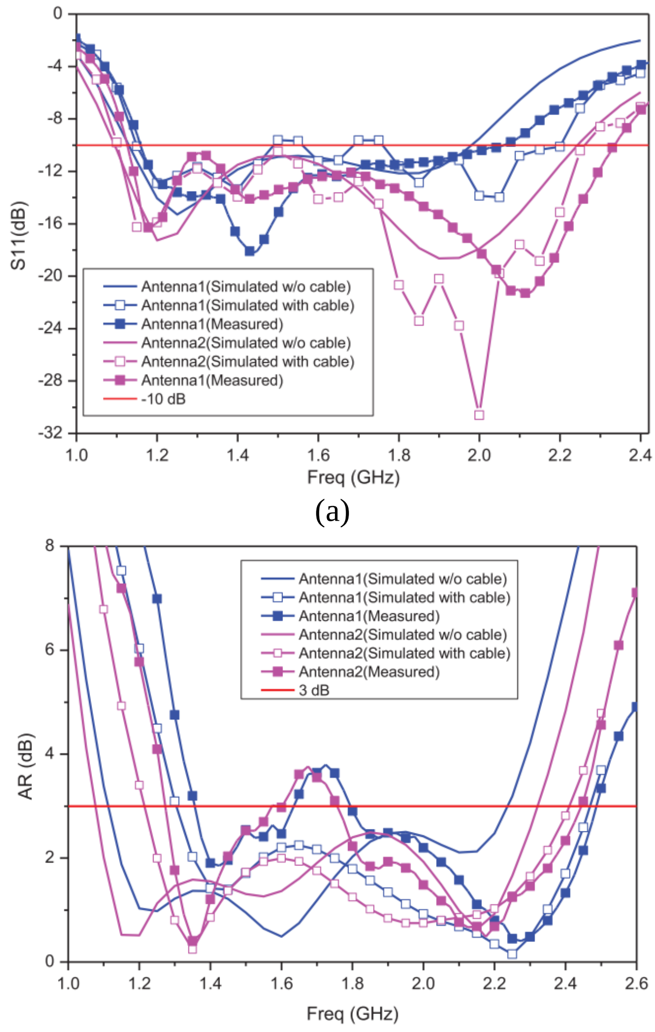

(a)

(b)

Figure 3.6: Simulated and measured (a) reflection coefficient and (b) axial ratio [59].

3.3 GNSS CROSSED-DIPOLE ANTENNA

S. X. Ta *et al.* [56] have proposed a multi-band, RHCP, crossed, multi-branch, barbed dipole antenna with a broad impedance-matching bandwidth, and a high front-to-back ratio in the GPS L1 - L5 bands. The multi-branch barbed dipole with a meander line in each branch is used to achieve not only multiple resonances but also a significant reduction in the radiator size. A vacant quarter printed ring is used as a 90° phase delay line to generate the CP radiation.

Along with the development of wireless communications, many applications require antennas that radiate a unidirectional pattern with a significant front-to-back ratio to ensure high security and efficiency in the propagation channels. Accordingly, the crossed dipole is generally equipped with a reflector to generate a desired unidirectional pattern with CP or dual polarization [83].

The antenna is composed of two printed dipoles, a coaxial line, and a reflector. The reflector is an inverted pyramidal cavity with a rectangular bottom measuring 120 × 120 mm^2, a top aperture measuring 160 × 160 mm^2, and a height of 40 mm as shown in Figure 3.7.

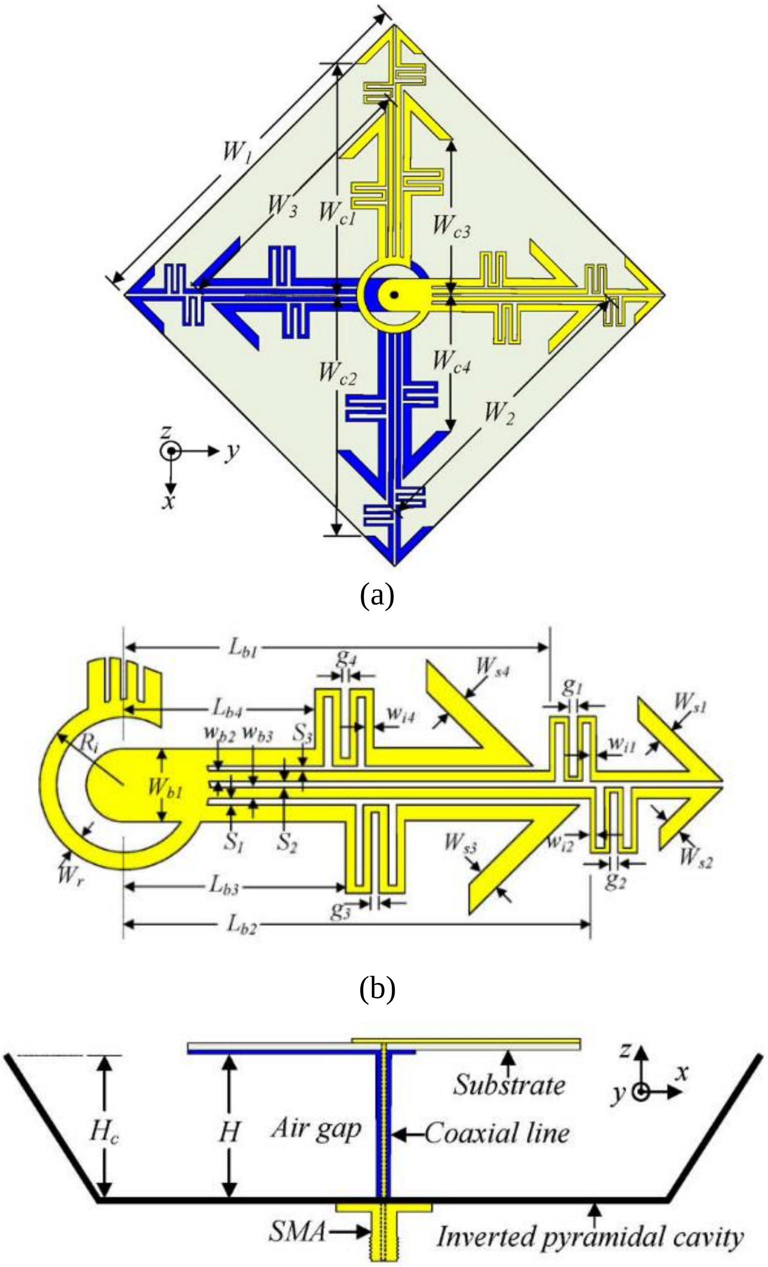

(a)

(b)

(c)

Figure 3.7: Geometry of the proposed antenna (a) radiator (b) vacant-quarter printed ring and dipole arm (c) side view with the inverted pyramidal cavity [56].

The crossed dipole was designed on both sides of a 60 × 60 mm^2 Rogers RO4003 substrate with permittivity of 3.38 and thickness of 0.508 mm. The outer conductor of the coaxial line is connected to the arms on the bottom side of the substrate. The inner conductor of the coaxial line extends through the substrate and connects to the arms on the top side. The crossed dipoles are equipped with a cavity-backed reflector to provide a unidirectional radiation pattern with a wide AR beamwidth and a high front-to-back ratio in both bands.

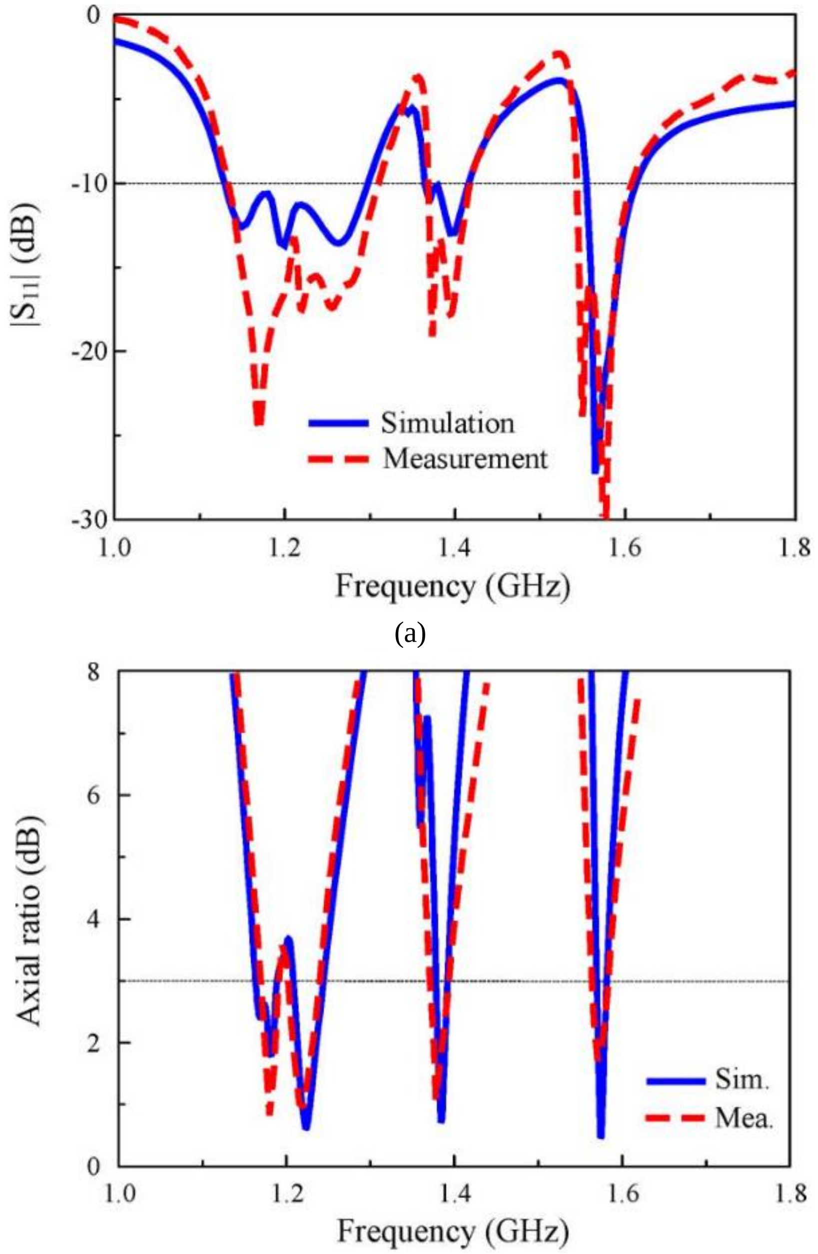

(a)

(b)

Figure 3.8: Simulated and measured (a) reflection coefficients (b) axial ratios of the multi-band antenna [56].

The proposed antenna has bandwidths of 1.131–1.312 GHz (181 MHz), 1.369–1.421 GHz (52 MHz), and 1.543–1.610 GHz (67 MHz) for impedance matching with $|S_{11}| < -10$ dB and 1.165–1.190 GHz (25 MHz), 1.195–1.240 GHz (45 MHz), 1.370–1.395 GHz (25 MHz), and 1.565–1.585 GHz (20 MHz) for an AR of < 3dB as shown in Figure 3.8.

On the other hand, [84] reported a novel composite cavity with unequal-length crossed fins is designed and integrated with the antenna to enhance the front-to-back ratio (FBR) of the antenna. It is well known that the surface wave propagating along the ground plane reradiates at the ground plane edge and thus increases the side-lobes as well as the back lobe of the antenna. Therefore, suppressing the propagation of surface waves can reduce the back lobe of the antenna.

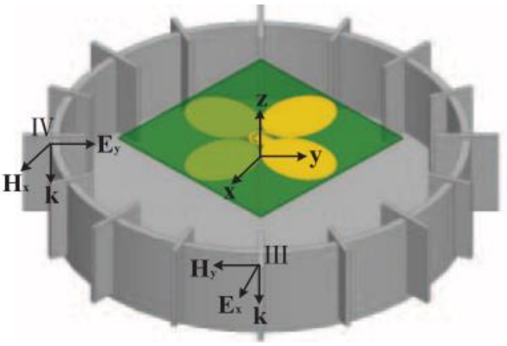

Figure 3.9: Geometry of the proposed antenna with a composite cavity [84].

The antenna is etched on a 0.817 mm thick Rogers RO4003C substrate with a relative permittivity of 3.55 and a loss tangent of 0.0027. Furthermore, the patches are employed to tune the impedance matching of the proposed antenna by introducing proper capacitance. Similar to the conventional crossed dipole CP antenna, the proposed antenna radiates in bidirectional that makes RHCP toward the broadside and LHCP backward. The proposed composite cavity placed underneath the antenna shows better back lobe reduction ability by minimizing diffracted waves.

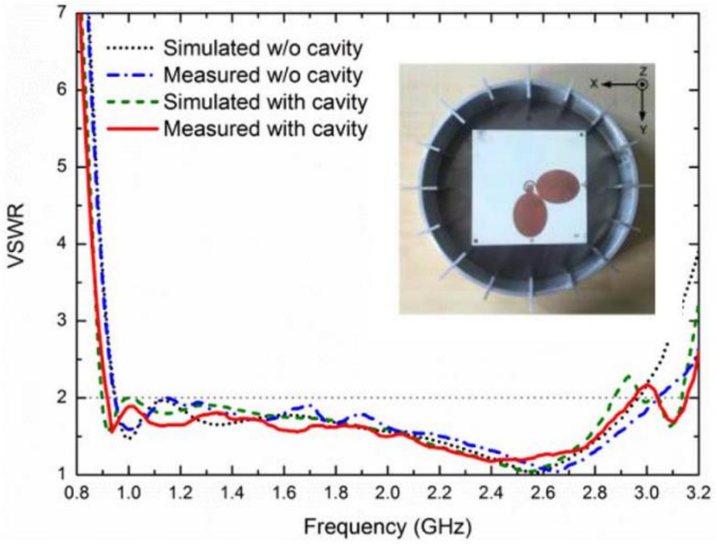

(a)

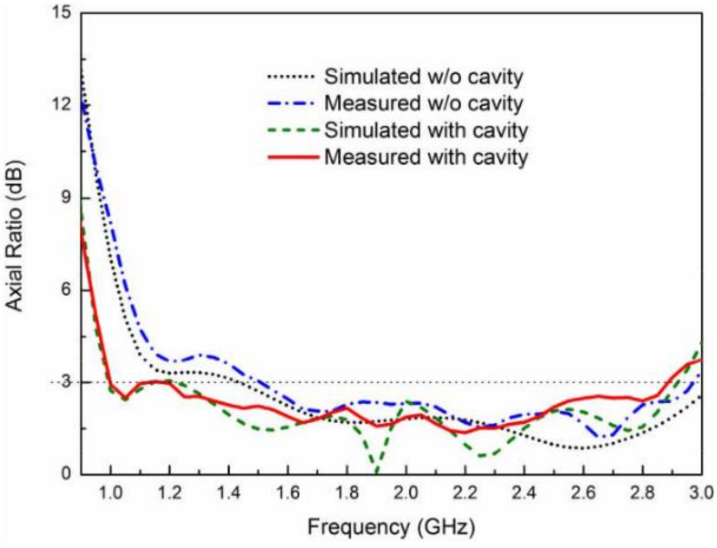

(b)

Figure 3.10: (a) Prototype of ultra-wideband composite cavity backed CP antenna and VSWR and (b) simulated and measured ARs of the antenna with and without a cavity [84].

3.4 GNSS ADAPTIVE ANTENNA ARRAYS

Modern GNSS receivers require antennas that cover wider bandwidths over a wider range of frequencies than older GPS-only antennas. One way to achieve greater bandwidth is to employ wideband antenna designs, such as bowtie dipoles or spiral antennas. Unfortunately, these antennas tend to be relatively large in size [85]–[87]. A critical challenge with these smaller antennas is the feed structure, which must achieve RHCP radiation, employ simple materials and bonding, and must be affordable. Therefore, it is important to employ readily available materials, and non-contact proximity feeds, as was done in [88] and [89].

The 33 mm diameter tri-band GNSS antenna and associated anti-jamming GNSS array in [88] were among the first proximity excited multiband antennas to be presented. It was fed by a single coaxial cable leading to a Wilkinson power divider together with a quarter-wavelength delay for CP.

The antenna is a stacked patch, a six- element version of the array with 114 mm in diameter. Its geometrical configuration is shown in Figure 3.11, indicating two stacked circular patches printed on different substrates material. The antenna was designed to support two orthogonal modes that combine to deliver a CP operation.

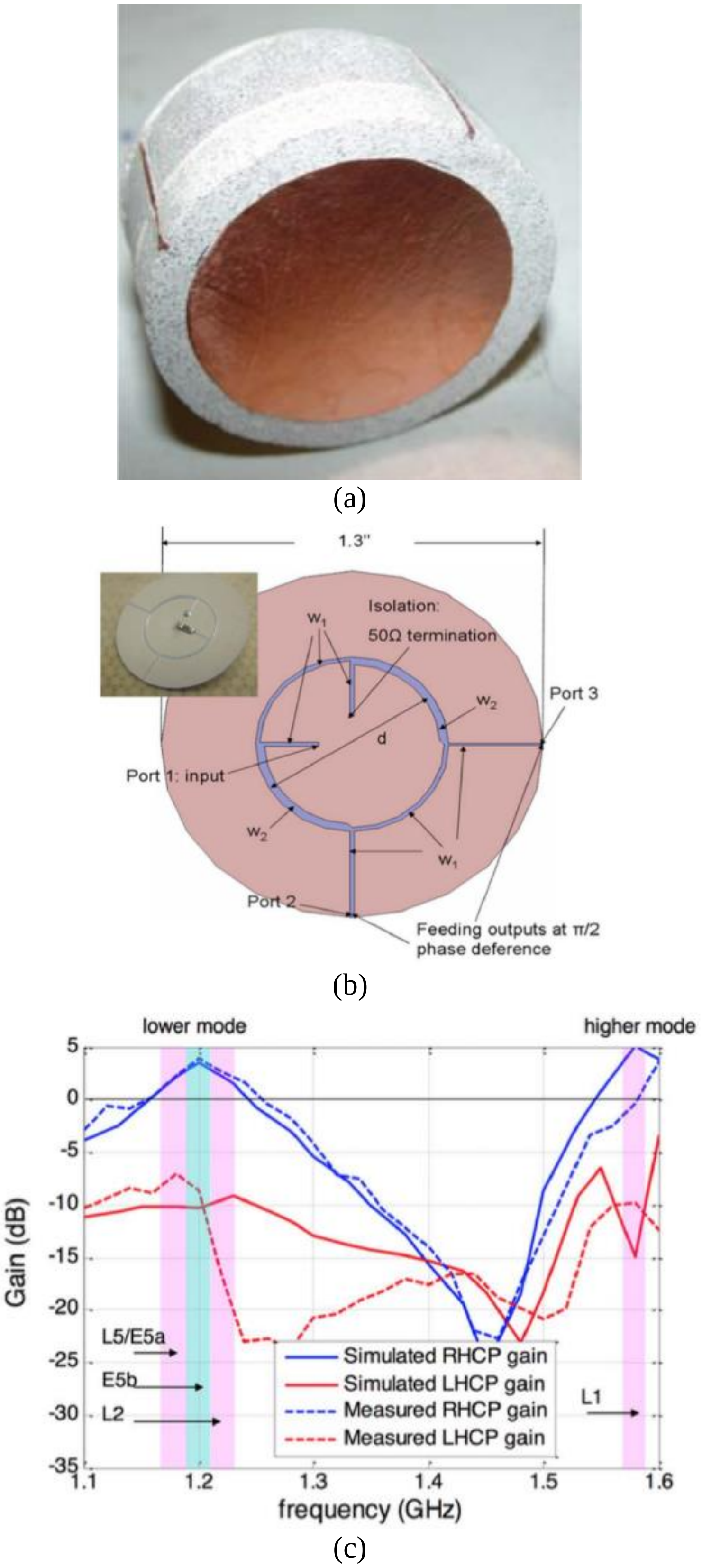

Figure 3.11: (a) Prototype using high-contrast substrates and (b) associated Wilkinson divider for feeding using a single coax feed at Port 1 and (c) gain of the patch [88].

The geometrical parameters for the feed in Figure 3.11 (b) that were found to achieve good gain at all frequencies are: D = 33 mm, d_1 = 26 mm, d_2= 22 mm, h_1 = 6mm, and h_2 = 8 mm. Figure 3.11 also shows the boresight gain curves, which show 2.5 dBi to 5 dBi at the lower (L5/ E5a, E5b, and L2) and higher (L1) bands.

Referring to Figure 3.11, this GNSS antenna covers all said bands and has the following optimized parameters. The simulated and measured gain performance is shown in Figure 3.11 (c). Its gain in the bands of interest is always greater than 0 dB and even reaches more than 4 dBi at some bands. Specifically, the lower mode of the stacked patches covers the L5/ E5a, E5b, and L2 bands with RHCP gain above 3-dB, whereas the high mode covers the L1 band with a gain of 5 dBi.

For the array formation, the antenna in Figure 3.11 was used to form a six-element circular array shown in Figure 3.12. Key to this performance is coupling reduction between adjacent antenna elements within the array.

For smaller array sizes, it is important to reduce the antenna element size even further than shown above. A 25 mm GNSS antenna element was first presented by Zhou et al. [90]. Instead of using higher-contrast dielectric substrates that would reduce bandwidth, slots are introduced on the printed surface of the GPS antenna. A similar concept was introduced in [91] and [92] adopted four spiral slots to design a proximity-fed dual-band stacked patch.

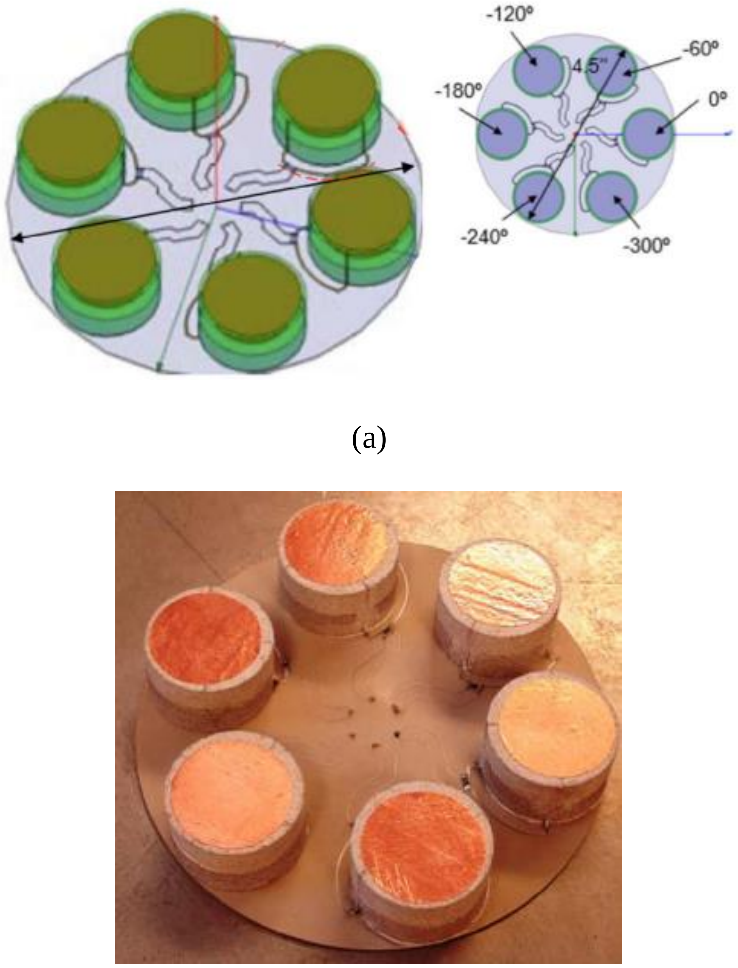

(a)

(b)

Figure 3.12: (a) GNSS antenna array design and (b) fabricated prototype [88].

Kasemodel et al. [85] and Svendsen et al. [93] presented a spiral array antenna capable of continuous operation from 1.1 to 1.6 GHz. The array is shown in Figure 3.13. The array is designed to be placed on a ground plane, making it suitable for mounting on small vehicles. In [85], the dielectric layer is formed from a polymer, allowing precise control of its dielectric constant while also reducing weight and increasing mechanical durability as compared to more rigid and brittle dielectric materials.

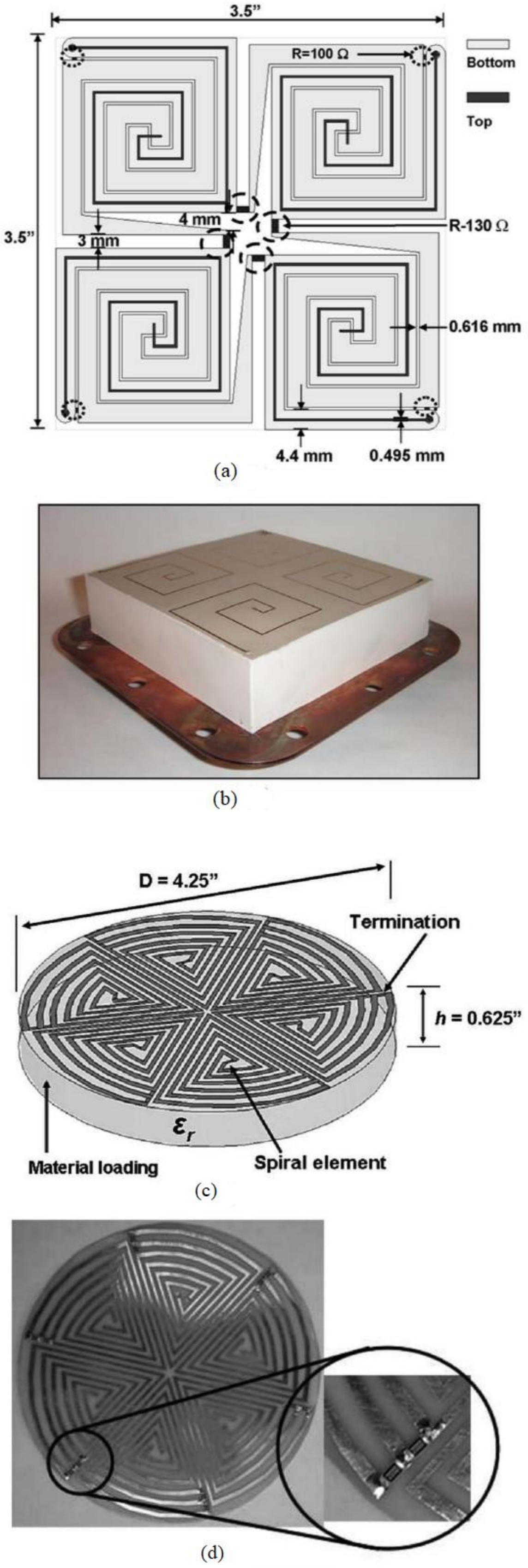

Figure 3.13: Four-element and six-element spiral array [85], [93].

The array elements are connected in the center with resistors, and ferrite beads are used to terminate the spiral arms. These techniques improve return loss and axial ratio while maintaining good gain and upper hemispherical coverage. In the absence of interference, the array is designed to operate in a reference mode where all elements are excited with equal weight and progressive phase. This produces a rotationally symmetric boresight pattern with RHCP polarization. The densely packed array produces significant mutual coupling between elements. However, the array has been designed with each element effectively exciting the entire aperture. The small size of the array and the wideband nature of the spiral results in desirable phase and delay characteristics.

Meanwhile, in [93] altered the square spiral array in [85] and presented a dual-band array for handheld GPS receivers. Handheld applications are more challenging since the antenna array must be extremely lightweight, be very robust, occupy a small volume, be inherently portable, and be easy to fabricate. The array presented in consists of a tightly packed 2 × 2 array of square spiral elements that form a small, 4 × 4 inch^2 (102 × 102 mm^2) aperture that can flip out from a handheld receiver. Again, the array operates in a reference mode with no interference. The resulting RCHP polarized pattern is broad with good peak realized gain. The authors show simulations of the antenna performance with space-time adaptive processing (STAP). They demonstrate their ability to operate in scenarios with several narrowband and wideband interference sources.

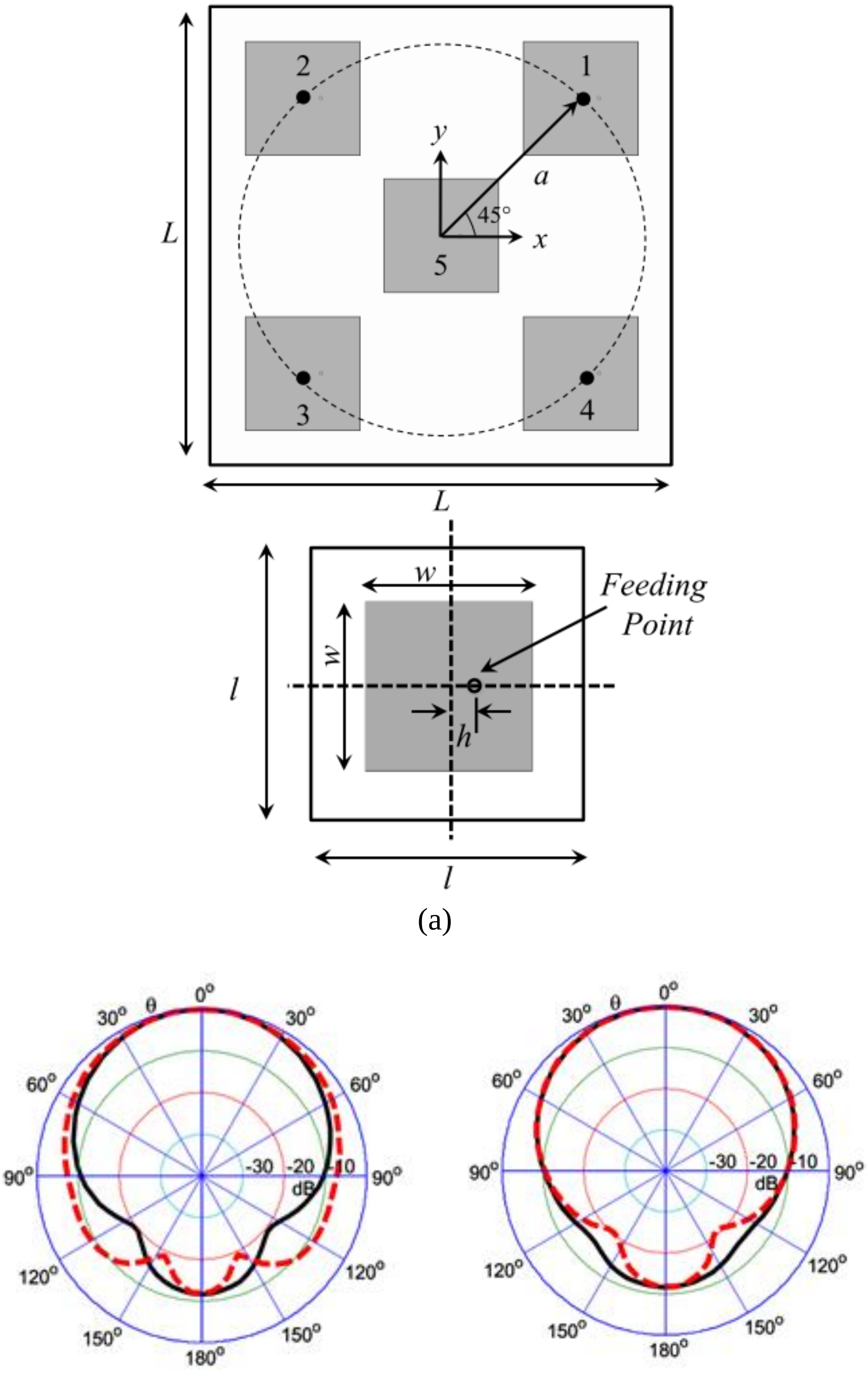

(a)

(b)

Figure 3.14: (a) Antenna array geometry formed by five identical patch antennas and (b) radiation pattern at φ = 0° and φ = 90° [94].

A recent study by [94] has proposed a new method to extract the optimal complex weights for suppression of the jamming signals in a GPS antenna array in the presence of mutual coupling. The proposed antenna array geometry is shown in Figure 3.14. All patch antennas are printed on a square RO4003 substrate with a length of L = 20 cm, 30 mm thickness and relative permittivity of ε_r = 3.55.

The full wave simulation patterns of the standalone GPS antenna element and the reference active element patterns in the array (fifth elements) is shown in Figs. 3.14(a) and (b). It shows the normalized antenna radiation patterns comparison at φ = 0, 90° planes where the antenna gain is 5.24 and 3.94 dB for the stand alone and reference antennas, respectively. The null steering method was performed by using the exact active element patterns of the array antenna. These patterns include the mutual coupling effect and the nearby antenna scattered such as holder which increase the antenna performance to deal with the jammer sources which was not considered in the literature based on the author knowledge.

3.5 SUMMARY

Nevertheless, we can summarize the basic antenna types applicable to GNSS, and a broad overview of their characteristics, in Table 3.1.

Table 3.1: Basic Antenna Typed Used in GNSS System and Their General Characteristics

Ref.	**Antenna Structure**	**Size (mm^3)**	**$\lvert S_{11}\rvert$<-10dB BW**	**Axial Ratio BW**
Ref [76]	DRA	90 × 90 × 51.6	L1, L2, L5	1 to 1.6 GHz
Ref [69]	Stacked Patch Antenna	80 × 80 × 6.024	1.51-1.59 GHz (L1) 1.2-1.245 (L2) 1.168-1.185 (L5)	3.19% (L1) 3.04% (L2) 2.21% (L5)
Ref [72]	-Stacked patched antenna -dual feed + hybrid design	90 × 90 × 8.135	1.17 to 1.6 GHz (L1, L2, L5)	1.47 to 1.63 GHz (L1) 1.15 to 1.33 GHz (L2, L5)
Ref [77]	DRA + hybrid feeding network	160 × 160 × 23	1.125 to 1.625 GHz (L1, L2, L5)	<1.5 dB (L1, L2, L5)
Ref [64]	DRA + feeding network	250 × 250 × 50	1.164 to 1.614 GHz (L1, L2, L5)	<3 dB (L1, L2, L5)
Ref [59]	Monopole antenna	88 × 88 × 1.6	1.122 to 2.344 GHz (L1, L2, L5)	1.27 to 1.6 (L1)

Ref [57]	Crossed-dipole antenna	120 × 120 × 30.55	1.274 to 2.360 (L1, L2)	1.39 to1.82 GHz (L1, L2)
Ref [55]	Crossed-dipole antenna	120 × 120 × 40	1.555 to 1.665 GHz (L1) 1.220 to 1.385 GHz (L2)	1.565 to 1.595 GHz (L1) 1.260 to 1.300 GHz (L2)
Ref [95]	Crossed-dipole antenna	120 × 120 × 62.5	1.05 to 1.79 (L1, L2, L5)	1.12 to 1.64 GHz (L1, L2, L5)

In this chapter, some significant achievements in GNSS antenna technologies have been reviewed. It has been clearly shown that the research of GNSS antenna is of great significance to the modern industry and it will still be an important research topic for the coming decades. The studies of antenna for GNSS applications have been highlighted and discussed in detail. It was found that most existing antennas in the literature have not been focused on broadband antennas due to the difficulty and complexities in the design. The information presented in this chapter is useful to gain a better understanding on the state of art in antenna designs and meanwhile identify the research challenges and problems for us to overcome in this work.

CHAPTER 4:

A CROSSED-DIPOLE ANTENNA WITH PARASITIC ELEMENTS

4.1 INTRODUCTION

With the deployment of a few noteworthy Global Navigation Satellite Systems (GNSSs) for example GPS, GLONASS, COMPASS and many more frequency bands will be accessible for positioning applications. GNSS applications have multiplied internationally, not only in the military field but also in business and consumer markets.

Global positioning systems typically transmit in CP due to its features of non-sensitive to Faraday rotation introduced by the ionosphere and its potential of reducing polarization mismatch and multipath interferences. Different designs of single and dual-band CP antennas in the GNSS frequency bands have been reported:

e.g., crossed dipole [58], monopole [59], slotted [64], [65], stacked patch [69], [70] and dielectric resonator [75]–[77] antennas. Nevertheless, almost all these antennas have inadequate 3-dB AR bandwidth to meet the requirements of GNSS applications, due to the lack of techniques to broaden the CP radiation bandwidth. Recently, single-feed CP antennas with a compact radiator have been designed for GNSS applications [55], [56]. However, their operational bandwidth does not completely cover the GNSS spectra.

This chapter presents a broadband and broad beamwidth circularly polarized antenna to cover the GPS L1-L5 bands, GLONASS G1, G2 and G3 as well as the Galileo E5a, E5b, E6 and E1bands (1.08 GHz – 1.69 GHz). A printed vacant-quarter ring is used as a 90-degree phase delay line between the dipole pair to produce the CP radiation. The detailed dimensions are presented, and good results are obtained. The CST Microwave Studio is employed for the numerical simulation.

4.2 AN ANTENNA WITH PARASITIC ELEMENTS

4.2.1 Antenna Design Configurations

Figure 4.1 and Table 4.1 show the geometry and the dimension of the proposed broadband CP antenna, respectively. The antenna comprises two printed cross dipoles and a coaxial line. The dipoles are printed on both sides of a Rogers RO3210 substrate with a relative permittivity of 10.2 and thickness of 1.28 mm.

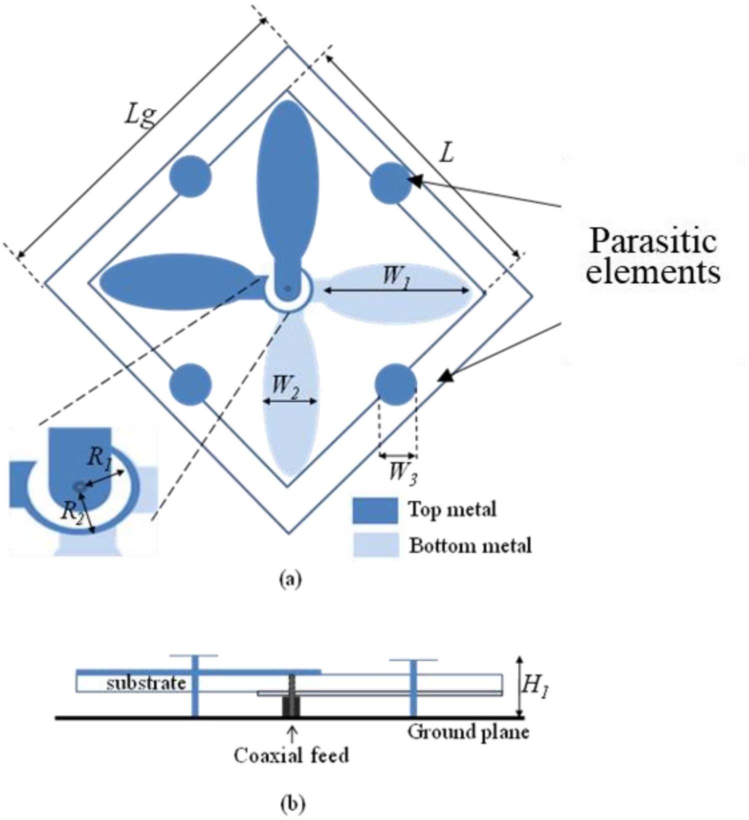

Figure 4.1: Geometry of the proposed antenna: (a) top view and (b) side view.

Table 4.1: Dimension of The Proposed Antenna

Parameter	**Value (mm)**	**Parameter**	**Value (mm)**
L_g	90.0	L	66.0
R_1	4.7	R_2	5.5
W_1	20.0	W_2	8.0
W_3	8.5	H_1	15.5

The proposed antenna is designed to meet the needs of multiple GNSS. The critical part is the feeding structure which is relatively new, and the dimensions should be optimized. The elliptical cross-dipole antenna is produced on both sides of the PCB board. The antenna was fed with a 50 Ω coaxial line. The outer conductor of the coaxial line was connected to the dipole arms on the bottom side of the substrate while the inner conductor of the coaxial line was extended through the substrate and connected to the dipole arms on the top side.

The pair of dipoles is linked by a vacant quarter printed ring to generate 90° phase delay line and produce the RHCP radiation field at the front side of the antenna and the LHCP radiation field at the back side. The reason of choosing the cross-dipole in this design are the impedance bandwidth of the cross-dipole is much broader than a conventional microstrip patch antenna, and it is much easier o generate the CP radiation and obtain a broader CP bandwidth by using the feeding mechanism as mentioned above.

Furthermore, the antenna is composed of four parasitic element and four metallic cylinder that are excited by coupling with the elliptical crossed dipole in the center. Figure 4.2 shows the theory of how to broaden the beamwidth. The ordinary microstrip antenna radiates mainly towards the elevation angle of 90°. Meanwhile, the crossed dipoles radiate mainly towards the elevation angle of 0°. Therefore, when the ordinary microstrip antenna is combined with the loaded monopoles, the two-elevation angle of highest gain of the two radiation patterns could be merged into one, and their radiation fields are added together, forming a broad radiation pattern in both the X_oZ and Y_oZ planes. Based on this theory and our numerical simulations, the vertical half power beamwidth (HPBW) of the microstrip antenna could be widened.

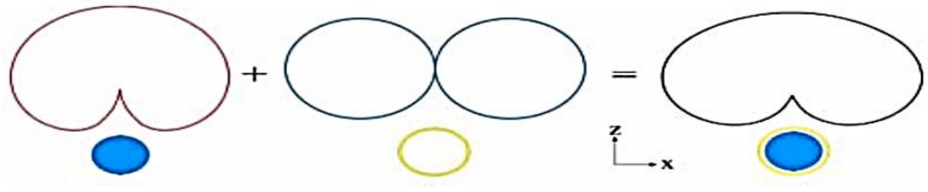

(a) (b) (c)

Figure 4.2: Vertical radiation patterns for the antennas. (a) elliptical cross-dipole (b) parasitic element and loaded monopole and (c) crossed dipole surrounded by parasitic elements and monopoles.

By adjusting the size of the parasitic elements and the edge of the dipoles, the coupling strength can be optimized. The antenna was optimized via CST Simulation Software. For the initial design of the proposed antenna, it was first to design in free space to provide resonance in the GPS L1 and L2 bands.

4.2.2 Antenna Performances

The simulated S_{11}, axial ratio and gain of the antenna with different values of the ground plane length L_g are depicted in Figures 4.3 to 4.4, respectively. The bandwidth of the antenna for S_{11} < -10 dB is improved by reducing the size of the ground plane. The impedance bandwidth of the antenna covers from 1.08 to 1.69 GHz when the size of ground plane is 90 mm × 90 mm which is completely cover the entire GPS bands (L1: 1.575 GHz, L2: 1.227 GHz, L3: 1.381 GHz, L4: 1.379 GHz and L5: 1.175 GHz) and Galileo (E1; 1.575 GHz, E5: 1.191 GHz and E6: 1.279 GHz).

Meanwhile, the CP bandwidth (AR < 3-dB) shows a decrease at the lower frequency when the size of the ground plane is reduced, but at the upper frequency bands, the axial ratio is reduced. It covers from 1.55 to 1.63 GHz which involves the L1 and E1 frequency bands and from 1.12 to 1.26 GHz for L2, L5, and E5.

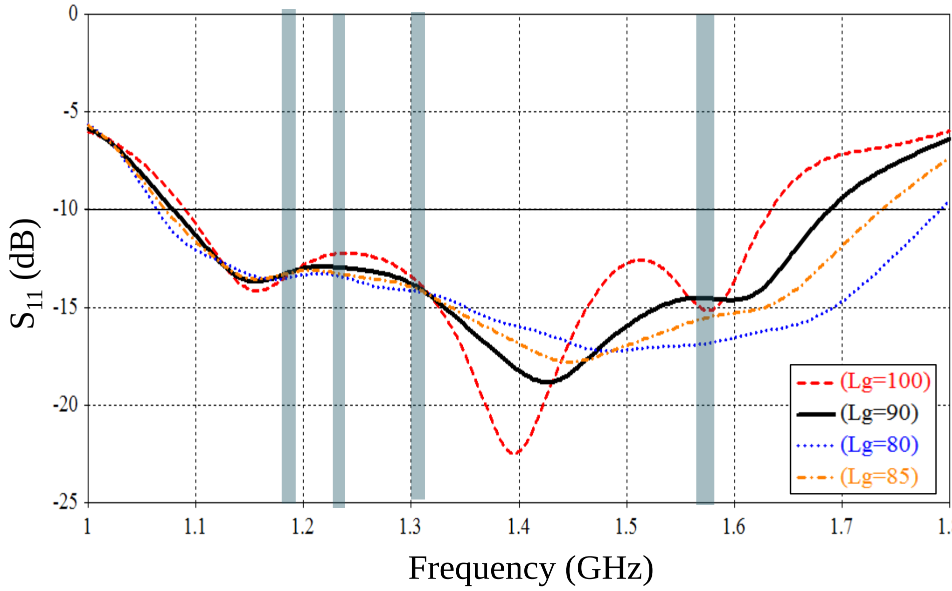

Figure 4.3: The simulated S$_{11}$ with different values of L_g of the proposed antenna.

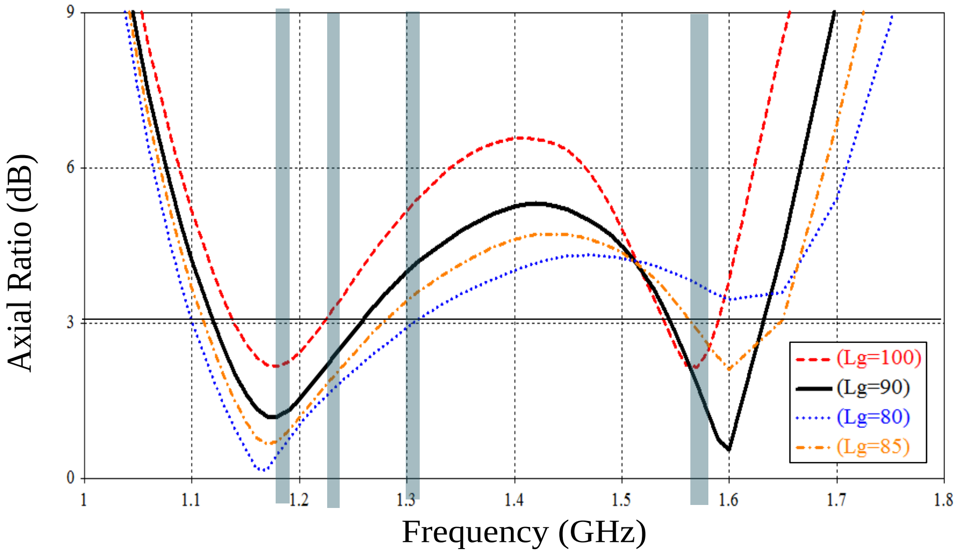

Figure 4.4: The simulated axial ratio with different values of L_g of the proposed antenna.

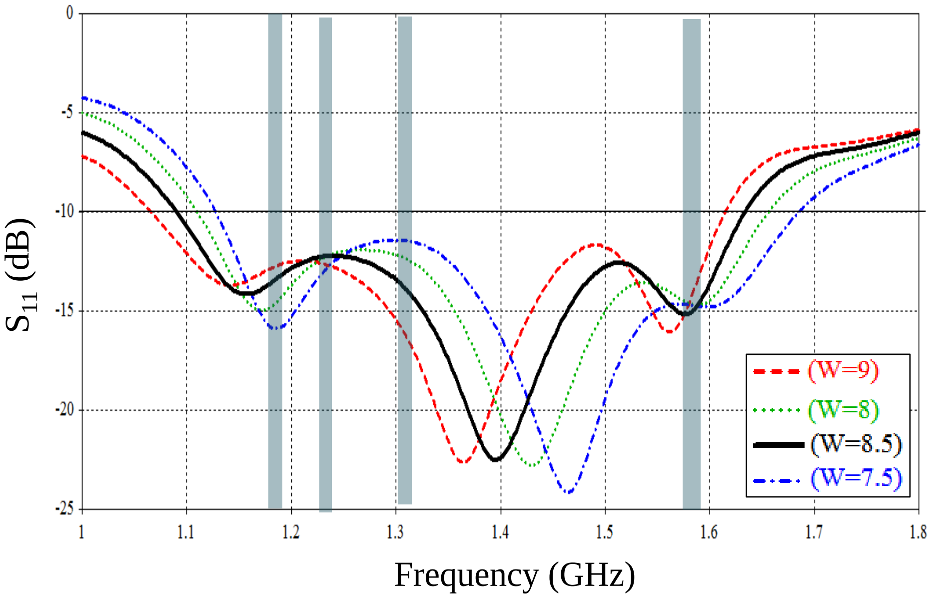

Figure 4.5: The simulated S_{11} with different values of *W* of the proposed antenna.

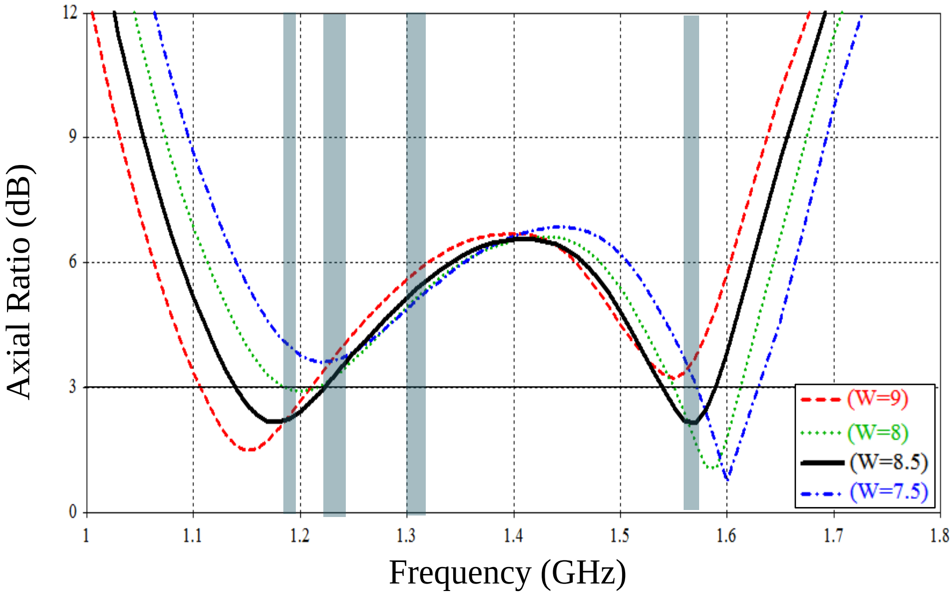

Figure 4.6: The simulated axial ratio with different values of *W* of the proposed antenna.

In another case, the antenna also simulated with different values of W_3 which is the radius of a parasitic element at the upper cylinder. The simulated results of S_{11}, axial ratio and gain are presented in Figure 4.5 and Figure 4.6. It is shown that the impedance bandwidth of the antenna did not change much, but the resonant frequency seems to be shifted to the higher frequency bands when the radius of the parasitic element is too small.

However, as shown in Figure 4.6, the CP bandwidth (AR < 3-dB) is highly sensitive to the variation of the parasitic element size. The axial ratio decreased when the size of the parasitic element is enlarged at the lower frequency. Meanwhile, at the upper frequency bands, the axial ratio decreased when the size of the element reduced. The optimal value of *W* is 8.5 mm to cover the desired bandwidth. Thus, as shown in Figure 4.6, when *W* = 8.5, the CP bandwidth for AR < 3-dB is from 1.13 to 1.22 GHz for L2, L5, and E5 bands and from 1.53 to 1.59 GHz for L1 and E1 bands.

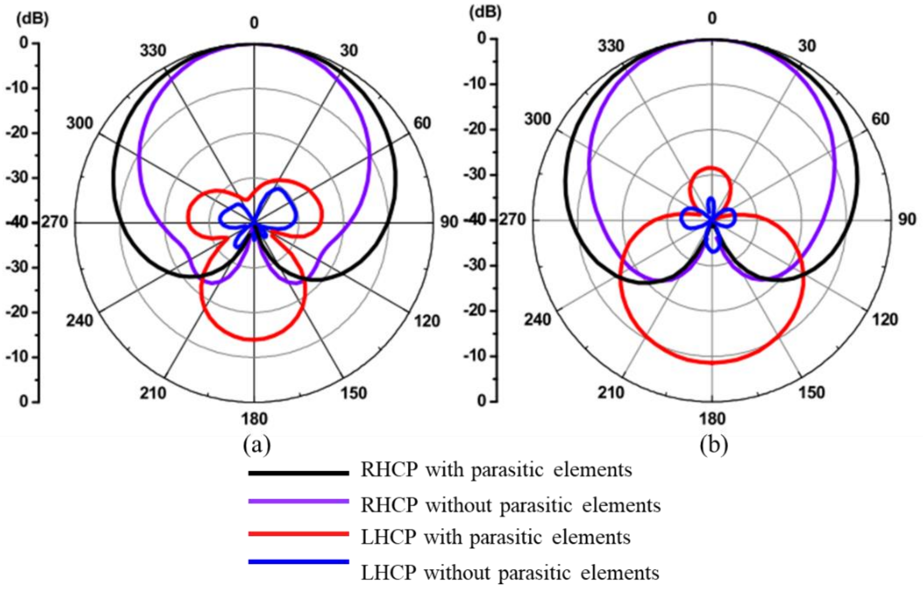
(a) (b)

Figure 4.7: The simulated radiation pattern with and without the parasitic elements of the proposed antenna at (a) GNSS L2 (b) GNSS L1.

The simulated radiation patterns are demonstrated in Figure 4.7, indicating that hemispherical shape radiation patterns with good symmetry is obtained. It can be seen that the radiation pattern is greatly enhanced by the introduction of the parasitic elements for both operating bands.

Figure 4.8 presents the RHCP radiation patterns in two orthogonal planes. For both the X_oZ and Y_oZ planes, the HPBW is more than 170°. The operation at other frequencies is given in Table 4.2. At each frequency, the antenna shows a wide angular coverage for both HPBW and 3-dB axial ratio beamwidth.

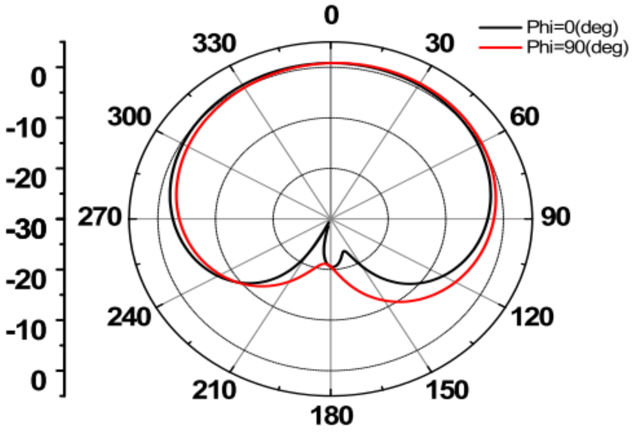

Figure 4.8: RHCP radiation patterns in X_oZ and Y_oZ planes at 1.575 GHz.

Table 4.2: 3 dB Beamwidth of The Proposed Antenna

Frequency band	**HPBW (deg)** X_oZ / Y_oZ	**3-dB axial ratio beamwidth (deg)** X_oZ / Y_oZ
GNSS: L1	172 / 170	157 / 140
GNSS: L2	120 /120	140 / 120
GNSS: L5	180/174	134 / 156

The final design was fabricated and measured. The comparison of the simulated and measured reflection coefficients of the fabricated antenna is shown in Figure 4.9 (a) and (b). The antenna was measured in an anechoic chamber using a vector analyzer. The simulated and measured reflection coefficients of the antenna are depicted in Figure 4.10.

It can be seen that the results agreed reasonably well within the bandwidth. The $|S_{11}| < -10$ dB measured bandwidths of the lower and upper bands were merged, and the result ranged from 1.060 to 1.671 GHz. The simulated bandwidths were 1.077–1.683 GHz. Figure 4.11 shows the simulated and measured axial ratio of the proposed antenna. It can be seen that a very good agreement was obtained between simulation and measurement. The CP bandwidth AR < 3-dB is from 1.093 to 1.257 GHz (164 MHz) and 1.542 to 1.666 GHz (124 MHz) as expected.

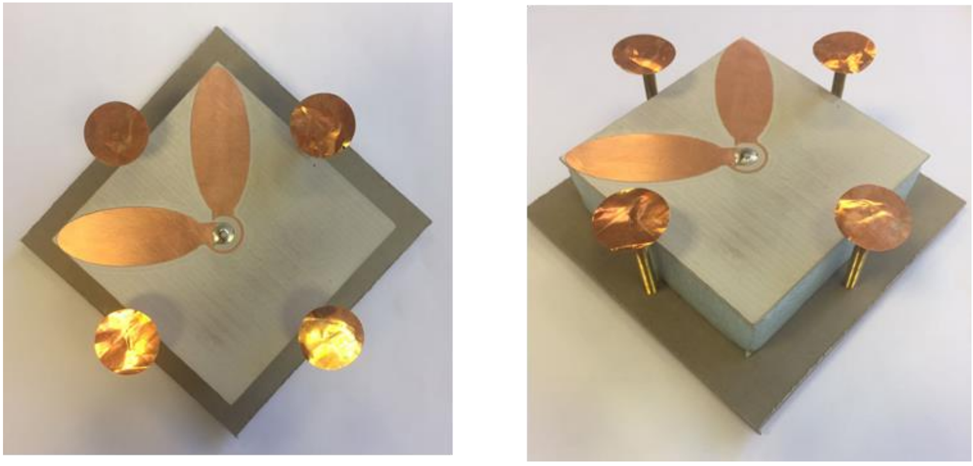

(a) (b)

Figure 4.9: Photograph of fabricated antenna (a) front view and (b) perspective view.

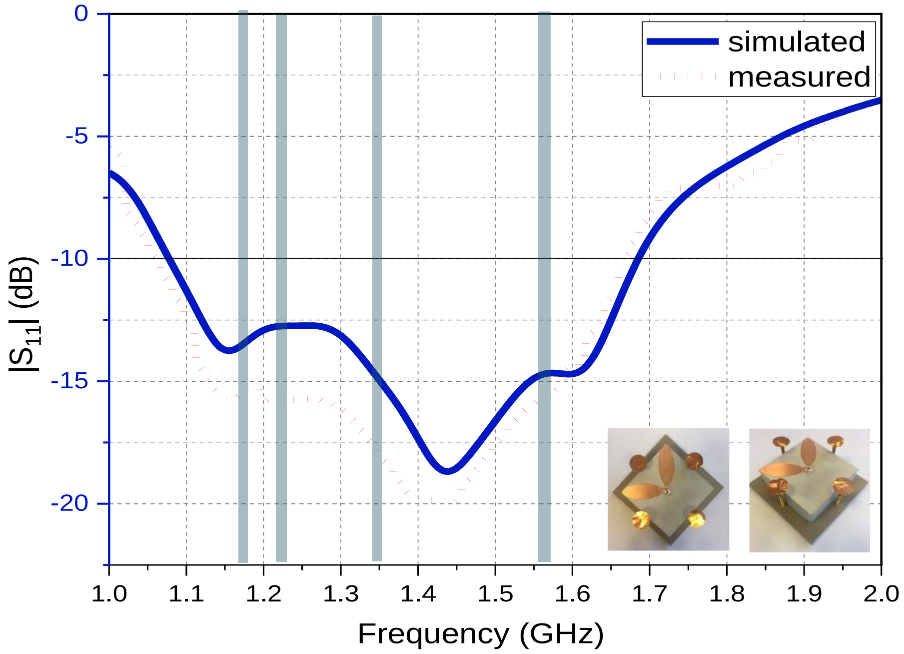

Figure 4.10: Measured and simulated results of the proposed antenna: $|S_{11}|$.

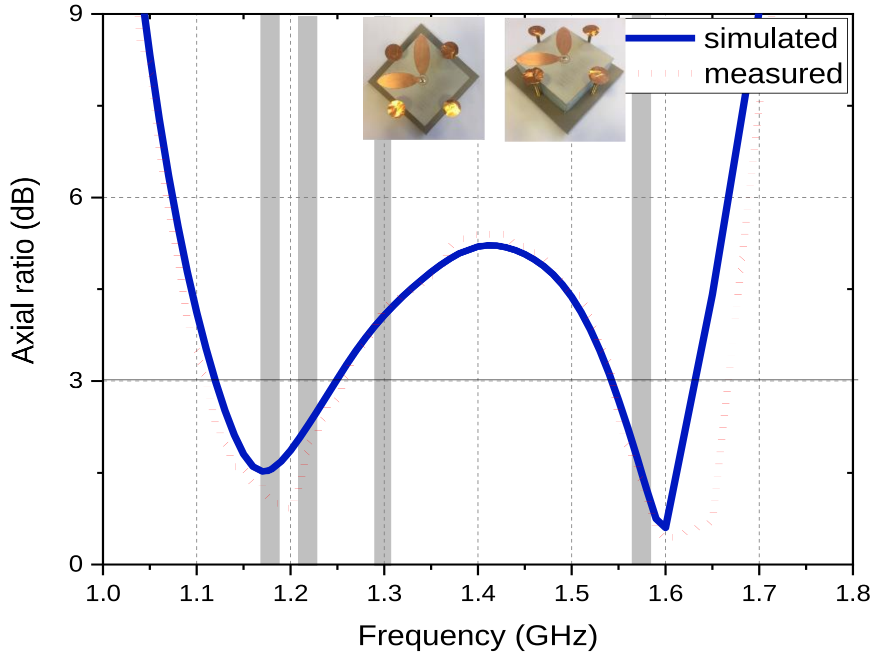

Figure 4.11: Measured and simulated results of the proposed antenna: AR.

4.3 SUMMARY

A new broadband cross-dipole antenna has been proposed and designed for the GNSS applications. The impedance bandwidth is very broad to cover the entire GPS, Galileo, and GLONASS bands. The structure of the antenna is compact and unique. The dimension of the antenna is 90 mm × 90 mm × 15.5 mm which is small and compact. The proposed antenna has bandwidth of 1.06 to 1.671 GHz (611 MHz) for impedance matching $|S_{11}| < -10$ dB and 1.093 to 1.257 GHz (164 MHz) and 1.542 to 1.666 GHz (124 MHz) for an AR < 3-dB. All the results have demonstrated that the antenna is an excellent candidate for the GNSS application.

Table 4.3: Comparison with Existing GNSS Antenna Designs

Ref.	**Size (mm^3)**	**$\|S_{11}\|$ <-10 dB BW (GHz)**	**Axial Ratio BW (GHz)**	**Antenna Type**
Ref [16]	160 × 160 × 23	1.125 to 1.625 (L1, L2, L5, E6)	<1.5dB (L1, L2, L5)	DRA + hybrid feeding network
Ref [5]	88 × 88 × 1.6	1.122 to 2.344 (L1, L2, L5, E6)	1.27 to 1.6 (L1, E6)	Monopole antenna
Ref [3]	120 × 120 × 30.55	1.274-2.360 (L1, L5)	1.39-1.82 (L1)	Crossed-dipole antenna
Proposed Antenna	**90 × 90 × 15.5**	**1.06 to 1.671 (L1, L2, L5, E6)**	**1.093 to 1.257 (L5, L2)** **1.542 to 1.666 (E6)**	**Crossed-dipole antenna**

In order to evaluate the achievements of the proposed antenna with respect to available designs, the proposed antenna is compared with recently published designs as tabulated in Table 4.3.

CHAPTER 5:

A CIRCULARLY POLARIZED ANTENNA BACKED BY AN AMC GROUND PLANE

5.1 INTRODUCTION

Artificial Magnetic Conductor (AMC) is a type of implemented metamaterial in several antenna and microwave design applications. By utilizing the unique characteristics of metamaterials which do not exist naturally, the performance of various microwave devices can be enhanced. This chapter elaborates on the technical perspective and recent works on AMC for antenna applications. The technical perspective discusses the theoretical aspects, simulation design procedures, and the measurement setup used to characterize the AMC unit cell. Subsequently, various recent works of antenna design that involve the incorporation of AMC are discussed thoroughly. Each of the recent works is highlighted with specific performance enhancements that can be achieved with the introduction of AMC.

5.2 ARTIFICIAL MAGNETIC CONDUCTOR (AMC)

AMC is a metamaterial which mimics the characteristics of a perfect magnetic conductor (PMC). A useful PMC characteristic that mimicked by AMC is the ability to provide zero-degree reflection phases at its resonant frequency[96]. Electromagnetic band gap (EBG) technology has become a significant breakthrough in the radio frequency (RF) and microwave applications due to their unique band gap characteristics at certain frequency ranges.

Since 1999, the EBG structures have been investigated for improving performances of numerous RF and microwave devices utilizing the surface wave suppression and the artificial magnetic conductor (AMC) properties of these special type metamaterial. Issues such as compactness, wide bandwidth with low attenuation level, tunability, and suitability with planar circuitry all play an important role in the design of EBG structures.

EBG structure can be defined as fabricated periodic elements that may hinder, allow, or confine electromagnetic waves propagation within a specified span of frequencies [97]. These structures are formed by arranging dielectric material and metallic conductors periodically. When plane waves are incident upon an EBG structure, the reflection coefficient phase varies with frequency. At a frequency, the incident wave encounters a reflection phase of zero degrees. At this frequency, the EBG functions as an AMC. This structure when integrated onto a microstrip antenna below the radiating patch functions either as a reflector or as an artificial ground plane [98].

The main problem of an antenna equipped with a metallic reflector is often addressed by including a quarter-wavelength space between the radiating elements and the reflector to obtain optimal antenna characteristics. These can be circumvented by using an AMC surface instead of a metallic reflector. The AMC, which consists of a lattice of metal plates on a grounded dielectric substrate with/without grounding vias, can mimic a perfect magnetic conductor (PMC) over a certain frequency band.

By combining the crossed dipole radiators and the finite AMC surfaces, low-profile multiband CP antennas that are nearly completely matched to a single 50 Ω source and have high radiation efficiencies have been implemented. More interestingly, surface waves propagating on the finite AMC are excited to generate extra operating bands for the radiating system. It was shown that the extra bands could be favorably used to enhance the bandwidth of the antenna.

5.2.1 AMC Properties

AMC-based antennas have been intensely developed for enhancing their performance, including bandwidth and unidirectional radiation pattern with a miniaturized profile. The AMC surface, also known as a high-impedance surface (HIS) [99], an EBGs [97], or a reactive impedance surface [100], can mimic a PMC within a certain frequency range. Therefore, the AMC surface allows for the placement of the antenna in proximity with good impedance matching and highly efficient radiation. In many applications, an antenna works at two different frequencies simultaneously; consequently, the AMC structure requires dual-band operation that can match the antenna’s working frequencies. Many LP antennas on AMC surface [101]–[105] have been presented for dual-band operation, but there are still a limited number of studies on CP antennas loaded with the dual-band AMC structures. Recently, a dual-band LP dipole was designed on a dual-band polarization-dependent EBG surface to realize a dual-band CP antenna [106]. However, its AR bandwidth is insufficient for some applications.

AMCs are used in low-profile microstrip antennas to generally improve their gain and bandwidth [107]–[110] and directivity [111]. Usually AMC cells are fabricated as periodic structures. However, in [112], a multi periodic AMC structure is used to improve gain and also to widen the impedance bandwidth of a planar antenna. In [113], a periodic AMC structure is designed by using genetic algorithm is found to improve the bandwidth of a wideband planar antenna. Sidelobe suppression is also possible with AMC structures as investigated in [114].

In addition, AMC can also be implemented in a resonance cavity antenna as a ground plane to achieve profile reduction by almost one-half, while maintaining high gain performance [115], [116]. Radar cross-section reduction can also be achieved by combining two AMCs which have overlapping bandwidths [117]. These promising improvements on the characteristics of low-profile planar antennas have triggered various investigations on the possible geometries which form the AMC structure.

AMC is also known as High Impedance Surface (HIS) because at its resonant frequency, it exhibits high surface impedance [118]. The surface impedance consists of real and imaginary parts. AMC can be constructed with and without vias connection [118]–[121]. However, for incidence wave normal to the AMC, the vias are not required as there are no currents excited to it [122]. Via is a shorting pin from the metallic patch of AMC unit cells to the ground as shown in Figure 5.1 (a). As shown in the figure, the AMC is consisting of several periodically arranged metallic unit cells of uniform dimensions with individual vias. The equivalent inductance-capacitance presented in the AMC/HIS structure and the circuit model shown in Figure 5.1 (b) and Figure 5.1 (c), respectively.

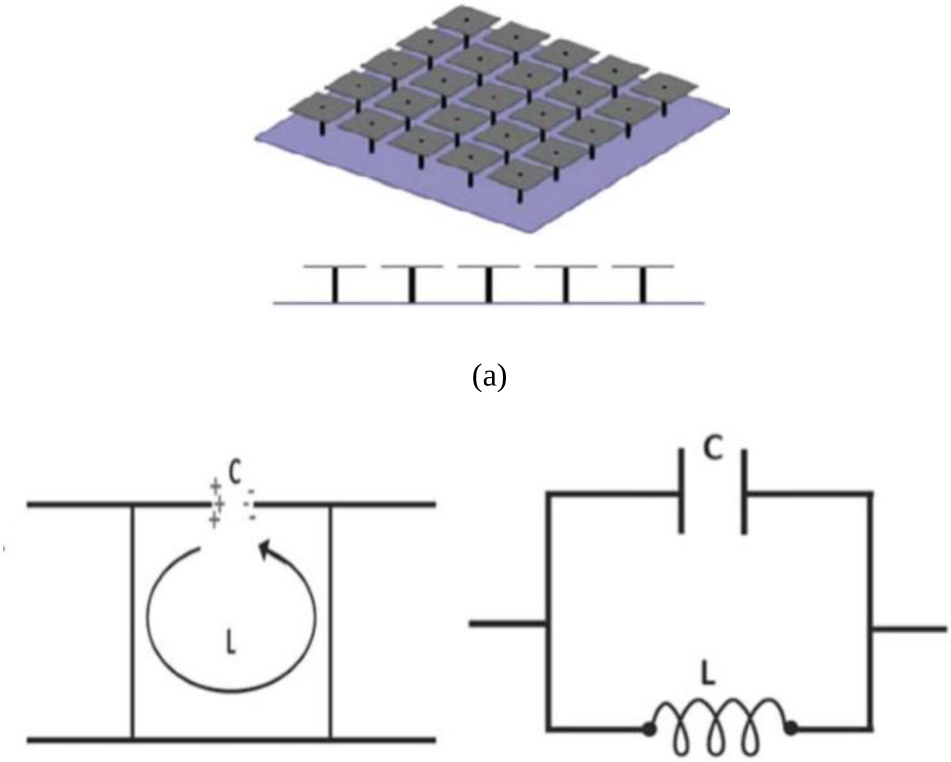

(a)

(b) (c)

Figure 5.1: (a) An array of AMC unit cells with each vias connected to the ground plane, (b)the equivalent inductance capacitance circuit, and (c)circuit model [102].

Conventional antenna tends to use Perfect Electric Conductor (PEC) (or in practical, conductive layer like copper) as a conventional background plane [123].

The PEC layer functions as the reflector of the antenna. However, the drawback of the PEC layer is the produced reflected wave that is 180° out of phase with respect to the source wave, *J* as shown Figure 5.2 (a). The source wave is a wave (wave 1) that initially flows along the radiating part of the antenna. The out of phase reflected wave (wave 2) induces destructive interference with the source wave. This interference cancels out or greatly attenuates the source wave from the antenna, hence reducing its radiation efficiency.

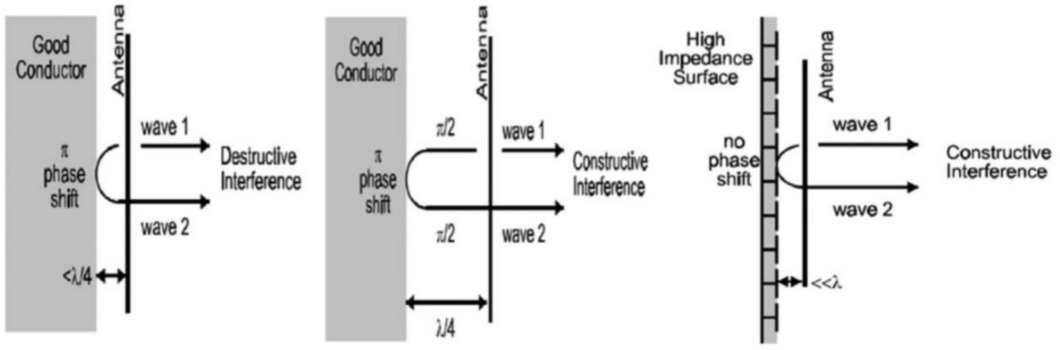

(a) (b) (c)

Figure 5.2: Antenna separated (a) closely and (b) further from the ground plane. (c)Antenna incorporated with AMC is in very close proximity with the ground layer [98].

Subsequently, the gain of the antenna decreases. In this case, the antenna might not properly match due to the strong field cancellation. The undesired effect of the PEC layer can be minimized by having the PEC layer at a minimum distance of *λ/4* from the radiating antenna as in Figure 5.2 (b). The corresponding distance considered the π phase shift of the reflected wave (from the PEC) that will constructively interfere with the source wave (from the antenna). Additionally, the impedance matching at the resonant frequency is also improved. Unfortunately, the drawback of the introduction of such distance increases the overall antenna dimensions.

Thus, the antenna structure is no longer low-profile, a characteristic most desirable in antenna designs especially in space limited conditions such as in microwave circuitry of portable devices. In contrast, PMC (or AMC in practical) generates reflected waves that are similar in the direction of the original current with the reflection coefficient of magnitude $|\Gamma|$ that equals to +1. As illustrated in Figure 5.2 (c), the reflected wave by AMC is in-phase with the source wave.

The additional reflected waves constructively interfere with the source wave. The combining effect from both reflected wave and source wave improves the radiation efficiency and gain of the antenna. Thus, a low-profile antenna can be realized without adding an unnecessary distance of $\lambda/4$ between the AMC ground plane and the antenna (as in the case of PEC ground layer).

5.3 CP CROSSED-DIPOLE ANTENNA WITH AMC SURFACE ON FR-4 SUBSTRATE

5.3.1 Antenna Design Configurations

A new way of designing a dual-band CP antenna by integrating a CP radiator with a finite AMC surface. The broadband operation was obtained in Figure 5.3. It consists of a compact crossed dipole above a 5 × 5 AMC surface. The antenna was optimized for GNSS frequency bands with low-profile broadband characteristics and excellent CP radiation.

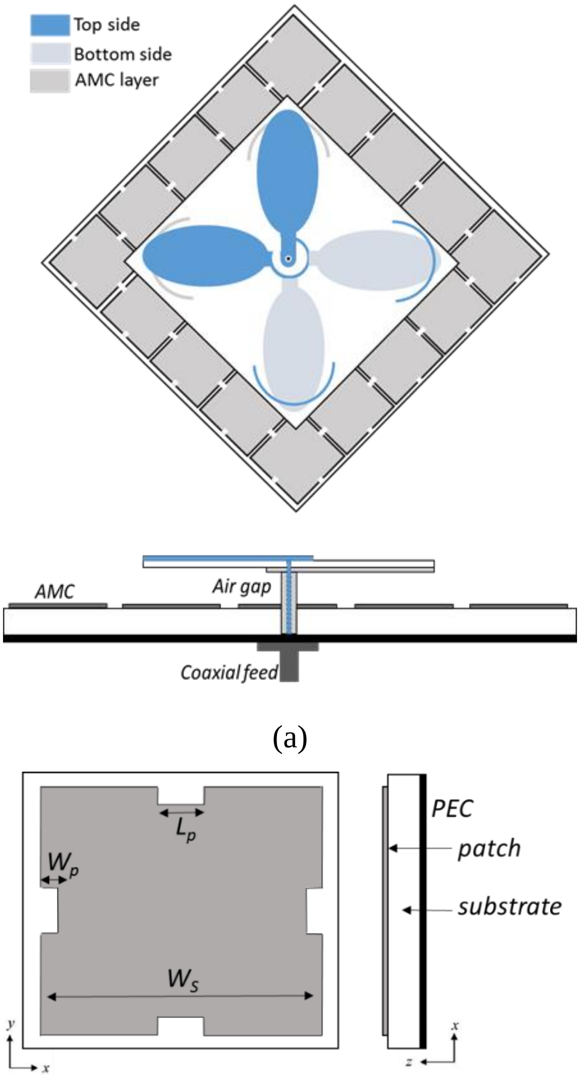

(a)

(b)

Figure 5.3: Geometry of the proposed antenna: (a) top and (b) cross-sectional view of the proposed antenna.

The proposed antenna is designed to meet the needs of multiple GNSS. The critical part is the feeding structure which is relatively new, and the dimensions should be optimized. The elliptical cross-dipole antenna is produced on both sides of the PCB board. The antenna was fed with a 50 Ω coaxial line. The outer conductor of the coaxial line was connected to the dipole arms on the bottom side of the substrate while the inner conductor of the coaxial line was extended through the substrate and connected to the dipole arms on the top side.

Figure 5.3 shows the geometry of the dual-band, crossed, asymmetric dipole antenna on the dual-band AMC surface. The crossed dipoles were suspended at a height from the top of the reflector. The primary radiator element, which is similar to the one presented in Chapter 4, was designed on both sides of PCB.

Figure 5.3 (b) shows the geometry of the unit cell of the AMC structure. A 5 × 5 metal patch array forming an AMC surface was backed as a reflector of the proposed antenna. The unit cell was printed on a 100 mm × 100 mm FR-4 substrate with a relative permittivity of 4.4, a loss tangent of 0.0023, and a thickness of 10 mm. There was no via. Four slits were symmetrically inserted into the square patch of the AMC unit cell. A sample of the fabricated antenna is shown in Figure 5.4. The AMC structure was optimized via adjusting the slit shape to have the resonances frequency.

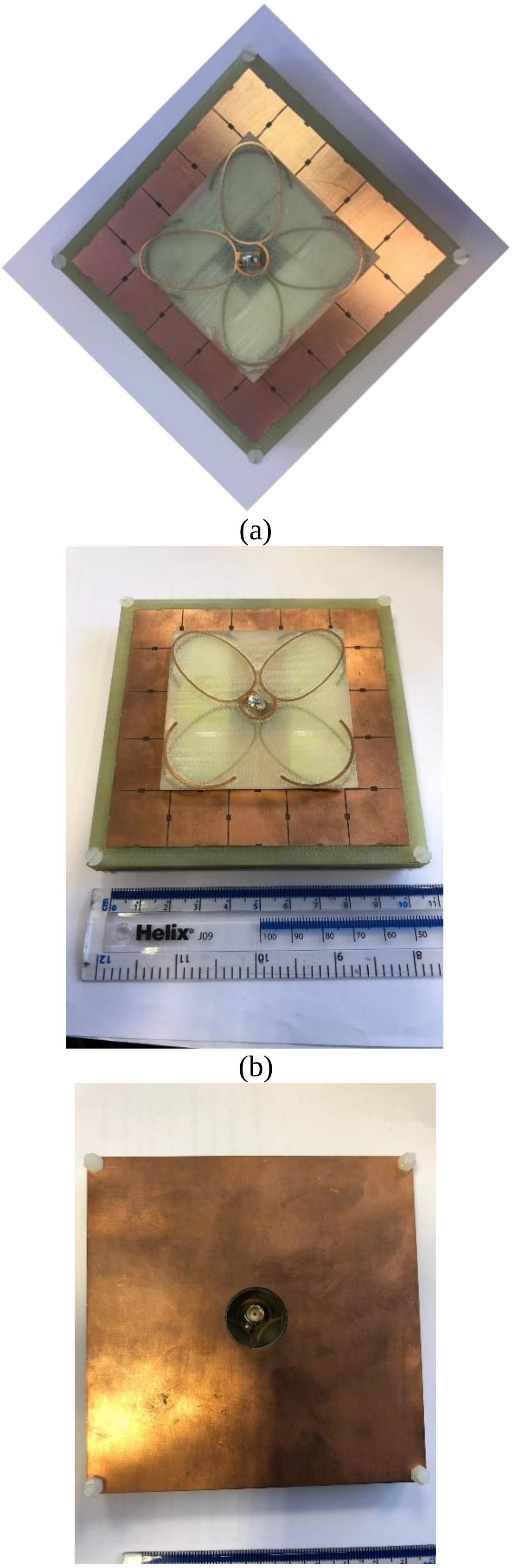

(a)

(b)

(c)

Figure 5.4: Photograph of the fabricated antenna (a),(b) front view and (c) back view.

5.3.2 Antenna Performances

The crossed asymmetric dipoles were first optimized in free space for GNSS frequency bands with good CP radiation and then incorporated with PEC and AMC reflectors to render a unidirectional radiation pattern. To achieve a unidirectional radiation pattern, good impedance matching, and good low-profile CP radiation at both operating bands, a crossed asymmetric dipole antenna was incorporated with the AMC surface. Interactions between the radiator and the reflector, such as the air gap and finite size of the AMC surface, were meticulously considered for the optimization.

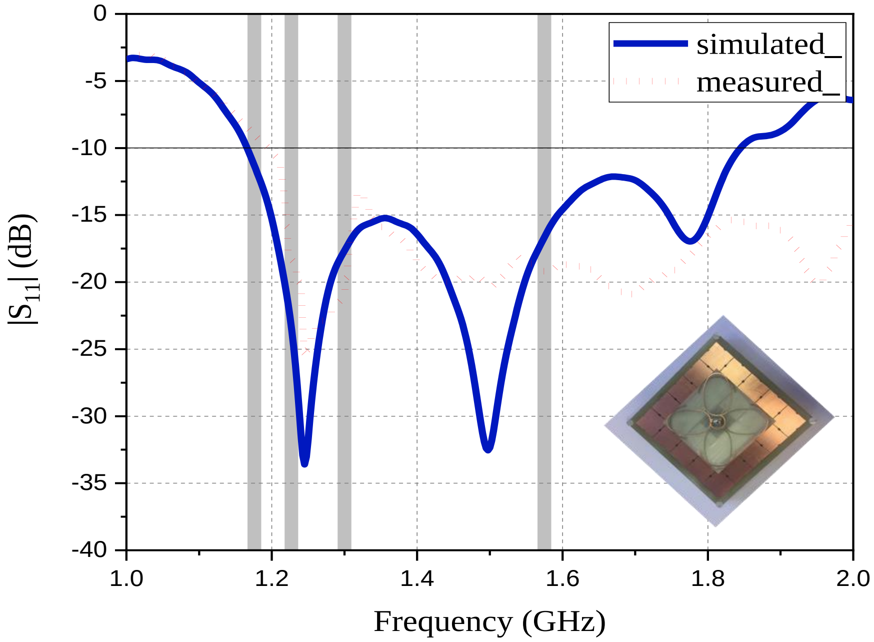

Figure 5.5: Measured and simulated results of the proposed antenna: |*S₁₁*|.

The overall size of the final design was 100 mm × 100 mm × 14 mm including the substrate thickness of the radiator. Since a 10 mm thick FR-4 sheet was unavailable, the AMC was fabricated by stacking several thin sheets and binding them together by using four plastic screws (not included in the simulations) to achieve the desired thickness.

The crossed asymmetric dipole on the dual-band AMC surface was fabricated and measured. A comparison of the simulated and measured $|S_{11}|$ and AR values is given in Figure 5.5 and Figure 5.6. The measured impedance bandwidths of 10 dB were 1.196 to 2.176 GHz, values that agree closely with the simulated bandwidths of 1.607 to 1.845 GHz.

The measured AR < 3-dB bandwidths were 1.148 to 1.761 GHz, while the simulated AR <3-dB bandwidths were 1.1803 to 1.795 GHz.

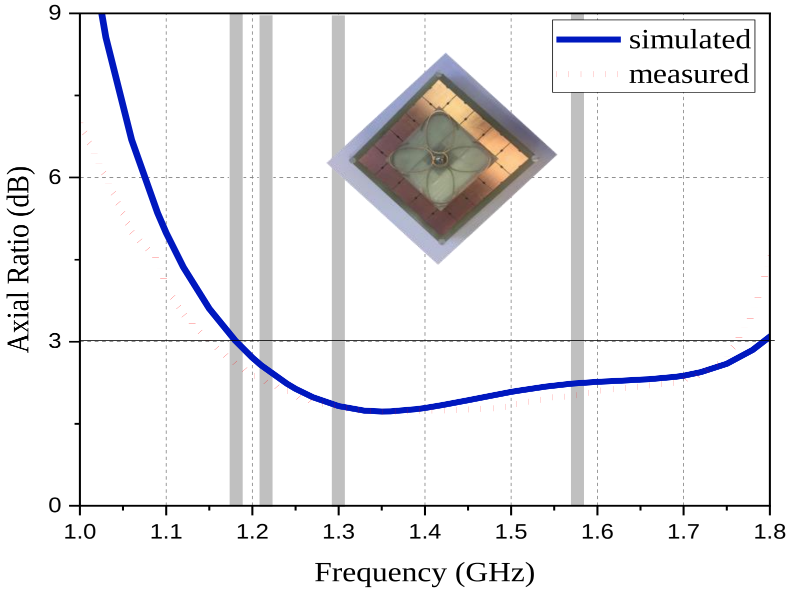

Figure 5.6: Measured and simulated results of the proposed antenna: AR.

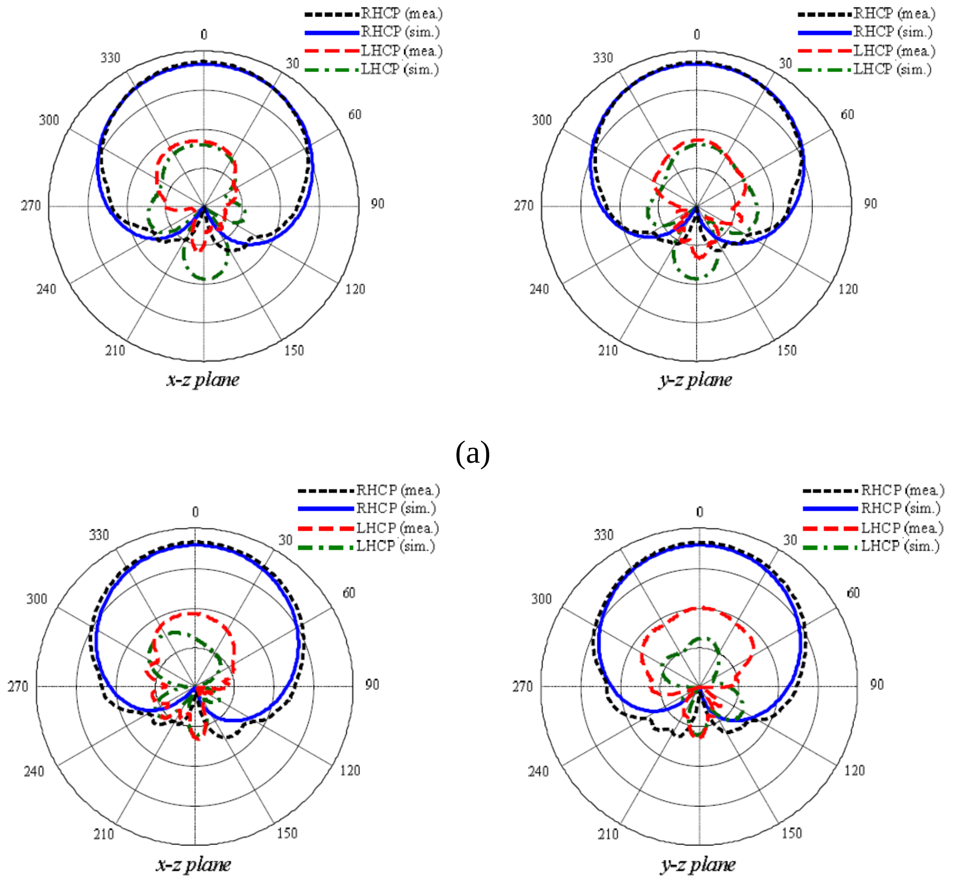

(a)

(b)

Figure 5.7: Measured and simulated results of the radiation pattern at (a) L1 and (b) radiation pattern at L2.

Figure 5.7 (a) and (b) shows the radiation patterns of the antenna at 1.575 GHz (L1) and 1.227 GHz (L2), respectively. The measurements agreed well with the CST simulation results and showed RHCP radiation, a wide CP radiation beamwidth, and asymmetric pattern in both the *xz* and *yz* planes. At 1.575 GHz, the measurements resulted in a gain of 5.9 dBic, a front-to-back ratio of 24 dB, and a 3-dB AR beamwidth of 200° and 199° in the *xz* and *yz* planes, respectively. At 1.227 GHz, the measurements resulted in a gain of 6 dBic, a front-to-back ratio of 24 dB, and a 3-dB AR beamwidth of 168° and 150° in the *xz* and *yz* planes, respectively. Additionally, the measured radiation efficiencies were about 90% and 87%, and the simulated values were 95% and 89%, at 1.227 GHz and 1.575 GHz, respectively.

5.4 CP CROSSED-DIPOLE ANTENNA WITH AMC SURFACE ON ROGERS RT6006 SUBSTRATE

5.4.1 Antenna Design Configurations

Figure 5.8 shows the geometry of the proposed antenna which comprised of two printed dipoles as a primary radiator which is similar to the one presented in Chapter 4, was designed on both sides of PCB, a coaxial line, and an AMC surface. The printed dipoles were suspended at height H above the AMC surface. The AMC was composed of 5 × 5 square metal patch structures that were periodically printed on the conductor-backed substrate.

Figure 5.8 (b) shows the geometry of the unit cell of the AMC structure. A 5 × 5 metal patch array forming an AMC surface was backed as a reflector of the proposed antenna. The unit cell was printed on a 100 × 100 mm^2 Rogers RT 6006 substrate with a relative permittivity of 4.4, a loss tangent of 0.0023, and a thickness of 12.7 mm as shown in appendices section. There was no via. Four slits were symmetrically inserted into the square patch of the AMC unit cell. A sample of the fabricated antenna is shown in Figure 5.9.

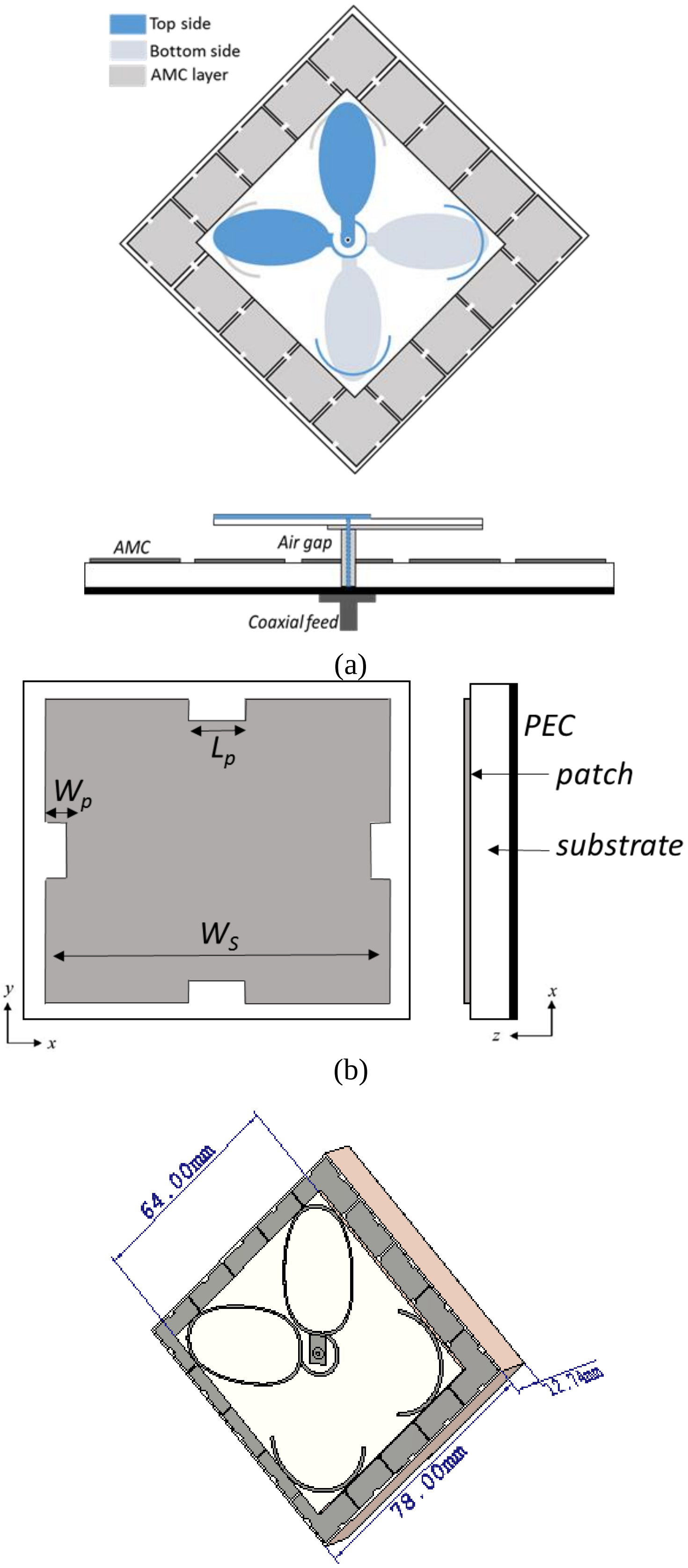

(a)

(b)

(c)

Figure 5.8: Geometry of the proposed antenna: (a) top and (b) cross-sectional view of the proposed antenna (c) perspective view.

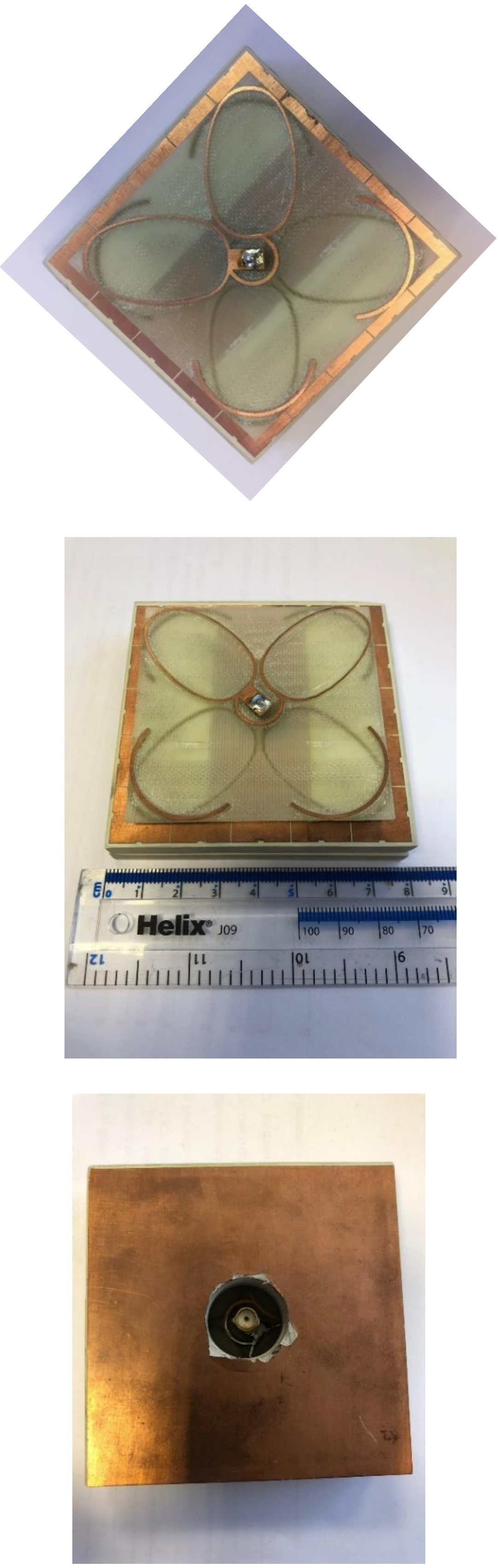

Figure 5.9: Photographs of the fabricated antenna.

The AMC structure was optimized via adjusting the slit shape to have the resonances frequency. The AMC substrate was made of an RT6006 material with a relative permittivity of 10.2 and a loss tangent of 0.0023. The characteristic impedance of the coaxial line was 50 Ω, and the line passed through the center of the AMC reflector to feed the radiator. The antenna was optimized via CST Simulation Software.

5.4.2 Antenna Performances

This design using a 5 × 5 cell AMC configuration with H = 12.7 mm was fabricated and measured. The printed dipoles were fabricated on both side of FR-4, and AMC reflector was fabricated on RT6006. Because a 12.7 mm thick RT6006 sheet was unavailable, the AMC was fabricated by stacking two sheets and binding them together by tape to achieve the desired thickness. The antenna was measured in an anechoic chamber using a network analyzer.

The comparison of the simulated and measured reflection coefficients of the antenna is shown in Figure 5.10. The $|S_{11}| < -10$ dB measured bandwidths of the lower and upper bands were merged, and the result ranged from 1.153 to 2.36 GHz. The simulated bandwidths were 1.154 to 1.929 GHz. The slight difference between the measurement and the simulation could be attributed to the effects of the binding process.

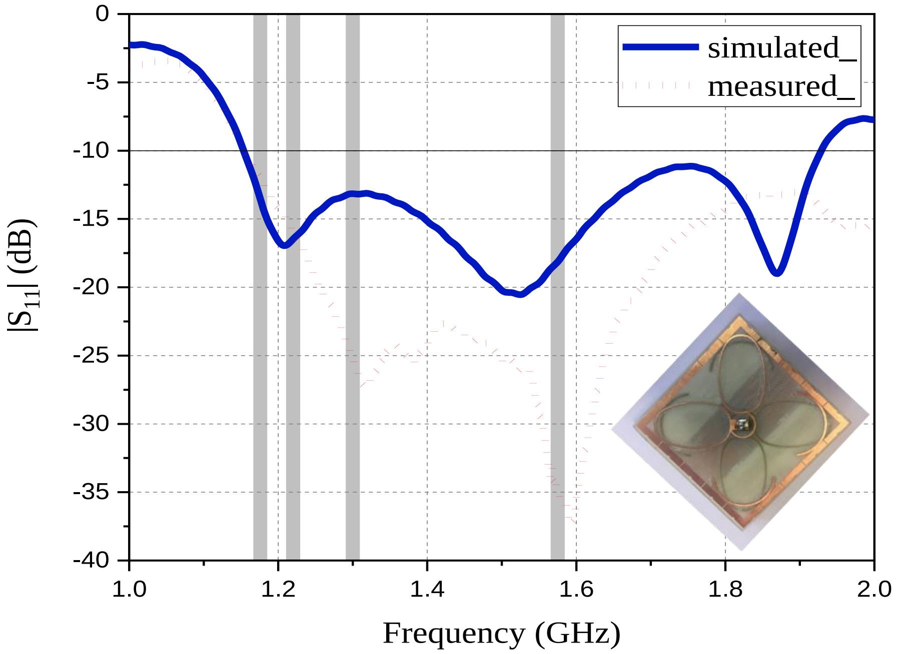

Figure 5.10: Measured and simulated results of the proposed antenna: $|S_{11}|$.

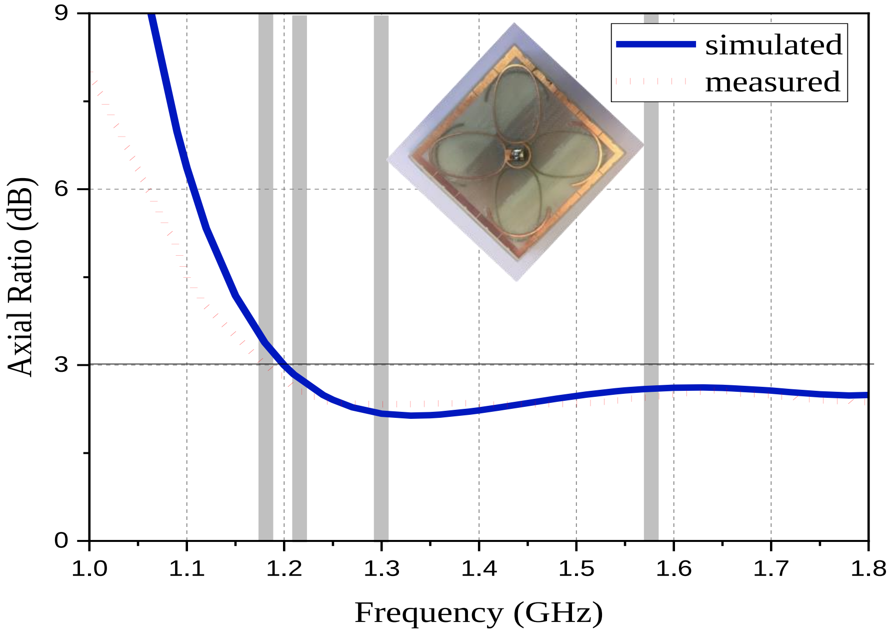

Figure 5.11: Measured and simulated results of the proposed antenna: AR.

Figure 5.11 shows the measured and simulated AR bandwidth values of the antennas, which also yielded a good agreement between the two. The measured 3-dB AR bandwidths were 1.170 – 1.970 GHz. The simulated 3-dB AR bandwidths were 1.199 – 1.9 GHz. Figure 5.12 (a-d) shows the radiation patterns of the crossed dipole on the AMC surface at L5 (1.176 GHz), L2 (1.277 GHz), E6 (1.3 GHz) and L1 (1.575 GHz), respectively and which shows good agreement between the measurements and the simulations.

The radiation was RHCP and symmetric in both the xz and the yz planes. At 1.176 GHz, the measurements yielded a gain of 7.55 dBic, a front-to-back ratio of 24 dB, half-power beamwidths (HPBWs) of 100° and 102° in the xz and yz planes, respectively, and 3-dB AR beamwidths of 161° and 120° in the xz and yz planes, respectively. At 1.227 GHz, the measurements yielded a gain of 7.7 dBic, a front-to-back ratio of 26 dB, HPBWs of 100° and 102° in the xz and yz planes, respectively, and 3-dB AR beamwidths of 112° and 134° in the xz and yz planes, respectively.

At 1.3 GHz, the measurements yielded a gain of 8.1 dBic, a front-to-back ratio of 25 dB, HPBWs of 105° and 103° in the xz and yz planes, respectively, and 3-dB AR beamwidths of 124° and 145° in the xz and yz planes, respectively. At 1.575 GHz, the measurements yielded a gain of 7.94 dBic, a front-to-back ratio of 27 dB, HPBWs of 90° and 96° in the xz and yz planes, respectively, and 3-dB AR beamwidths of 168° and 135° in the xz and yz planes, respectively. Also, the measurements resulted in high radiation efficiencies, which were 87%, 88%, 90%, and 91% at 1.176 GHz, 1.227 GHz, 1.3 GHz, and 1.575 GHz, respectively.

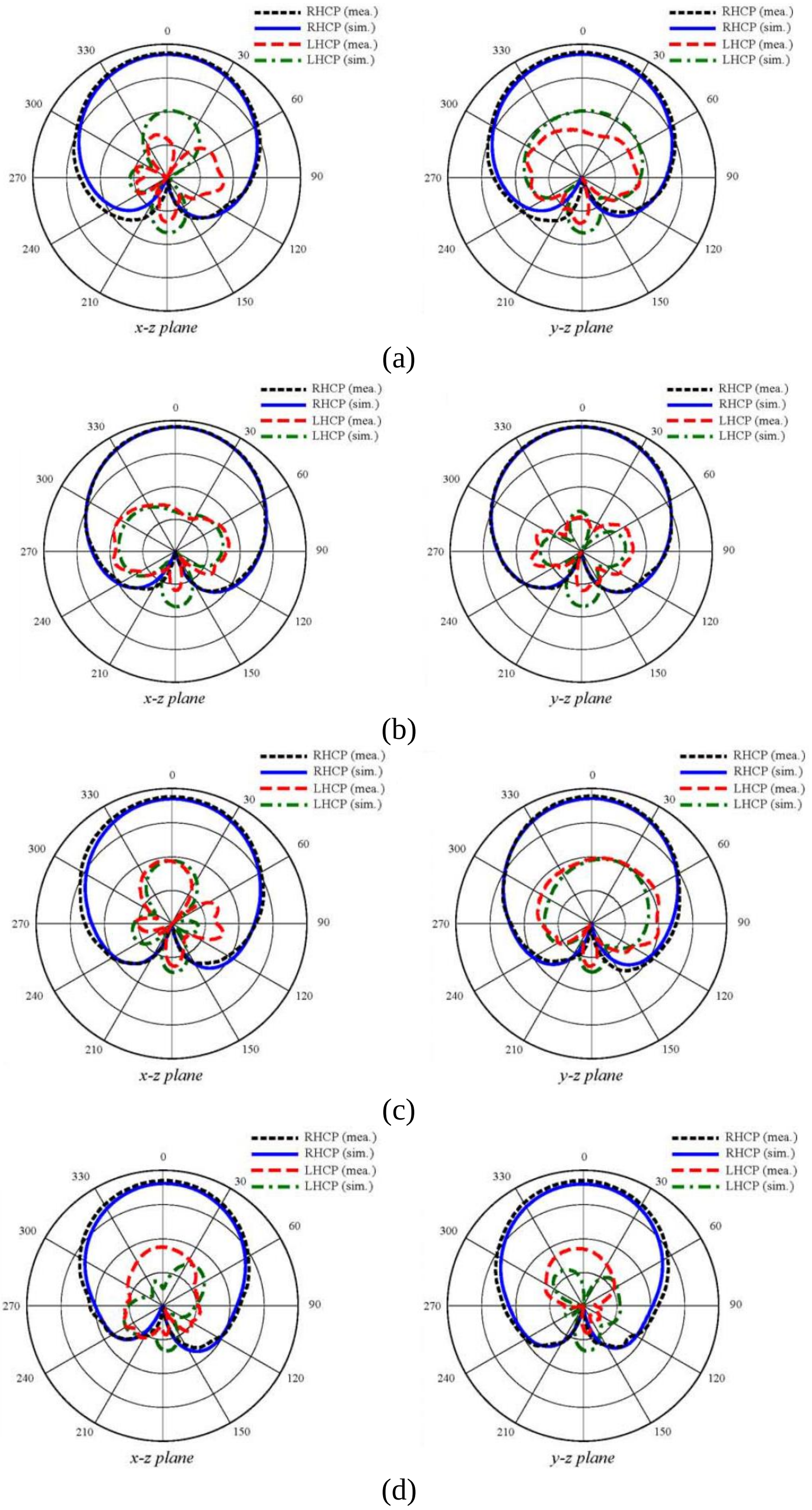

Figure 5.12: Measured and simulated radiation pattern results of the proposed antenna at (a) L5; (b) L2; (c) E6; (d) L1.

5.5 SUMMARY

The size of the AMC surface was a crucial factor in defining the original and additional operating CP bands of the antenna. The measured results of the proposed design with a size of 100 × 100 × 10 mm^3 FR-4 material AMC and yielded an impedance bandwidth of 1.196 to 2.176 GHz for the $|S_{11}|$<–10dB and 3-dB AR bandwidths of 1.148 to 1.761 GHz. Meanwhile, the measured results of the proposed design with a size of 100 × 100 × 12.7 mm^3 Rogers RT6006 material AMC and yielded an impedance bandwidth of 1.153 to 2.36 GHz for the $|S_{11}|$<–10dB and 3-dB AR bandwidths of 1.170 – 1.970 GHz. Additionally, the proposed antenna exhibited RHCP and high radiation efficiency (> 90%) in both bands. With a low profile, broadband characteristics, and high radiation efficiency, the proposed antenna could be widely applied to dual-band GNSS applications as well as in many other kinds of satellite communications.

The interesting features of the AMC-based crossed dipole antennas are not only their ability to achieve high efficiency with a low profile but also to generate additional resonances and the corresponding additional CP radiation features. These were utilized to add other operating bands or to broaden the antenna bandwidth. However, further investigations of these phenomena have not been rigorously pursued. The challenge is to develop a theoretical model that can be used to predict the extra resonances exist in all of the antennas. Consequently, future work should consider the suppression or utilization of these resonances depending on whether or not they would be beneficial to the antenna in selected applications.

In order to evaluate the achievements of the proposed antenna with respect to available designs, the proposed antenna is compared with recently published designs as tabulated in Table 5.1.

Table 5.1: Comparison with Proposed Antenna without AMC

Ref.	Size (mm^3)	$\lvert S_{11}\rvert$ <-10 dB BW (GHz)	Axial Ratio BW (GHz)	Antenna Type
Proposed Antenna without AMC	**90 × 90 × 15.5**	**1.06 to 1.671 (L1, L2, L5, E6)**	**1.093 to 1.257 (L5, L2) 1.542 to 1.666 (E6)**	**Crossed-dipole antenna**
Proposed Antenna with AMC surface on FR-4 substrate	**100× 100 × 10**	**1.196 to 2.176 (L1, L2, L5, E6)**	**1.148 to 1.761 (L1, L2, L5, E6)**	**Crossed-dipole antenna**
Proposed Antenna with AMC surface on Rogers RT6006 substrate	**100 × 100 × 12.7**	**1.153 to 2.36 (L1, L2, L5, E6)**	**1.170 to 1.970 (L1, L2, L5, E6)**	**Crossed-dipole antenna**

CHAPTER 6:

DESIGN OF ANTI-JAMMING ANTENNA FOR THE GNSS RECEIVER

6.1 INTRODUCTION

Global Navigation Satellite System (GNSS) receivers are highly susceptible to radio frequency interference (RFI) due to the weak signals of the satellites. The interference sources could be intentional, such as high and medium-powered jammers with various signal modulations, or unintentional, such as in-band signals of civilian and military terrestrial navigation systems and out-of-band harmonics of terrestrial digital video broadcasting [124]. Due to the vast number of applications relying on GNSS, interference mitigation is of high importance in military and increasingly in civilian sectors.

6.2 OVERVIEW OF INTERFERENCE THREAT

Radio frequency interference on GNSS frequencies can originate from a variety of sources, including aircraft avionics and ground-based sources such as radar and aeronautical emitters [125]–[127]. In some cases, navigation signals share spectrum with other signals [125], [127]–[129]. In a more difficult case, the interference could come from hostile jamming. There is a range of interference and jamming waveforms including continuous wave (CW), pulsed CW, narrowband and broadband Gaussian noise, and phase-shift keyed pseudo-noise. To understand the detrimental effects of interference, it is necessary to appreciate the weak signal strength of GNSS satellite signals.

Spoofing and meaconing are structural wideband intentional interference which misdirect target GNSS receivers into generating fictitious position and/or timing solutions [130], [131]. Meaconing is a replayed version of a recorded genuine GNSS signal whereas spoofing is a fake signal that is designed to mimic the authentic signal's structure. Under a spoofing or meaconing attack, a receiver provides position and timing solutions with good signal quality measures. However, the solutions do not represent the actual location or time of the victim user. Due to the widespread use of civilian GNSS dependent systems, motivation has increased to spoof GNSS signals for scores of illegal activities. Therefore, spoofing is becoming a more serious type of threat for future applications and this necessitates proper countermeasures [132], [133]. Many research groups have been involved in the vulnerability analysis of GNSS to spoofing attack (e.g., [130], [131], and [133]–[135]).

State-of-the-art interference suppression systems for GNSS receivers utilize a multi element antenna array with an adaptable reception pattern. Adaptive arrays allow greater performance over a single element antenna by their ability to provide beamforming/null steering in specific directions. This gives the system spatial degrees of freedom with which to separate the desired and undesired signals.

6.3 CIRCULAR POLARIZED CROSSED-DIPOLE ANTENNA

6.3.1 Antenna Element Design

Reducing an antenna array's size to fit into conventional single antenna receivers has been a major focus of the research in this area in the past few years [136]. In order to have a compact array, the previous design has been optimized to reduce the electrical the size of antenna elements and extend the impedance and CP bandwidths.

In addition to the existing inductive loading approach, a combination of elliptical and circle loop radiator for the dipole arms to develop a small size broadband CP antenna has been proposed. The electrical size of the complete antenna can be further reduced to $0.22\,\lambda_0 \times 0.22\,\lambda_0 \times 0.001\,\lambda_0$. Moreover, the proposed antenna enables a broadband operation from 1.03 to 2.58 GHz. To the authors' knowledge, we have probably reported the smallest electrical size for CP crossed dipoles with a similar frequency coverage and a relatively wide bandwidth (e.g., FBW > 30%).

The 3D disassembled view of the proposed crossed dipole antenna with parasitic elements is depicted in Figure 6.1. There are two layers of PCBs employed in this design. The substrate materials for both circuit boards are the low-cost FR4 with a relative permittivity of 4.3 and a thickness of 1.6 mm. The crossed dipole antenna is located at the bottom layer and printed on both sides of the PCB. It is fed by using a typical 50 Ω coaxial cable that is perpendicular to the board. In addition, a parasitic element is printed on the top layer substrate and stacked over the crossed dipole without a gap. It couples to the crossed dipole through the substrate without any electrical connections to the antenna.

To have a better illustration of the design, the detailed geometry of the proposed antenna is shown in Figure 6.2. There are several notable features in this design. The main aim of using such a “combination elliptical and circle shaped loop” structure is to improve/broaden the impedance bandwidth as well as the axial ratio (AR) bandwidth of the crossed dipole. It can also reduce the resonant frequency of the antenna, or in other words, miniaturize the physical dimension of the antenna.

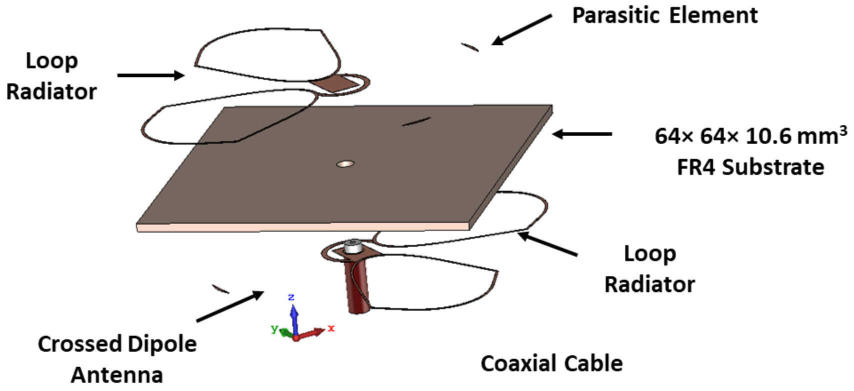

Figure 6.1: 3D disassembled view of the proposed crossed dipole antenna with parasitic elements.

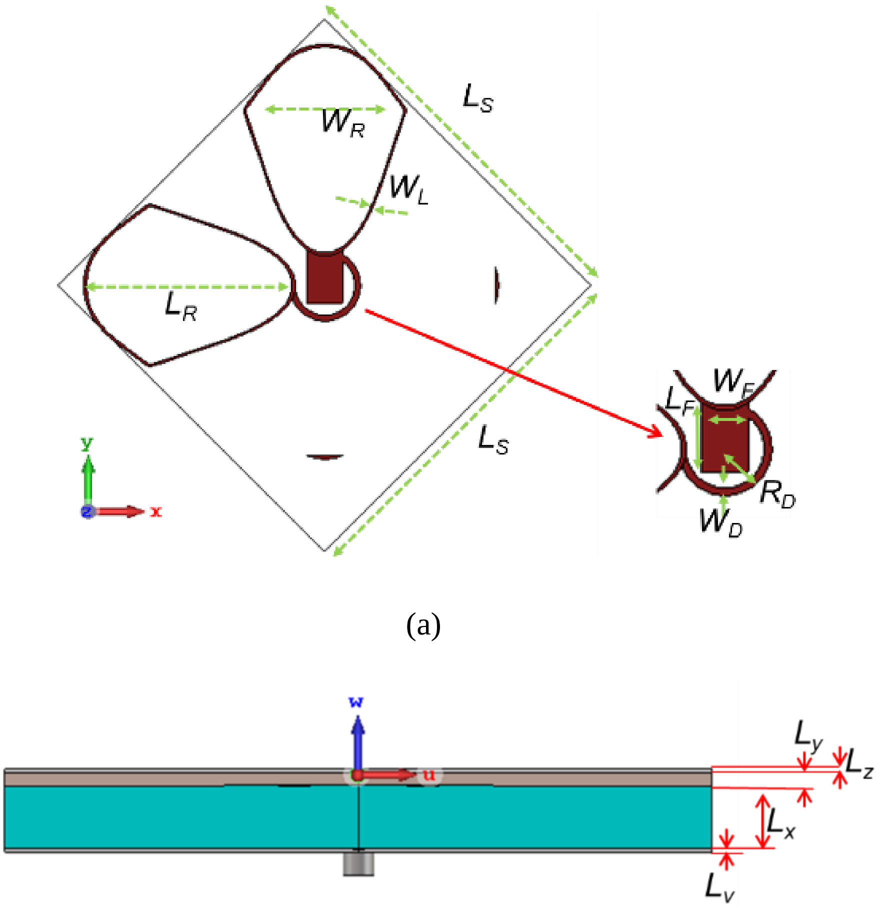

(a)

(b)

Figure 6.2: Detailed geometry of the proposed antenna (a) Crossed dipole antenna. (b) Side view of the antenna.

The antenna was built and modelled using the CST software. After software simulation and optimization, the final antenna parameters (as given in Figure 6.2) are listed in Table 6.1. The lowest resonant frequency of the antenna was found to be about 1.03 GHz. According to the antenna dimension in Table 6.1, the electrical size of this antenna is only around 0.22 λ_0 × 0.22 λ_0.

Table 6.1: Optimized Parameters of The Proposed Antenna

Parameter	**Value (unit: mm)**	**Parameter**	**Value (unit: mm)**
W_R	28	W_D	1.5
L_R	35	R_D	6
W_L	0.8	L_y	1.6
L_S	64	L_v	0.5
W_F	6	L_z	0.5
L_F	8.4	L_x	8.0

To have a better understanding of this novel antenna design, the evolution of the antenna design is shown in Figure 6.3. It can be seen that the starting point of this design is atypical CP crossed dipole where the arms of the dipole are strip lines with a width of 6 mm and a length of 34 mm. The feeding structure is identical to that of the proposed antenna as given in Figure 6.3. in this scenario, the total length of the dipole is about 84 mm after taking the feeding structure into account. If the antenna is considered as a typical half-wavelength dipole, the resonant frequency of this antenna can be estimated at around 1.7 GHz [137].

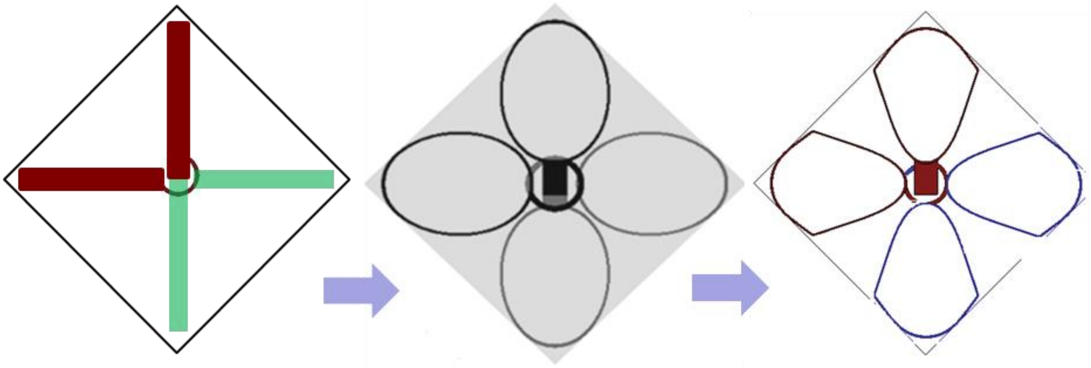

Figure 6.3: Evolution of the antenna design: a conventional crossed dipole is converted to an egg-shaped loop radiator; finally, the proposed antenna is designed with combination elliptical and circle shaped loop radiator.

Next, to broaden the bandwidth of the crossed dipole, the arms are changed to elliptical, egg-shaped structures. The loop structure also reduced the resonant frequency of the antenna. Finally, the antenna optimized by changing a few points of the radiator to get the combination structure.

It has been demonstrated that by modifying the crossed dipole from a conventional reference structure to the proposed novel structure, the lowest resonant frequency has been reduced from 1.3 to 1.03 GHz, while the impedance and CP bandwidths have been improved from 37.5% and 12.5% to 89.5% and 87% respectively. The electrical size of the proposed antenna is only around 0.22 $\lambda_0 \times 0.22$ λ_0. Figure 6.3 shows the evolution of the antenna design from a conventional crossed dipole to an egg-shaped crossed dipole with radiator and finally the proposed antenna with combination of elliptical and circle loop of radiator.

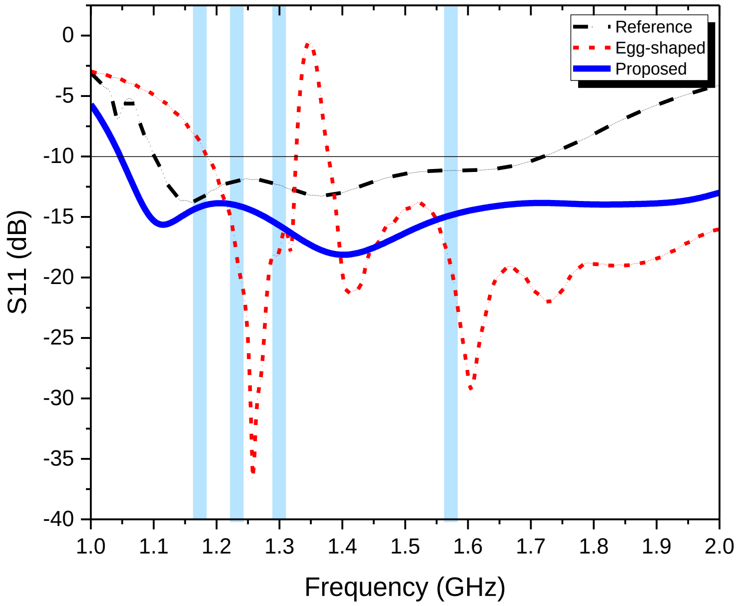

Figure 6.4: Simulated S_{11} of the reference crossed dipole antenna, the egg-shaped crossed dipole using loop radiators and the proposed antenna.

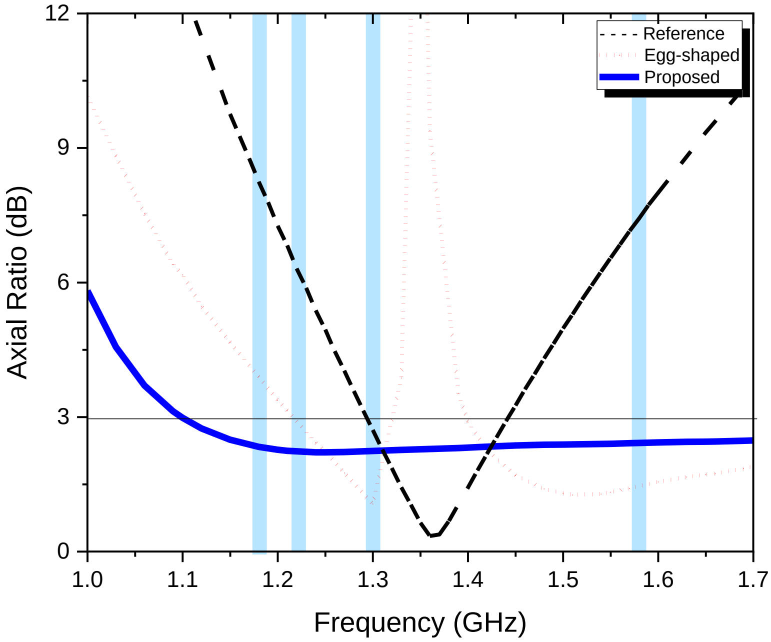

Figure 6.5: Simulated axial ratio (AR) of the reference crossed dipole antenna, the egg-shaped crossed dipole using loop radiators and the proposed antenna.

6.3.2 Antenna Element Performance

In order to gain a better understanding of the operation mechanism of the proposed antenna, the simulated current distributions at three different frequencies are shown in Figure 6.6 for phase = 0° and 90° respectively.

It is noted that, when the phase = 0°, the currents are mainly distributed on the vertical arms of the crossed dipole as well as the vertical part of the parasitic element. While the current distribution on the horizontal dipole and horizontal part of the parasitic element becomes stronger when the phase = 90°. This means that the vacant ring feeding structure has delayed the phase by 90° between the dipole pair. A CP radiation field could, therefore, be generated by using this single feed antenna.

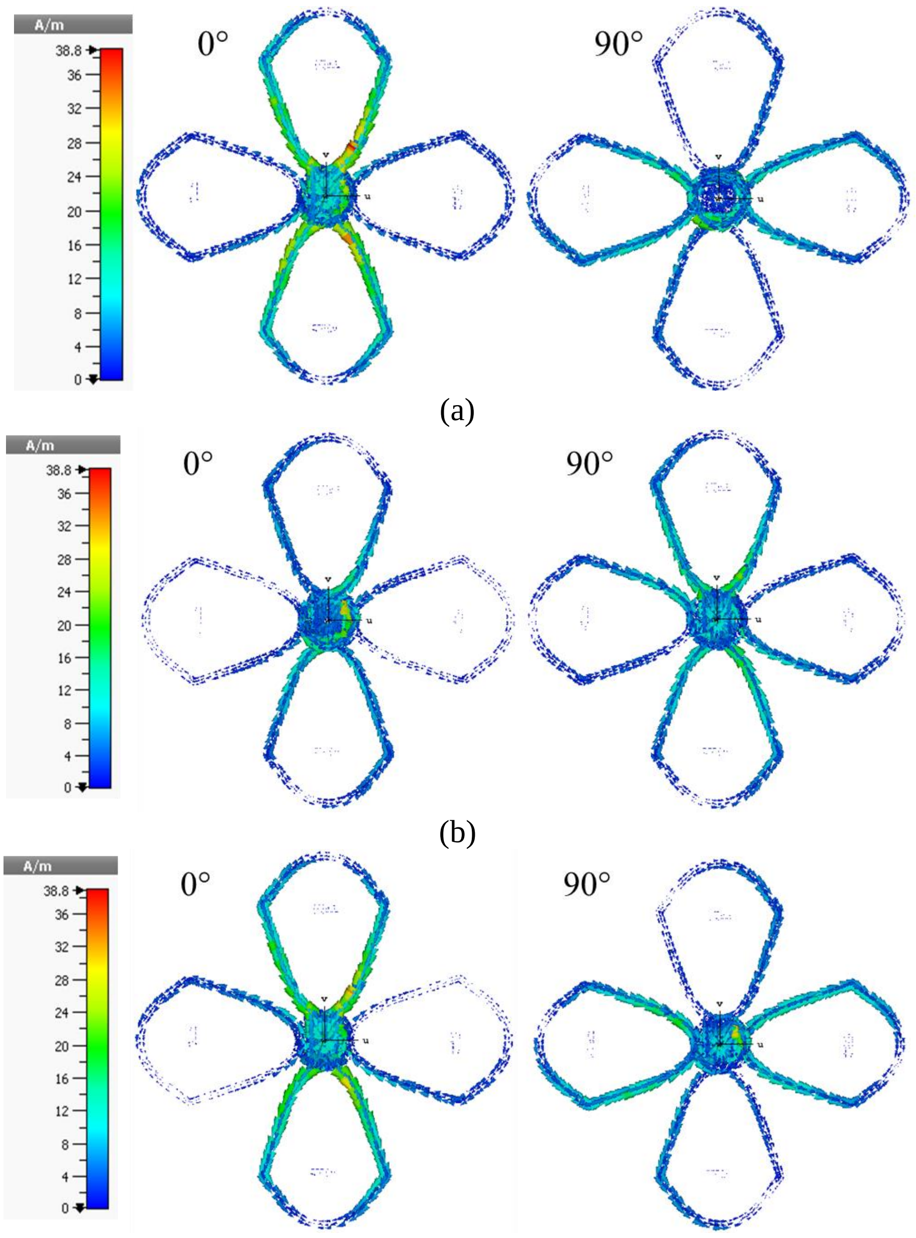

(a)

(b)

(c)

Figure 6.6: Simulated surface current distribution of the proposed antenna with parasitic element at (a) 1.15 GHz, (b) 1.21 GHz and (c) 1.57 GHz.

At the resonant frequency of 1.15 GHz, the current distribution on the parasitic element is stronger than that of higher frequencies (e.g., 1.21 GHz), which demonstrates that the parasitic element can be driven by the crossed dipole at a lower frequency band using the coupling between them.

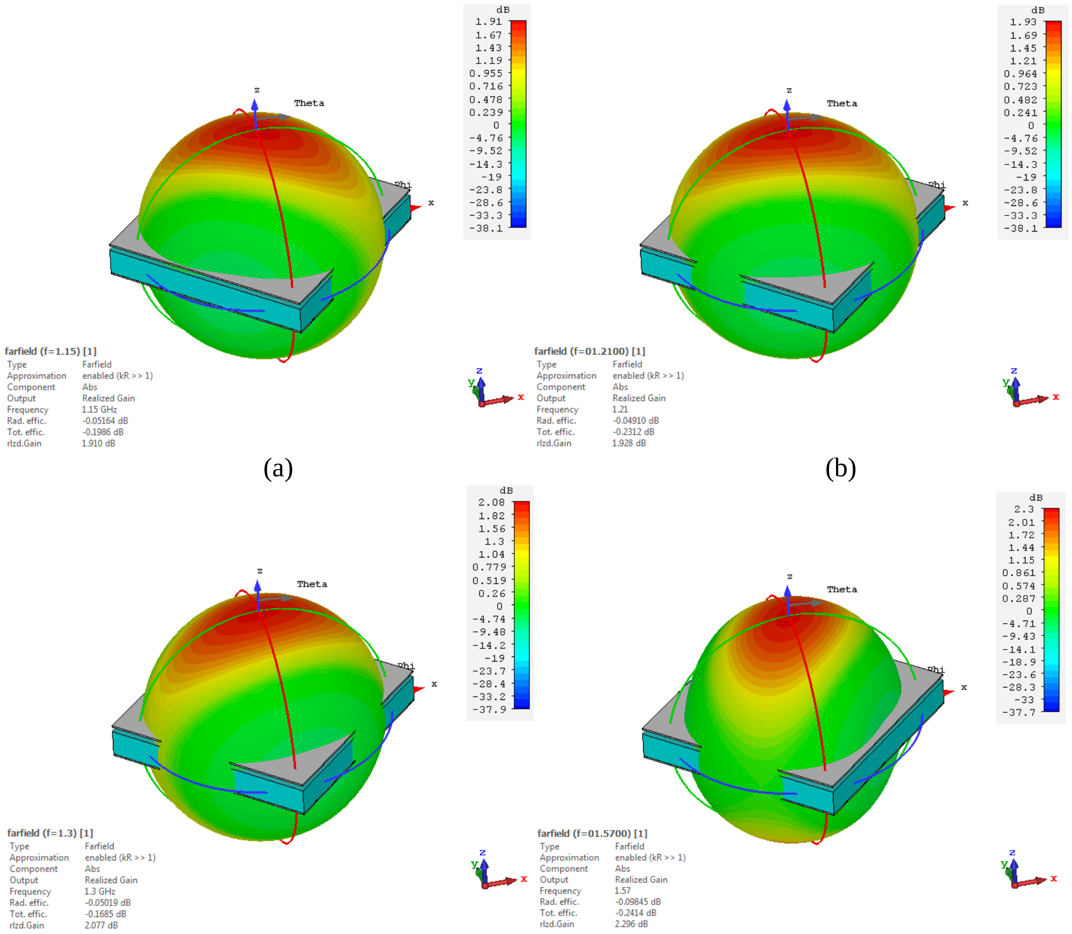

farfield (f=1.15) [1]

Type	Farfield
Approximation	enabled (kR >> 1)
Component	Abs
Output	Realized Gain
Frequency	1.15 GHz
Rad. effic.	-0.05164 dB
Tot. effic.	-0.1986 dB
rlzd.Gain	1.910 dB

(a)

farfield (f=01.2100) [1]

Type	Farfield
Approximation	enabled (kR >> 1)
Component	Abs
Output	Realized Gain
Frequency	1.21
Rad. effic.	-0.04910 dB
Tot. effic.	-0.2312 dB
rlzd.Gain	1.928 dB

(b)

farfield (f=1.3) [1]

Type	Farfield
Approximation	enabled (kR >> 1)
Component	Abs
Output	Realized Gain
Frequency	1.3 GHz
Rad. effic.	-0.05019 dB
Tot. effic.	-0.1685 dB
rlzd.Gain	2.077 dB

(c)

farfield (f=01.5700) [1]

Type	Farfield
Approximation	enabled (kR >> 1)
Component	Abs
Output	Realized Gain
Frequency	1.57
Rad. effic.	-0.09845 dB
Tot. effic.	-0.2414 dB
rlzd.Gain	2.296 dB

(d)

Figure 6.7: Simulated 3D radiation pattern of the proposed antenna with parasitic element at (a) 1.15 GHz. (b) 1.21 GHz. (c) 1.3 GHz. (d) 1.57 GHz.

The simulated 3D radiation pattern at 1.15 GHz is given in Figure 6.7 (a). It can be seen that the proposed antenna is almost of the omnidirectional radiation pattern with a realized gain of around 1.91 dBi. From Figure 6.7 (b), the peak currents at 1.57 GHz are located around the top edge of the egg-loop structures, which shows that the antenna works at the half-wavelength dipole mode. This feature can also be verified from the 3D radiation pattern of the antenna (see Figure 6.7 (c)), where the proposed antenna has a symmetrical bi-directional radiation pattern with a realized gain of 2.1 dBi.

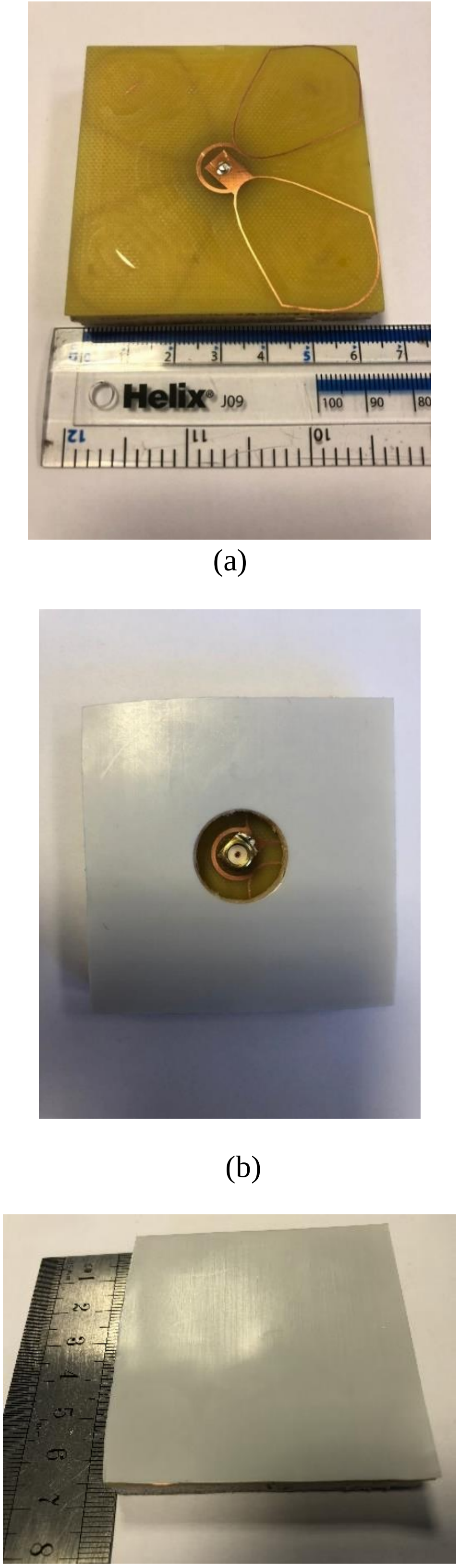

(a)

(b)

(c)

Figure 6.8: The fabricated antenna examples. (a) The crossed dipole at the top of PCB, (b) the bottom of the antenna, and (c) overall antenna with a radome.

Having optimized the complete antenna, the prototype antenna example was fabricated using the parameters as given in Table 6.1. The picture of the fabricated antenna example is shown in Figure 6.8. The overall size of the complete antenna was about 64 × 64 × 10.6 mm^3. Figure 6.9 depicts the measured and simulated S_{11} of the proposed antenna in an anechoic chamber. It is noted that the simulated antenna performance was better than the measured one over the frequency band. This was because the gap between the two PCBs cannot exactly be 0 mm in reality. Therefore, the coupling effect was reduced for the fabricated antenna prototype.

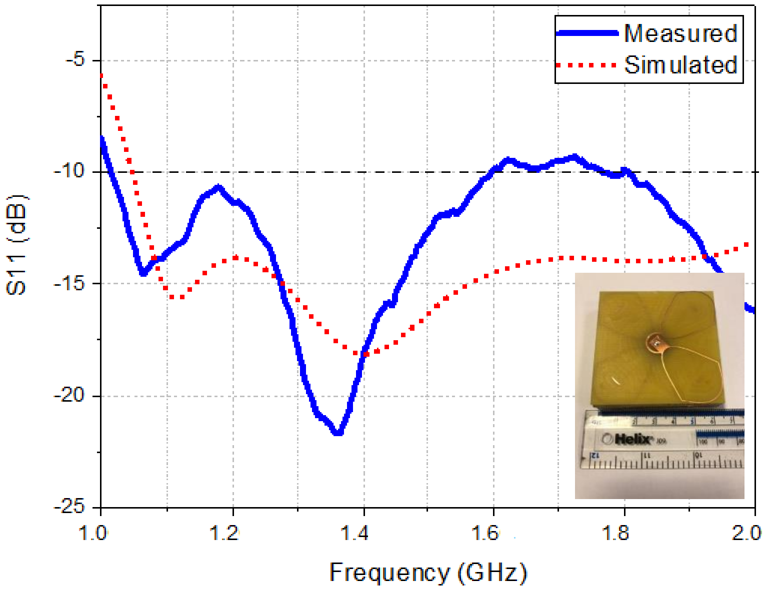

Figure 6.9: Simulated and measured S_{11} of the proposed antenna.

The measured impedance bandwidth was therefore counted from 1.016 to 1.598 GHz (FBW = 85.8%) for S_{11} < -10 dB. The simulated and measured axial ratios of the proposed antenna are given in Figure 6.10. A reasonable agreement is obtained between the simulated and measured ones. The measured AR was smaller than 3-dB for the bands between 1.048 – 1.142 GHz, 1.150 – 1.231 GHz and 1.282 – 1.572 GHz (FBW = 56.3%).

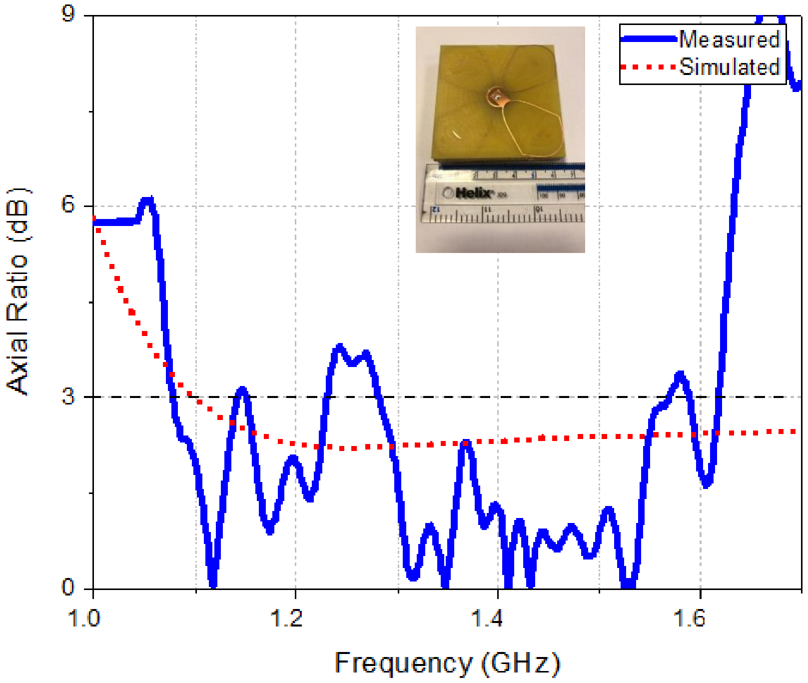

Figure 6.10: Simulated and measured axial ratio of the proposed antenna.

Figure 6.11 shows the simulated and measured radiation patterns over the *XOZ* and *YOZ* planes at 1.15 GHz, 1.3 GHz and 1.575 GHz. The proposed broadband CP antenna generated a bidirectional radiation field, i.e., the broadside radiation field was RHCP, while the backside radiation field was LHCP. The HPBW were found to be about 207° at 1.15 GHz, 113° at 1.3 GHz and 71° at 1.575 GHz respectively (for RHCP).

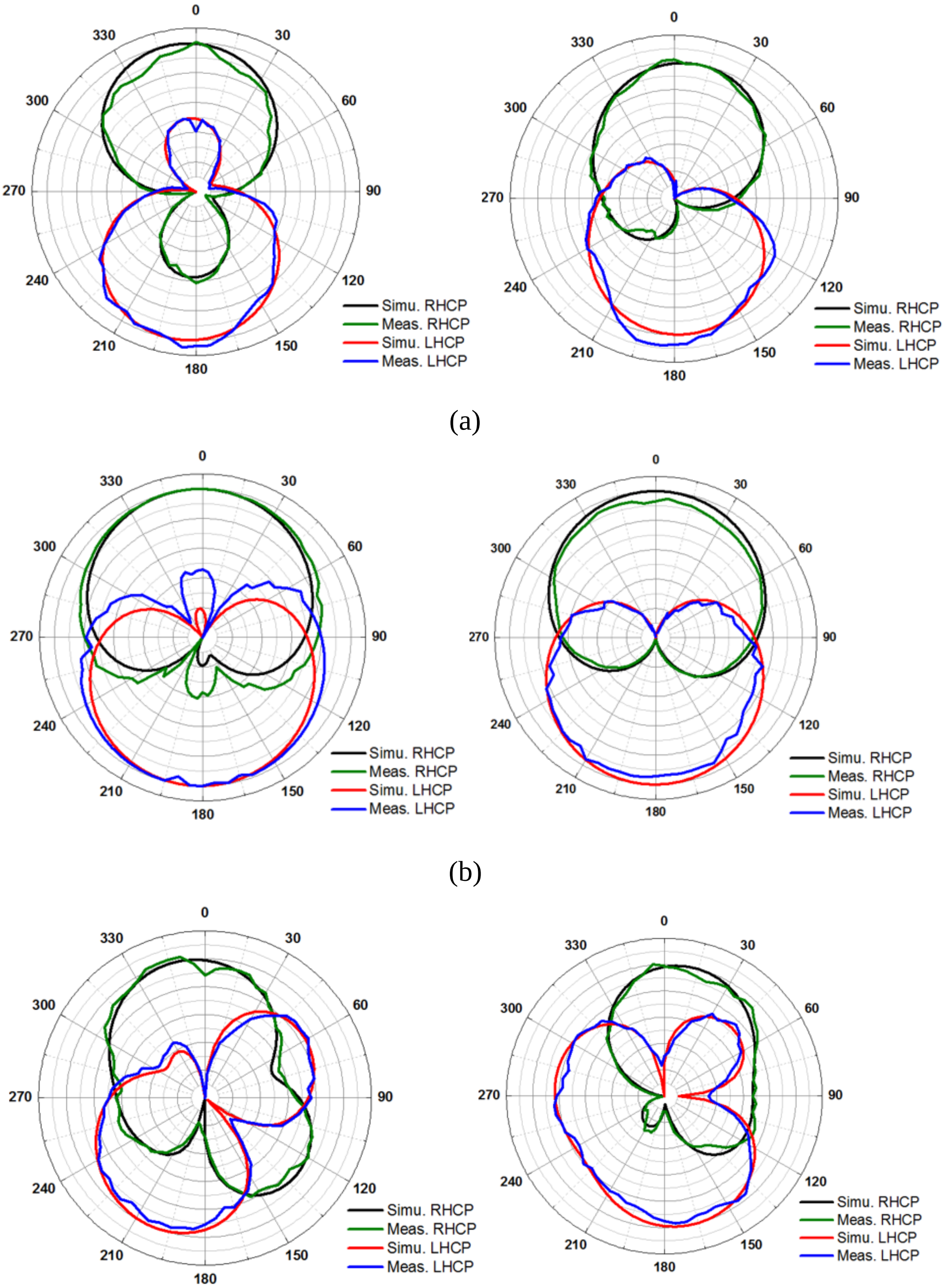

(a)

(b)

(c)

Figure 6.11: Simulated and measured radiation pattern over *XOZ*-plane (left) and *YOZ*-plane (right) at three different frequencies. (a) 1.15 GHz. (b) 1.3 GHz. (c) 1.575 GHz.

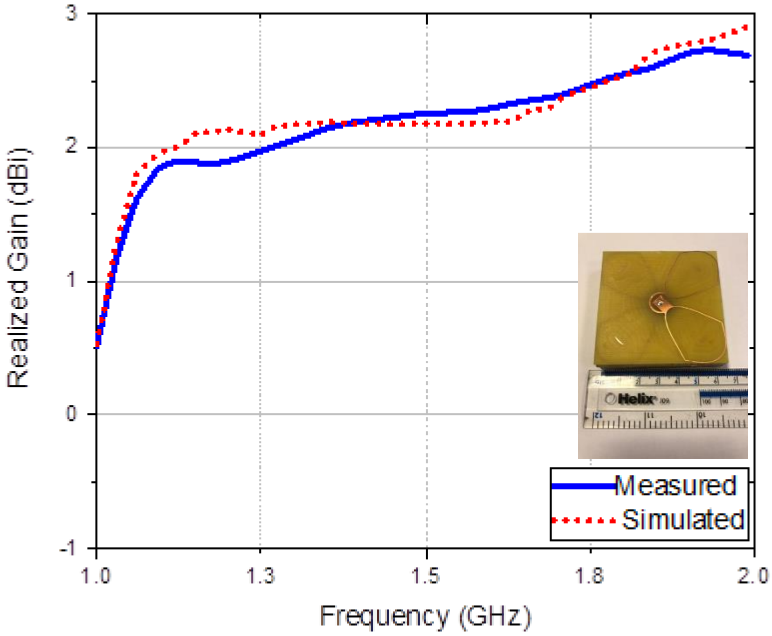

Figure 6.12: Simulated and measured axial ratio of the proposed antenna.

The simulated and measured realized gains of the proposed antenna are shown in Figure 6.12. It can be seen that the gain is around 1 to 3 dBi over the frequency band of interest. The total efficiency for all frequency band was greater than 80%.

6.4 ARRAY DESIGN CONFIGURATION

In this section onwards, a new method is proposed to extract the optimal complex weights for suppression of the jamming signals in a GNSS antenna array. As depicted in Figure 6.13, the controlled reception pattern antennas (CRPAs), adaptive antennas, null-steering antennas or beamforming antennas that specialized antenna that helps protect GNSS receivers from interference and jamming.

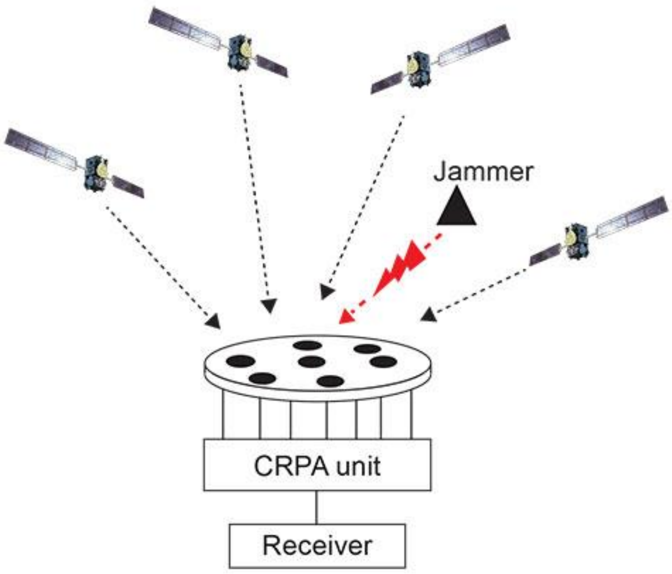

Figure 6.13: CRPA unit is receiving satellite and jammer signals.

The need is, therefore, from the antenna side, to develop miniaturized high-performance arrays, with reduced footprints, though maintaining as much as possible the capabilities (i.e., gain and bandwidth) of larger arrays. The quest for small antennas satisfying both gain and bandwidth requirements has been an active topic of research over the last decades. Several miniaturization techniques have been proposed (for a wide review see [138]), with the use of materials having a high dielectric constant being one of the most common.

Moreover, in order to have a compact system, a total antenna array footprint miniaturization has to be achieved. The array size has, thus, to shrink, meaning that the single antennas will be electrically closer to each other. Such aim is by no means easily achieved, as higher degrees of miniaturization also imply increased mutual coupling and more difficult antenna matching [139]–[141]. Various efforts to solve this problem are found in the literature, e.g., by the means of adding a decoupling and matching network [142]–[144] able to decouple the coupled patterns of the antennas, or by using, for instance or split-ring resonators [145]–[147] to limit the coupling between the elements' ports. These techniques are, however, manufacturing-intensive and cannot always be implemented, e.g., due to requirements on simplicity and versatility.

6.4.1 Antenna Array Configurations and Performances

It is necessary to understand how the design parameters affect antenna performance. To optimize the antenna performance, some important design parameters and their effects are studied. There are two designs presented in this section. In the first design, the five-element array antenna has been proposed (see Figure 6.14). Meanwhile, the second design which is a four-element array (Figure 6.21) has been proposed to have a compact system with a good performance.

6.4.1.1 Five-elements array antenna

The geometry of the proposed antenna array is shown in Figure 6.14 and Table 6.2. The substrate materials for the circuit board is the low-cost FR4 with a relative permittivity of 4.3 and a thickness of 1.6 mm.

The five elements of the array are placed sequentially rotated with a phase of 0°, 72°, 144°, 216°, and 288°. These sequentially rotated configurations produce a broad axial ratio bandwidth. The space between two adjacent elements is selected to be 80 mm, which is about 0.7 λ_0, to minimize mutual coupling without substantial degradation of the radiation pattern by the sidelobes [148].

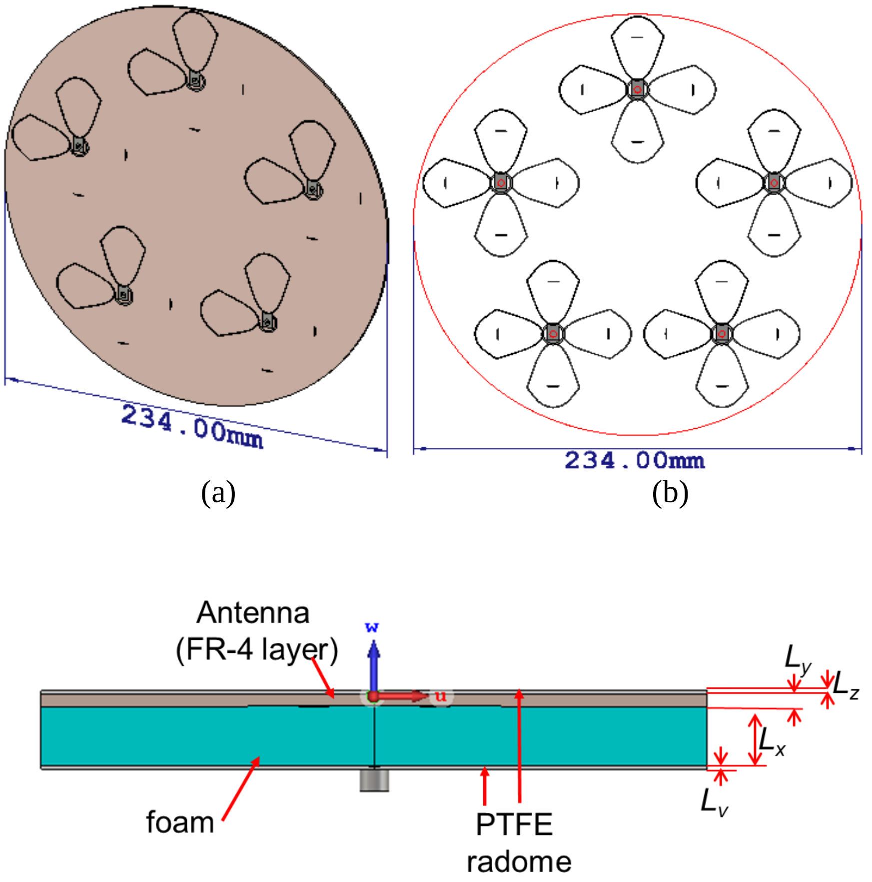

(a) (b)

(c)

Figure 6.14: Five-element antenna array configurations (a) perspective view (b) top view and (c) side view of the antenna.

Table 6.2: Dimension of The Proposed Antenna

Parameter	**Value (mm)**	**Parameter**	**Value (mm)**
L_y	0.5	L_z	8.0
L_x	1.6	L_v	0.5

The RF signal is fed to a 5-way power divider for each elements array. The antenna array scanning is simulated using CST Microwave Studio as shown in Figure 6.15. Each of the power divider output is then fed to an individual phase shifter for each antenna element of each element array where various phase progression was made to enable beam steering. The phase shifter outputs are finally connected to the antenna array.

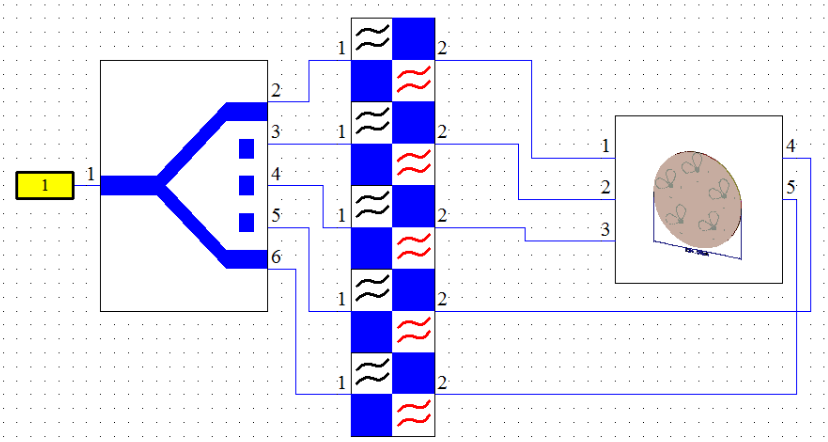

Figure 6.15: Array scanning setup for five elements array in CST MWS.

The antenna array covers the frequency range of 0.974 – 2.342 GHz as shown in Figure 6.16. The antenna has a total efficiency greater than 90% throughout 0.971 – 2.15 GHz and below 3-dB axial ratio for the entire frequency band as shown in Figure 6.18 and Figure 6.19.

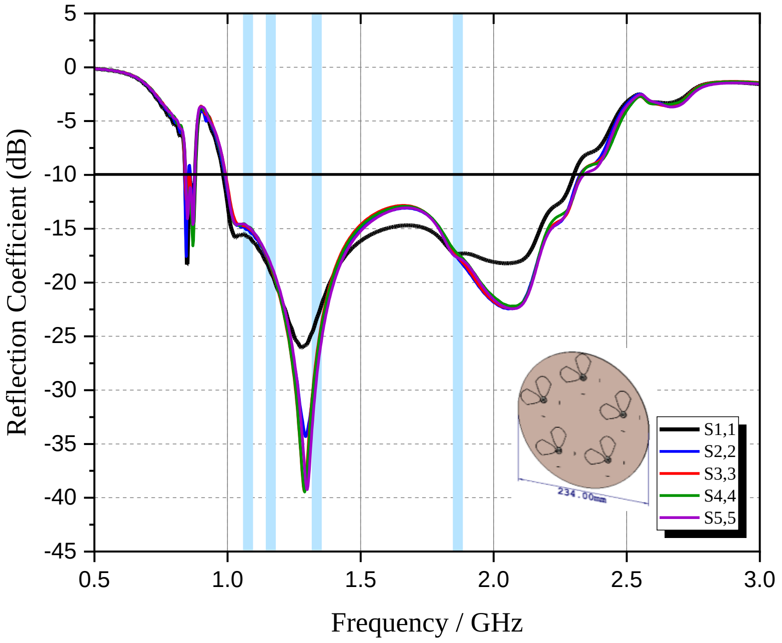

Figure 6.16: Simulated reflection coefficients of the proposed antenna.

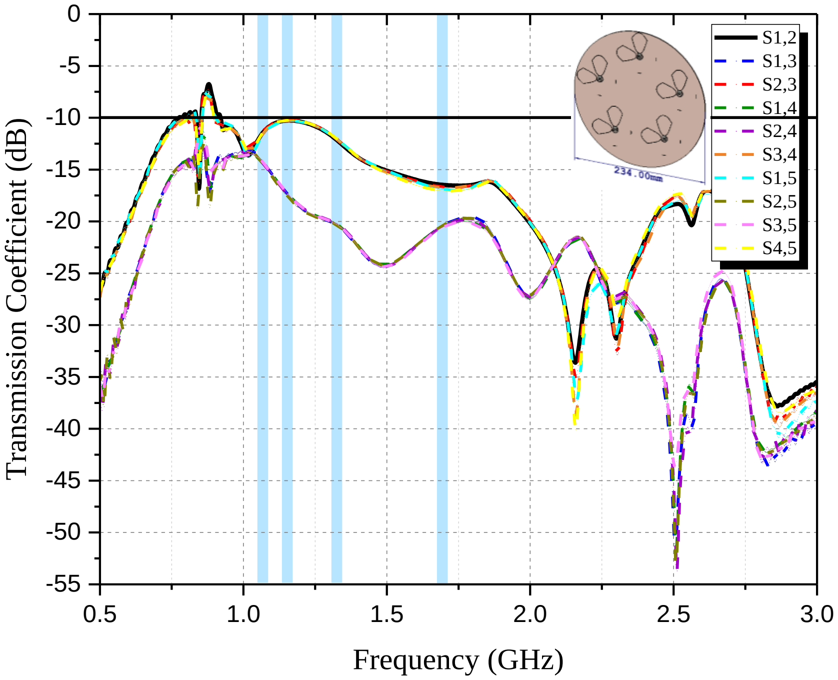

Figure 6.17: Simulated transmission coefficients of the proposed antenna.

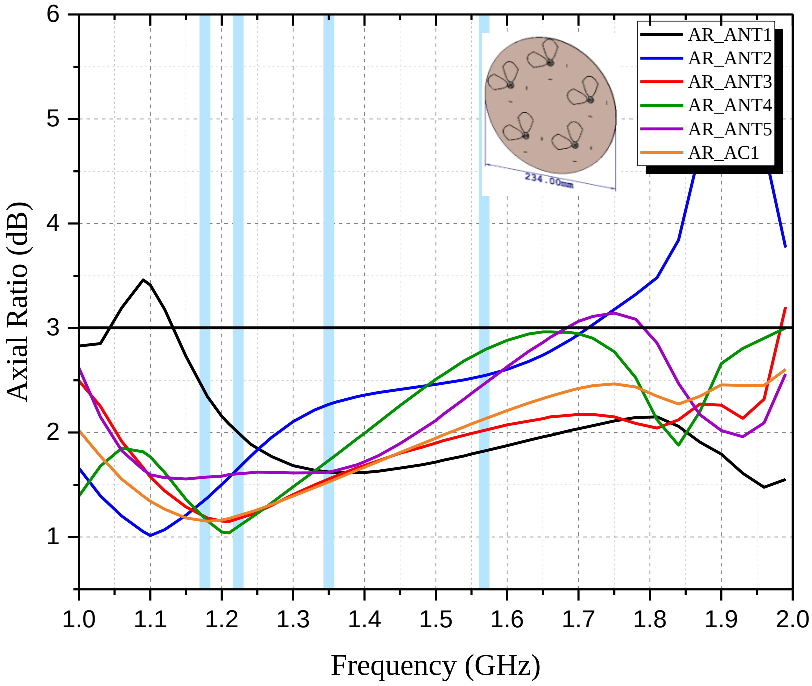

Figure 6.18: Simulated axial ratio of the proposed antenna.

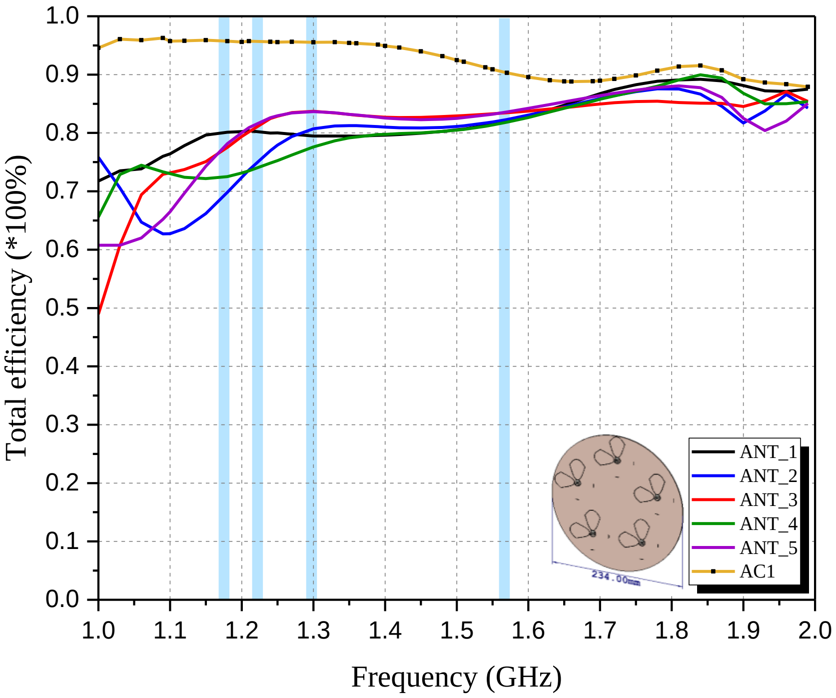

Figure 6.19: Simulated total efficiency of the proposed antenna.

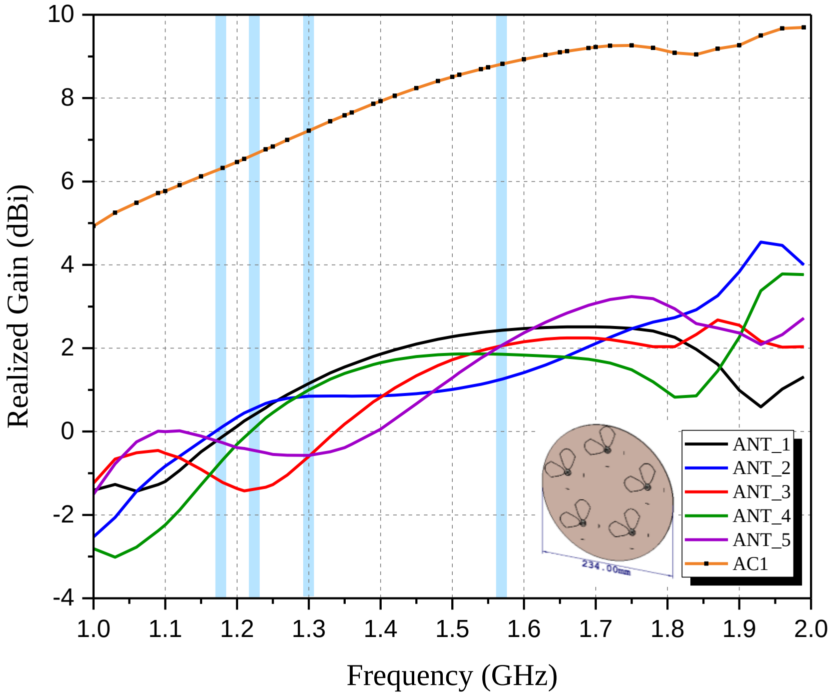

Figure 6.20: Simulated realized gain of the proposed antenna.

6.4.1.2 Four-elements array antenna

To make it more compact, the design is improved by minimizing the number of element and size of the antenna. In Figure 6.21, the four elements of the 2 × 2 arrays are placed sequentially rotated with a phase of 0°, 90°, 180°, and 270°. These sequentially rotated configurations produce a broad axial ratio bandwidth. The space between two adjacent elements is selected to be 80 mm, which is about 0.7 λ_0, to minimize mutual coupling without substantial degradation of the radiation pattern by the sidelobes [148].

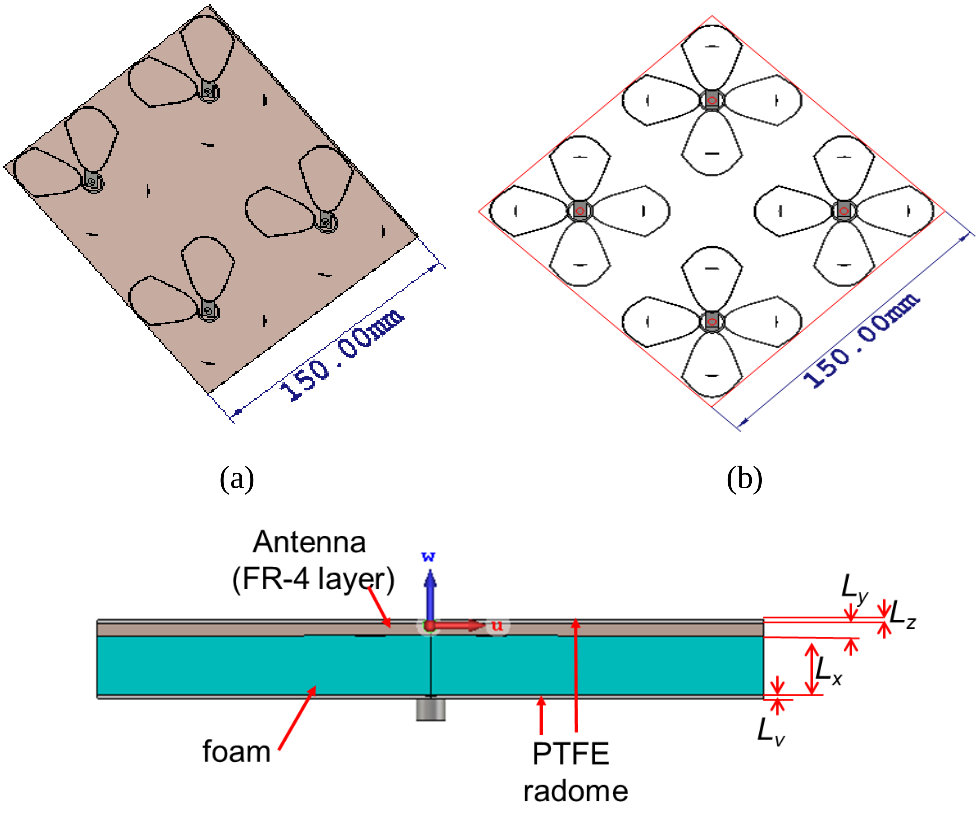

(a) (b)

(c)

Figure 6.21: Four-element antenna array configurations (a) perspective view (b) top view and (c) side view of the antenna.

Table 6.3: Dimension of The Proposed Antenna

Parameter	**Value (mm)**	**Parameter**	**Value (mm)**
L_y	0.5	L_z	8.0
L_x	1.6	L_v	0.5

The antenna array covers the frequency range of 0.959 – 2.333 GHz as shown in Figure 6.23. The antenna has a total efficiency greater than 90% below 3-dB axial ratio for the entire frequency bands as shown in Figure 6.24 and Figure 6.25 respectively.

The RF signal is fed to a 4-way power divider for each elements array. The antenna array scanning is simulated using CST Microwave Studio as shown in Figure 6.22. Each of the power divider output is then fed to an individual phase shifter for each antenna element of each element array where various phase progression was made to enable beam steering. The phase shifter outputs are finally connected to the antenna array.

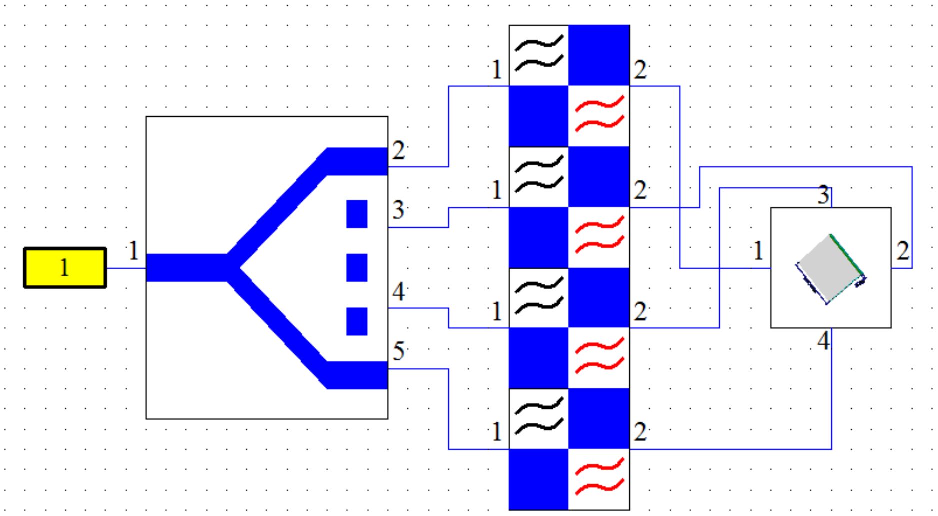

Figure 6.22: Array scanning setup for four elements array in CST MWS.

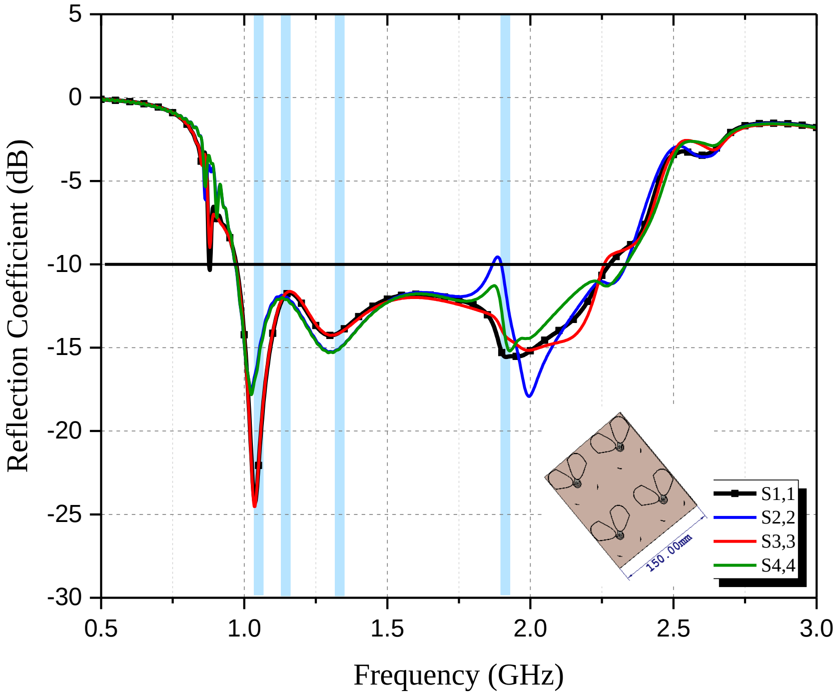

Figure 6.23: Simulated reflection coefficient of the proposed antenna.

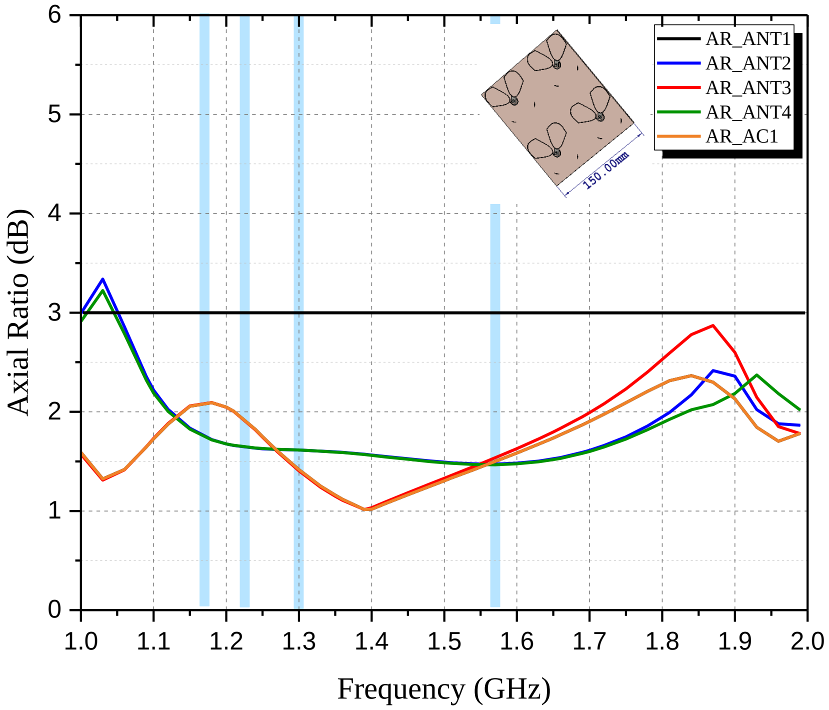

Figure 6.24: Simulated axial ratio of the proposed antenna.

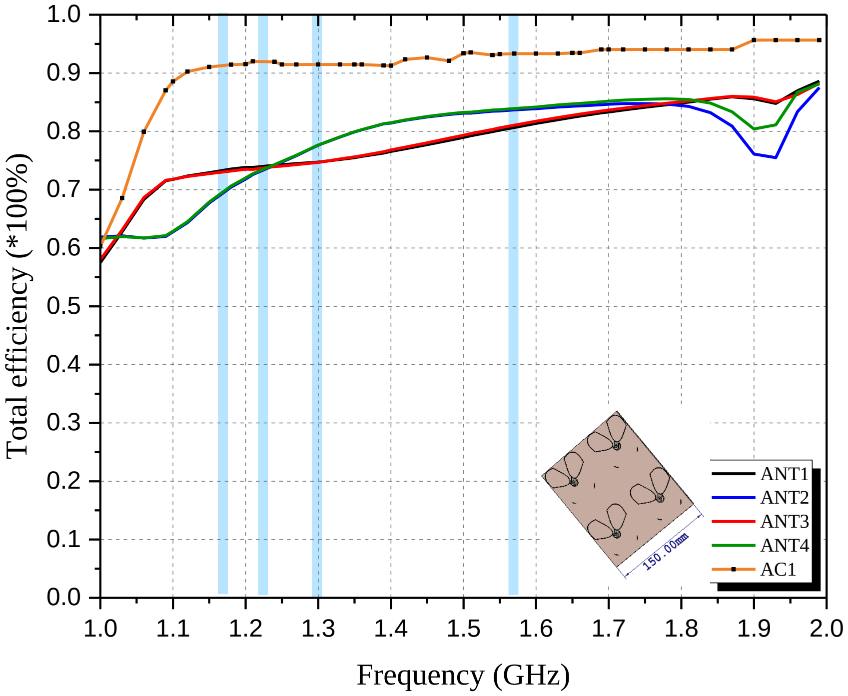

Figure 6.25: Simulated total efficiency of the proposed antenna.

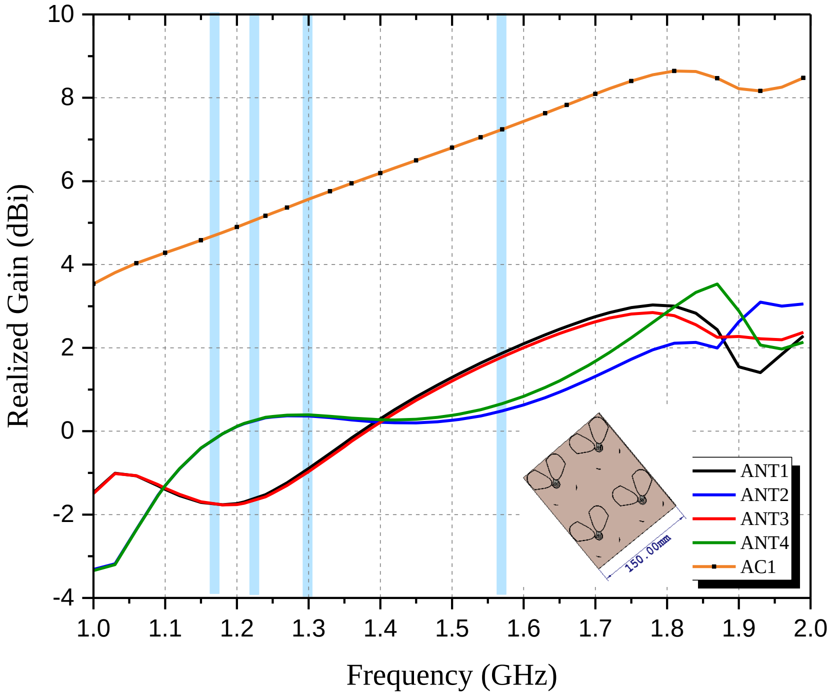

Figure 6.26: Simulated total efficiency of the proposed antenna.

6.5 ANTENNA PERFORMANCES

To prove the effectiveness of the proposed antenna for interference in practical applications, the performance of the antenna presents in this section. Here the aim is to evaluate the effect of mutual coupling in the null steering process. For this purpose, the simple 4-elements GNSS array designed in previous sections is considered. The jammer is assumed to be located at φ_j = 90° and θ_j = 90° with a jammer to signal ratio (JSR) of 30 dB. Notice that since the GPS signal is below the noise floor, the JSR can be considered as the jammer to noise ratio, also. Moreover, we consider the white Gaussian noise with $\sigma^2_n = 0.001$ in the simulations.

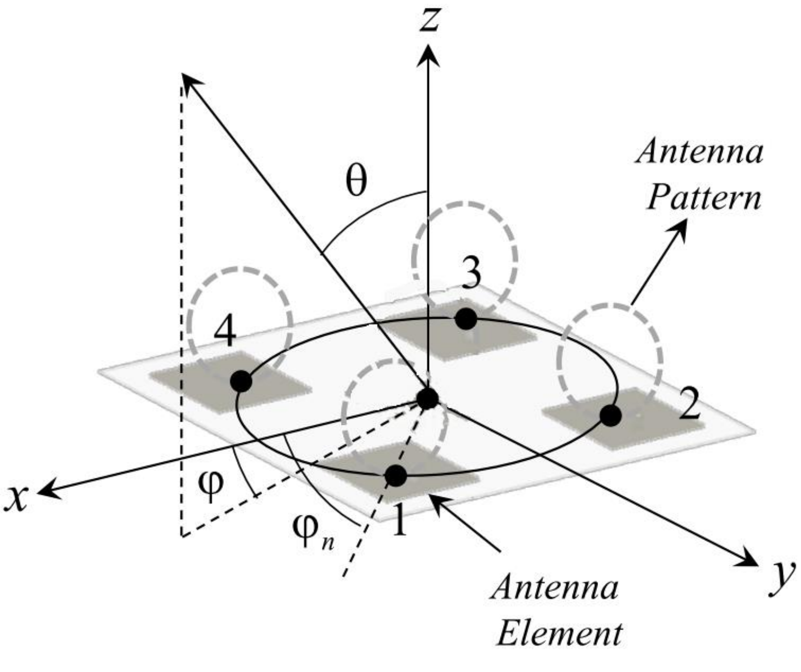

Figure 6.27: Antenna array with ideal (point source) and real radiation pattern.

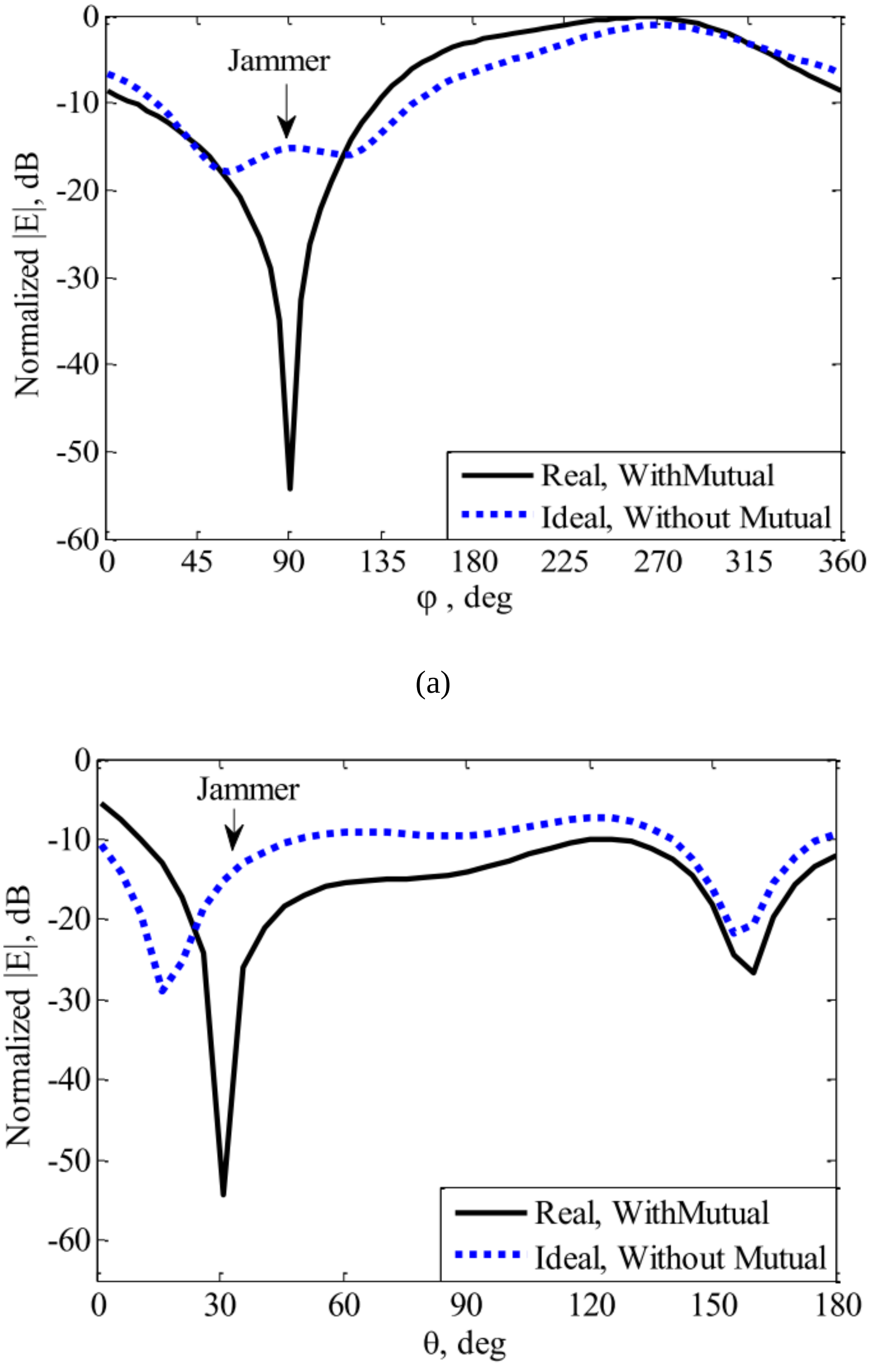

(a)

(b)

Figure 6.28: GPS Antenna array with point sources and real radiation patterns for SJR=30 dB, SNR=-20 dB and σ = 0.001. The jammer is placed at φj = 90° and θj = 90°. a) φ-plane with θj = 90° b) θ-plane with φj = 90°.

The results of using these two complex weight vectors are depicted in φ-plane with $\theta_j = 90°$ (Figure 6.28(a)) and θ-plane with $\varphi_j = 90°$ (Figure 6.28(b)). It can be seen clearly that mutual coupling affects the antenna performance, significantly. In the real case where the mutual couplings are considered, the jammer signal is encountered with more than 50 dB null depth, while it is low in the ideal case and maybe not acceptable. These results clarify the importance of mutual coupling in the extraction of the complex weight vector.

6.5.1.1 Multi Jammers

As it is well known, an array with N elements can reject N-1 jammer sources. Therefore, the method with 2, 3 and 4 jammer sources which have the same JSR as 30 dB is evaluated. The jammer sources locations in these three scenarios are tabulated in Table 6.4, and the corresponding simulation results are shown in Figure 6.30. It can be seen that the proposed method can create a proper null in the direction of jammer sources to reject their power.

Table 6.4: The Jammer Source Locations in Three Different Scenarios

Jammer Sources Scenarios	Jammer Source Locations
2- Jammer	(20°, 0°), (20°, 300°)
3- Jammer	(20°, 0°), (20° ,300°), (60°, 215°)
4- Jammer	(20°, 0°), (30° ,90°), (60°, 215°), (20°,300°)

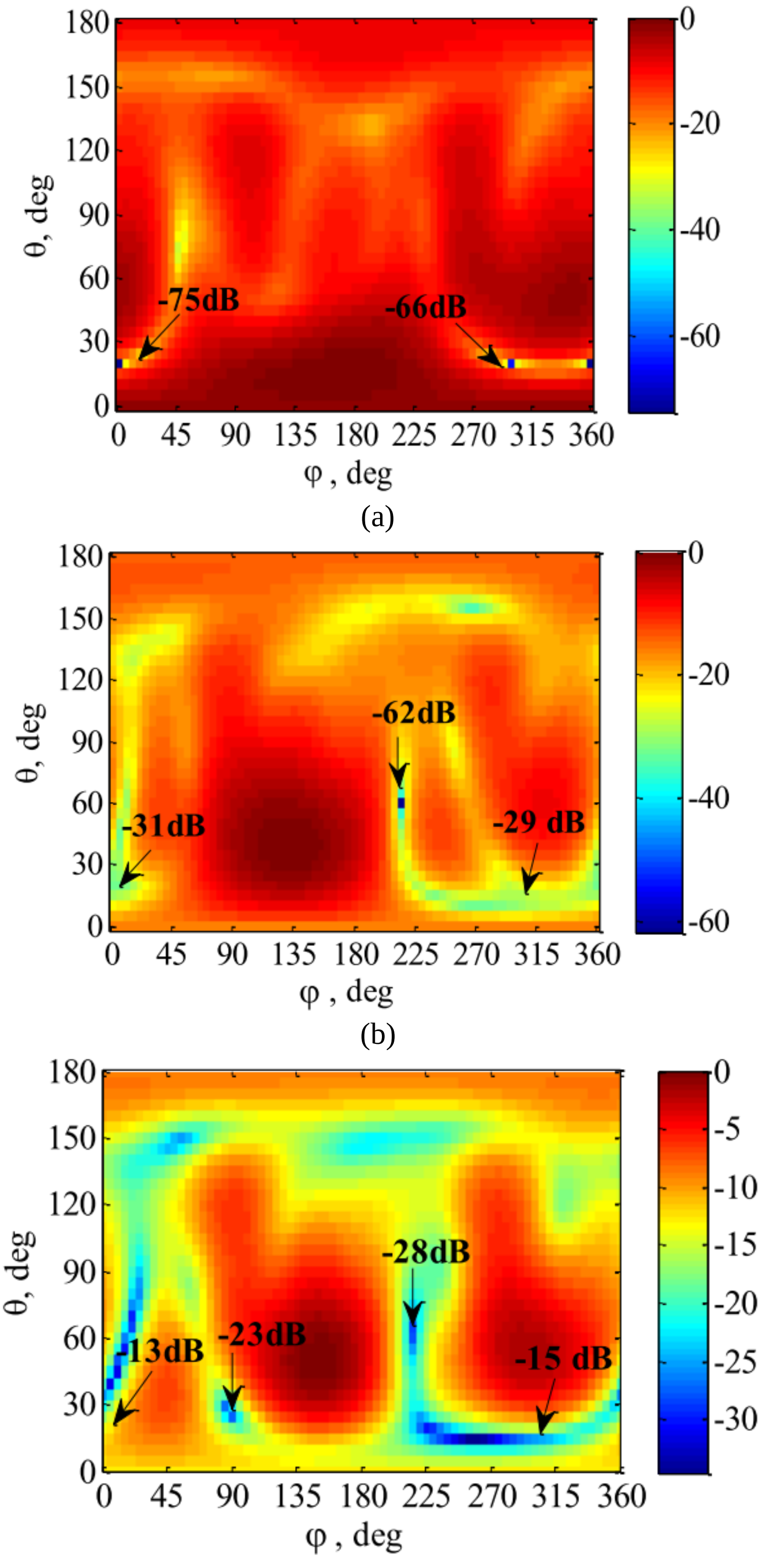

(a)

(b)

(c)

Figure 6.29: Array patterns after null steering with SJR = 50 dB for different jammer locations reported in Table 6.4.
(a) 2- jammers (b) 3- jammers (c) 4-jammers.

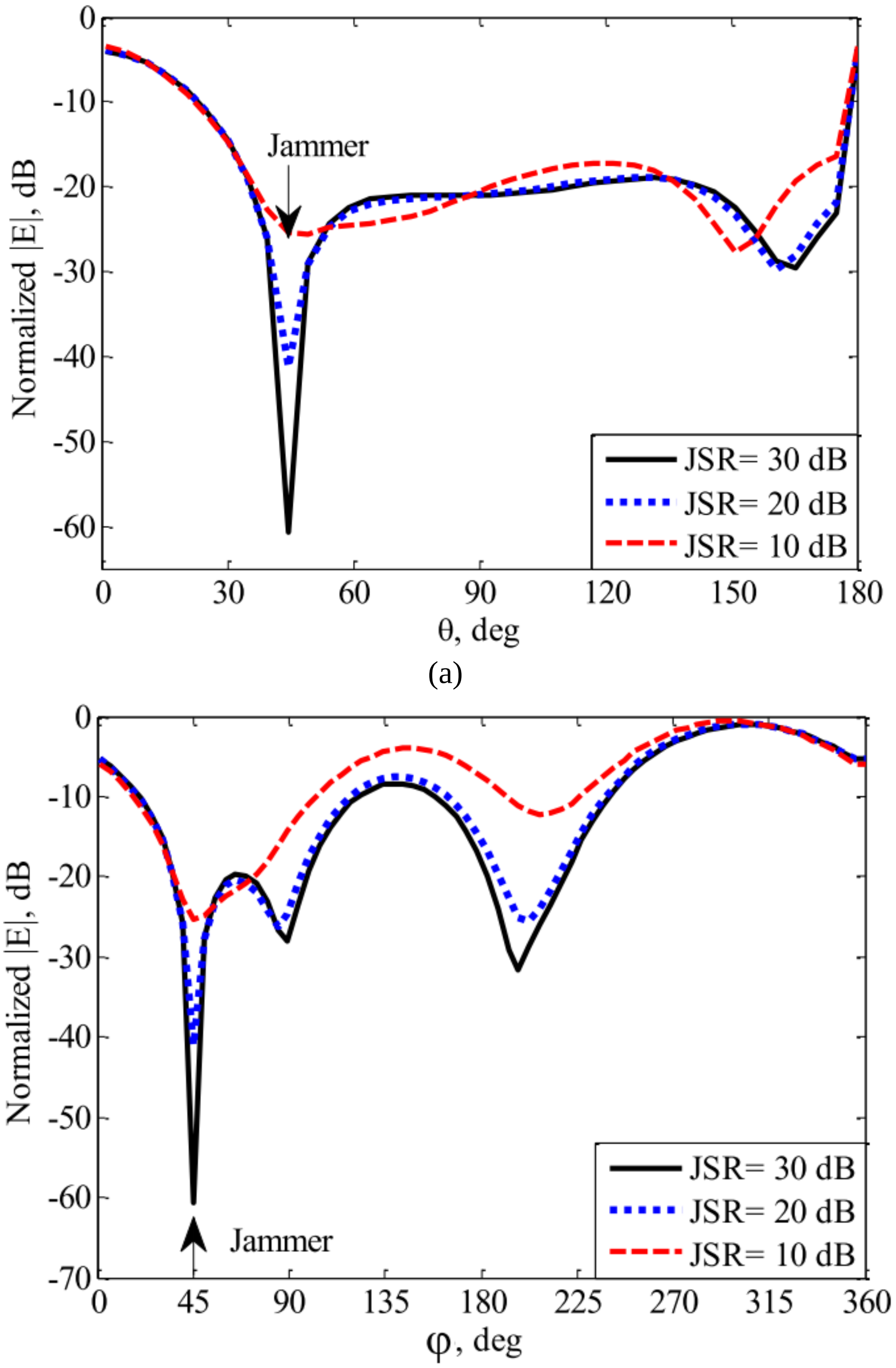

(a)

(b)

Figure 6.30: GPS Antenna with different signal to jammer ratio for SNR = -20 dB and σ = 0.001. The jammer is placed at φ_j = 45° and θ_j= 45° (a) φ-plane with θ_j = 45° (b) θ-plane with φ_j = 45°

Moreover, it can be seen that the null depth is highly related to the number of jammer sources. In other words, the results show that although the null depth is good enough in all scenarios, the null depth in the 2-jammer source scenarios is much higher than the 3 and 4-jammer source. To achieve more null depth with constant jammer sources, the number of array elements can be increased.

6.5.1.2 Jammer to Signal Effects

Since the proposed method works based on the array minimization, it is expected that JSR enhancement can help more to recognize the jammer signals from the noise. To show this fact, one jammer source in φ_j = 45° and θ_j = 45° with three different JSR as 30, 20 and 10 dB is considered. The simulation results are shown in φ-plane for θ_j = 45° (Figure 6.30 (a)) and θ-plane for φ_j = 45° (Figure 6.30 (b)). As can be seen, the null depth is related highly to the JSR. For example, we have about 60 dB null depth for JSR = 30 dB, while it is about 40 dB for JSR = 20 and only about 25 dB for JSR = 10 dB.

6.6 SUMMARY

This chapter presents a new antenna array configuration combining a 4-elements antenna array and a 5-elements antenna array to provide wide coverage. The anti-jamming performance of the antenna with respect to differently polarized jammers as well as its positioning capability are also presented. All the results have demonstrated that the antenna is an excellent candidate for the GNSS application.

An anti-jamming GNSS antenna was designed in this section. The designed antenna array was formed by four elements antenna in planar array geometry. The null steering method was performed by using the exact active element patterns of the array antenna. These patterns include the mutual coupling effect and the nearby antenna scatterer such as holder which increase the antenna performance to deal with the jammer sources which was not considered in the literature based on the author knowledge. Moreover, the proposed method can be easily used in conformal array structures due to using active antenna pattern in the method. The simulation results clarified the antenna ability to reject the jammer sources effects.

CHAPTER 7:

CONCLUSION AND RECOMMENDATIONS

The overarching questions that this thesis tries to answer are:

1) How to design compact, low profile and yet efficient CP antenna to deliver a GNSS application with high performance and wide frequency coverage?
2) How to design compact antenna arrays to meet the ever- increasing demand for wide coverage and wide bandwidth for anti-jamming GNSS applications?

In the first part, this thesis provided an overview of state of the art and extended the understanding of GNSS systems and fundamentals from an antenna and propagation perspective to propose and design a new and interesting compact antenna. In the second part, requirements of the compact GNSS antennas have been analyzed and various designs have been proposed to achieve these stringent requirements. The requirements included wide bandwidth, wide coverage, CP capability and low cost of production. In this chapter, the contributions of this thesis to the development of novel antennas are summarized. Section 7.1 provides a summary of the research work. The key contributions of this thesis are discussed in Section 7.2. Some suggestions for future work are discussed in Section 7.3.

7.1 CONCLUSION

This thesis sets out to explore appropriate miniaturization methods for reducing the size of antennas for GNSS systems. The motivation for this study stems from the desire to develop a compact GNSS antenna that would provide a broad bandwidth at GNSS frequency bands which is from 1.1 GHz to 1.6 GHz. CP was desired with an axial ratio of less than 3dB over each band, with a minimum gain of 0 dBi. Due to the requirements of bandwidth, CP with the low axial ratio, and gain, many miniaturization methods fail to meet the required performance.

In **Chapter 1**, the problem was defined, and the motivation of this research was discussed. The objectives of the study were defined with the goal of developing a compact circularly polarized antenna for GNSS applications. In **Chapter 2**, an overview of the studies of antennas for target application of GNSS systems been presented. Some important techniques for anti-jamming have been discussed in detail.

Following a thorough investigation of the limitations of the existing designs and understanding the antenna fundamentals, an overview of the current state of the art of the GNSS receiver antenna designs has been introduced in **Chapter 3**. The knowledge and prior work presented in this chapter could help readers to understand state of the art in antenna designs and also realize the research challenges of this topic. It should be valuable for researchers who are presently working on this topic and who are going to investigate this area in the near future.

In **Chapter 4**, the study was focused on the design of a crossed-dipole antenna with parasitic elements. This broadband antenna demonstrates a significant improvement on bandwidth and radiation pattern by using the parasitic elements and loaded monopoles that are excited by coupling with the elliptical crossed dipole in the center of the antenna. The structure of the antenna is compact and unique. The dimension of the antenna is 90 mm × 90 mm × 15.5 mm which is small and compact. The proposed antenna has a bandwidth of 1.06 to 1.671 GHz (611 MHz) for impedance matching $|S_{11}| < -10$ dB, and 1.093 to 1.257 GHz (164 MHz) and 1.542 to 1.666 GHz (124 MHz) for an AR < 3-dB. All the results have been demonstrated that the antenna is an excellent candidate for the GNSS application.

In **Chapter 5**, a new way of designing a dual-band CP antenna by integrating a CP radiator with a finite AMC surface were introduced and their application in protecting dipole antenna from metallic objects was reviewed. The antenna demonstrates a low-profile broadband characteristic and excellent CP radiation for GNSS frequency bands. The size of the AMC surface was a crucial factor in defining the original and additional operating CP bands of the antenna. The measured results of the proposed design with a size of $100 \times 100 \times 10$ mm^3 FR-4 material AMC and yielded an impedance bandwidth of 1.196 to 2.176 GHz for the $|S_{11}|<-10$dB and 3-

dB AR bandwidths of 1.148 to 1.761 GHz. Meanwhile, the measured results of the proposed design with a size of 100 × 100 × 12.7 mm^3, Rogers RT6006 material AMC and yielded an impedance bandwidth of 1.153 to 2.36 GHz for the $|S_{11}|<-10$dB and 3-dB AR bandwidths of 1.170 – 1.970 GHz. Additionally, the proposed antenna exhibited RHCP and high radiation efficiency (> 90%) in both bands. With a low profile, broadband characteristics, and high radiation efficiency, the proposed antenna could be widely applied to dual-band GNSS applications as well as in many other kinds of satellite communications.

In **Chapter 6**, this chapter also presents a new antenna array configuration combining a 4-elements antenna array and a 5-elements antenna array to provide wide coverage. The anti-jamming performance of the antenna with respect to differently polarized jammers as well as its positioning capability are also presented.

7.2 LIMITATION AND FUTURE WORK

Based on the conclusions above and considering the limitations of the work existed, many directions for further improvement and development present themselves. The following topics provide potential short-term and long-term directions for future work.

- As these systems become more established and integrated into mainstream receivers, so will the jammers designed to impede the receivers' performance. Therefore, it is recommended that this work be expanded in addition to bearing in mind a unified jamming detection platform that operates on multi-GNSS receivers. Modifications to the methods proposed in this thesis should be applied when considering other GNSSs, nonetheless, the approaches and the methodologies followed remain similar. It is foreseeable that the application of this research to different GNSSs will pose different challenges depending on the signals under study.

- Decoupling techniques to improve the antenna array isolation needs to be explored for miniaturization of antenna arrays.
- It is challenging to implement a broadband antenna element in an array configuration. The spacing between the adjacent antenna elements needs to be optimized for both the frequency bands. If the antenna element spacing is set as 0.5 λ for the higher band, the isolation performance for the lower band becomes poor. If the antenna element spacing is around 0.5 λ for the lower band, the increase in the grating lobes reduces the realized gain in the higher band. Using appropriate dummy parasitic elements could be a solution for this issue and needs further study.
- For the case of a single-element antenna, this could be done by collecting live data from a differential GNSS receiver and post-processing it in order to estimate antenna-induced biases. These biases could then be compared to chamber measurements. This would confirm that the calibration is of sufficient quality despite environmental effects and other sources of uncertainty.
- In the case of an antenna array, STAP hardware would be required; however, it would offer considerable credibility to the proposed approach.

The future work in GNSS antenna application is not limited to the works proposed in this thesis. Vastly broadened spectra and constellations of over 100 MEO and GEO satellites in GNSS are game-changing events that are reshaping antenna requirements toward much broader bandwidth and higher cutoff elevation angle. They pose new challenges not faced by conventional GPS and give rise to new features and applications as well as cost structures. For size reduction, the slow-wave technology appears to be a practical solution for applications from handheld to medium platform but needs considerable research. For pattern control, in particular higher cutoff angle above horizon, use of metamaterial will be pursued by some, especially for medium and large platforms. Smart antenna techniques will be developed to enhance performance in small and handheld platforms in the increasingly noisier terrestrial environment. There is no doubt an exciting future is waiting for this technology.

END

References

[1] B. W. Parkinson, J. J. Spilker, P. Axelrad, P. Enge, and American Institute of Aeronautics and Astronautics., *The Global Positioning System : Theory and Applications*, Volume 1. American Institute of Aeronautics and Astronautics, 1996.

[2] E. Kaplan and C. Hegarty, *Understanding GPS Principles and Applications : Principles and Applications.* Artech House, 2005.

[3] P. Misra and P. Enge, *Global Positioning System : Signals, Measurements, and Performance*. Ganga-Jamuna Press, 2011.

[4] Wei Liu, Xingqun Zhan, Li Liu, and Mancang Niu, "GNSS RF Compatibility Assessment: Interference among GPS, Galileo, and Compass : GPS World," *GPS World*, 2010. [Online]. Available: https://www.gpsworld.com/gnss-rf-compatibility-assessment-10837/.

[5] Thomas A. Stansell, Kenneth W. Hudnut, and Richard G. Keegan, "Future Wave: L1C Signal Performance and Receiver Design : GPS World," *GPS World*, 2011. [Online]. Available: https://www.gpsworld.com/gnss-systemgps-modernizationfuture-wave-11401/.

[6] J. J. H. Wang, "Antennas for Global Navigation Satellite System (GNSS)," *Proc. IEEE*, vol. 100, no. 7, pp. 2349–2355, Jul. 2012.

[7] Bruce R. Schupler and Thomas A. Clark, "Characterizing the Behavior of Geodetic GPS Antennas," *GPS World*, pp. 48–55, 2001.

[8] A. Kumar, A. D. Sarma, E. Ansari, and K. Yedukondalu, "Improved Phase Center Estimation for GNSS Patch Antenna," *IEEE Trans. Antennas Propag.*,

vol. 61, no. 4, pp. 1909–1915, 2013.

[9] L. Shafai, S. K. Sharma, B. Balaji, A. Damini, and G. Haslam, “Multiple phase center performance of reflector antennas using a dual mode horn,” *IEEE Trans. Antennas Propag.*, vol. 54, no. 11, pp. 3407–3417, Nov. 2006.

[10] W. Kunysz, “Antenna phase center effects and measurements in GNSS ranging applications,” in *2010 14th International Symposium on Antenna Technology and Applied Electromagnetics and the American Electromagnetics Conference, ANTEM/AMEREM 2010*, 2010.

[11] X. Wang, J. Yao, X. Lu, and W. Lu, “Research on phase center stability of circularly polarized patch antennas for GPS applications,” in *Proceedings of the 2015 IEEE 4th Asia-Pacific Conference on Antennas and Propagation, APCAP 2015*, 2016, pp. 362–365.

[12] D. M. Pozar, *Microwave Engineering, 4th Edition | Wiley*, 4th ed. Hoboken, NJ : Wiley, 2012.

[13] IEEE Antennas and Propagation IEEE Antennas and Propagation Society, *IEEE Standard Definitions of Terms for Antennas*. 1993.

[14] C. E. Balanis, *Antenna Theory: Analysis and Design, 3rd Edition*. 2005.

[15] John D. Kraus, *Antennas*, 2nd ed. McGraw-Hill, 1988.

[16] H. M. Al-Lawati, “Design and Analysis of Low Profile Circularly Polarised Antennas,” University of Sheffield, UK, 2014.

[17] J. D. Kraus and R. J. Marhefka, *Antennas for All Applications*, vol. 1, no. 3rd Edition. 2002.

[18] S. S. Gao; Q. Luo; F. Zhu, *Circularly Polarized Antennas*. Chichester, West Sussex: John Wiley & Sons, Ltd, 2014.

[19] Y. Huang and K. Boyle, *Antennas : From Theory to Practice*. John Wiley &

Sons, 2008.

[20] W. Kunysz, “Effect of Antenna Performance on the GPS Signal Accuracy,” in *Proceedings of the 1998 National Technical Meeting of The Institute of Navigation*, 1998, pp. 575–580.

[21] G. J. K. Moernaut and D. Orban, “GNSS Antennas An Introduction to Bandwidth, Gain Pattern, Polarization, and All That,” *GPS World*, pp. 42–48, 2009.

[22] D. B. Thornberg, D. S. Thornberg, M. F. Dibenedetto, M. S. Braasch, F. Van Graas, and C. Bartone, “LAAS Integrated Multipath-Limiting Antenna,” *J. Inst. Navig.*, vol. 50, no. 2, pp. 117–130, Jun. 2003.

[23] M. Braasch, “Optimum Antenna Design for DGPS Ground Reference Stations,” in *Proceedings of the 7th International Technical Meeting of the Satellite Division of The Institute of Navigation (ION GPS 1994)*, 1994, pp. 1291–1297.

[24] I. M. Barton, “Antenna Performance Analysis for The Nationwide Differential Global Positioning System,” Ohio University, 2005.

[25] F. van Graas, C. Bartone, and T. Arthur, “GPS Antenna Phase and Group Delay Corrections,” in *Proceedings of the 2004 National Technical Meeting of The Institute of Navigation*, 2004, pp. 399–408.

[26] L. J. Chu, “Physical Limitations of Omni-Directional Antennas,” *J. Appl. Phys.*, vol. 19, no. 12, pp. 1163–1175, Dec. 1948.

[27] R. C. Johnson and H. Jasik, *Antenna Engineering Handbook.* McGraw-Hill, 1984.

[28] C. A. Balanis, *Modern Antenna Handbook.* Wiley, 2011.

[29] C.-C. Chen, S. S. Gao, and M. Maqsood, “Antennas for Global Navigation

Satellite System Receivers," in *Space Antenna Handbook*, Chichester, UK: John Wiley & Sons, Ltd, 2012, pp. 548–595.

[30] B. R. Rao, W. Kunysz, R. Fante, and K. McDonald, *GPS/GNSS Antennas*. Artech House, 2012.

[31] J. J. H. Wang, "The Spiral as a Traveling Wave Structure for Broadband Antenna Applications," *Electromagnetics*, vol. 20, no. 4, pp. 323–342, Jul. 2000.

[32] J. J. H. Wang and D. J. Triplett, "High-performance Universal GNSS Antenna and Enhancement Techniques to Overcome Its Performance Limitations," in *2010 IEEE Antennas and Propagation Society International Symposium*, 2010, pp. 1–4.

[33] "Official U.S. government information about the Global Positioning System (GPS) and related topics." [Online]. Available: https://www.gps.gov/systems/gps/space/.

[34] G. Xu, *GPS : Theory, Algorithms, and Applications*. Springer, 2007.

[35] J. Farrell and M. Barth, *The Global Positioning System and Inertial Navigation*. McGraw-Hill, 1999.

[36] D. Doberstein, *Fundamentals of GPS Receivers : A Hardware Approach*. Springer, 2012.

[37] "GLONASS Interface Control Document (ICD)," 2002. [Online]. Available: http://www.glonass-ianc.rsa.ru/.

[38] "IEEE Standard Test Procedures for Antennas," *ANSI/IEEE Std 149-1979*, 1979. [Online]. Available: doi: 10.1109/IEEESTD.1979.120310.

[39] L. Musumeci and F. Dovis, "Use of the Wavelet Transform for Interference Detection and Mitigation in Global Navigation Satellite Systems," *Int. J.*

Navig. Obs., vol. 2014, pp. 1–14, Feb. 2014.

[40] R. Bauernfeind, T. Kraus, A. S. Ayaz, D. Dötterböck, and B. Eissfeller, "Analysis, Detection and Mitigation of In Car GNSS Jammer Interference Inn Intelligent Transport Systems," in *Deutscher Luft- und Raumfahrtkongress 2012*, 2012, pp. 1–10.

[41] D. Borio, C. O'Driscoll, and J. Fortuny, "GNSS Jammers: Effects and Countermeasures," in *2012 6th ESA Workshop on Satellite Navigation Technologies (Navitec 2012) & European Workshop on GNSS Signals and Signal Processing*, 2012, pp. 1–7.

[42] Michael Jones, "The Civilian Battlefield: Protecting GNSS Receivers from Interference and Jamming," *Inside GNSS*, pp. 40–49, 2011.

[43] M. Marcus, "Growing Consumer Interest in Jamming: Spectrum Policy Implications [Spectrum Policy and Regulatory Issues]," *IEEE Wirel. Commun.*, vol. 21, no. 1, pp. 4–4, Feb. 2014.

[44] A. Georgiadis, *Microwave and Millimeter Wave Circuits and Systems : Emerging Design, Technologies and Aapplications*. John Wiley & Sons, 2012.

[45] D. Borio, C. O'Driscoll, and J. Fortuny, "Jammer Impact on Galileo and GPS Receivers," in *2013 International Conference on Localization and GNSS (ICL-GNSS)*, 2013, pp. 1–6.

[46] M. Moussa, "High Resolution Jamming Detection in Global Navigation Satellite Systems," Queen's University Kingston, Ontario, Canada, 2015.

[47] Emily McMilin, "Single Antenna Null-Steering for GPS & GNSS Aerial Applications," Stanford University, 2016.

[48] S. D. A, "GNSS Interference Mitigation Using Antenna Array Processing,"

University of Calgary, Aberta, 2013.

[49] S. Deshpande, “Study of Interference Effects on GPS Signal Acquisition,” University of Calgary, 2004.

[50] B. D. Van Veen and K. M. Buckley, “Beamforming: A Versatile Approach to Spatial Filtering,” *IEEE ASSP Mag.*, vol. 5, no. 2, pp. 4–24, Apr. 1988.

[51] J. Li, “GPS Interference Mitigation for Small UAV Applications,” The University of Adelaide, 2009.

[52] M. Trinkle and D. Gray, “GPS Interference Mitigation; Overview and Experimental Results,” in *5th International Symposium on Satellite Navigation Technology & Applications*, 2001.

[53] Wang Lijun and Miao Huanping, “The System Model and Analysis of All-Digital Temporal and Spatial Anti-jamming for GPS Receivers,” in *IET 3rd International Conference on Wireless, Mobile and Multimedia Networks (ICWMMN 2010)*, 2010, pp. 258–261.

[54] C. Xue, H. Wang, X. Jiang, and Y. Huang, “A Single-Feed Arrow-Shaped Circularly Polarized Antenna With Unbalanced Slotted Artificial Magnetic Conductor for GNSS Application,” in *2016 IEEE MTT-S International Microwave Workshop Series on Advanced Materials and Processes for RF and THz Applications (IMWS-AMP)*, 2016, pp. 4–6.

[55] S. X. Ta, J. J. Han, I. Park, and R. W. Ziolkowski, “Wide-Beam Circularly Polarized Crossed Scythe-Shaped Dipoles for Global Navigation Satellite Systems,” *J. Electromagn. Eng. Sci.*, vol. 13, no. 4, pp. 224–232, 2013.

[56] S. X. Ta, H. Choo, I. Park, and R. W. Ziolkowski, “Multi-Band, Wide-Beam, Circularly Polarized, Crossed, Asymmetrically Barbed Dipole Antennas for GPS Applications,” *IEEE Trans. Antennas Propag.*, vol. 61, no. 11, pp. 5771–

5775, Nov. 2013.

[57] S. X. Ta and I. Park, “Crossed Dipole Loaded With Magneto-Electric Dipole for Wideband and Wide-Beam Circularly Polarized Radiation,” *IEEE Antennas Wirel. Propag. Lett.*, vol. 14, pp. 358–361, 2015.

[58] J.-W. W. Baik, T.-H. H. Lee, S. Pyo, S.-M. M. Han, J. Jeong, and Y.-S. S. Kim, “Broadband Circularly Polarized Crossed Dipole with Parasitic Loop Resonators and Its Arrays,” *IEEE Trans. Antennas Propag.*, vol. 59, no. 1, pp. 80–88, Jan. 2011.

[59] S. Hu, X. Chen, and D. Zhao, “Novel Compact Monopole Antennas for Global Navigation Satellite Systems,” in *2015 IEEE 4th Asia-Pacific Conference on Antennas and Propagation (APCAP)*, 2015, pp. 210–211.

[60] Y. Cao, S. W. Cheung, and T. I. Yuk, “A Simple Planar Polarization Reconfigurable Monopole Antenna for GNSS/PCS,” *IEEE Trans. Antennas Propag.*, vol. 63, no. 2, pp. 500–507, Feb. 2015.

[61] R. Xu, J.-Y. Li, and W. Kun, “A Broadband Circularly Polarized Crossed-Dipole Antenna,” *IEEE Trans. Antennas Propag.*, vol. 64, no. 10, pp. 4509–4513, Oct. 2016.

[62] A. Selek, C. Turkmen, and M. Secmen, “Compact planar folded monopole antenna with coupling mechanism for Quad ISM band, GNSS and UMTS applications,” in *GeMiC 2018 - 2018 German Microwave Conference*, 2018, vol. 2018-January, pp. 211–214.

[63] G. B. Abdelsayed, S. I. Shams, and a. M. M. a Allam, “Triple-band Circularly Polarized Slotted Patch Antenna for GPS and UMTS Systems,” in *2010 10th Mediterranean Microwave Symposium, MMS 2010*, 2010, pp. 448–451.

[64] C. Chen, X. Zhang, S. Qi, and W. Wu, “Wideband Circular Polarization

Cavity-Backed Slot Antenna for GNSS Applications," *Prog. Electromagn. Res. Lett.*, vol. 52, no. February, pp. 31–36, 2015.

[65] Nasimuddin, X. Qing, and Z. N. Chen, "A Compact Circularly Polarized Slotted Patch Antenna for GNSS Applications," *IEEE Trans. Antennas Propag.*, vol. 62, no. 12, pp. 6506–6509, Dec. 2014.

[66] S. B. Sharma, A. Ugle, and K. Parikh, "A Novel U-slot Aperture Coupled Annular-Ring Microstrip Patch Antenna for Multiband GNSS Applications," in *14th European Conference on Antennas and Propagation, EuCAP 2020*, 2020.

[67] Nasimuddin and X. Qing, "A Single-feed Compact Wideband Circularly Polarized Antenna for INMARSAT/GNSS Applications," in *14th European Conference on Antennas and Propagation, EuCAP 2020*, 2020.

[68] H. Zhang, Y. Guo, and G. Wang, "A Wideband Circularly Polarized Crossed-Slot Antenna with Stable Phase Center," *IEEE Antennas Wirel. Propag. Lett.*, vol. 18, no. 5, pp. 941–945, May 2019.

[69] A. Alphones, K. Agarwal, and Nasimuddin, "Triple-band Compact Circularly Polarised Stacked Microstrip Antenna Over Reactive Impedance Meta-surface for GPS Applications," *IET Microwaves, Antennas Propag.*, vol. 8, no. 13, pp. 1057–1065, 2014.

[70] O. P. Falade, M. U. Rehman, Y. Gao, X. Chen, and C. G. Parini, "Single Feed Stacked Patch Circular Polarized Antenna for Triple Band GPS Receivers," *IEEE Trans. Antennas Propag.*, vol. 60, no. 10, pp. 4479–4484, 2012.

[71] J. M. Baracco, L. Salghetti-Drioli, and P. de Maagt, "AMC Low Profile Wideband Reference Antenna for GPS and GALILEO Systems," *IEEE Trans. Antennas Propag.*, vol. 56, no. 8 II, pp. 2540–2547, 2008.

[72] Moran Wang, Xiaoqiao Deng, and Changqing Gu, “Tri-band GPS Antenna with Low-Multipath Ground Plane,” in *2010 International Symposium on Signals, Systems and Electronics*, 2010, vol. 2, pp. 1–4.

[73] U. U. Hussine, M. T. Islam, and N. Misran, “A New I Slotted Compact Microstrip Antenna for L1 & L2 Bands,” in *2011 IEEE International Conference on Space Science and Communication*, 2011, pp. 286–290.

[74] N. Rezazadeh and L. Shafai, “A Compact Microstrip Patch Antenna for Civilian GPS Interference Mitigation,” *IEEE Antennas Wirel. Propag. Lett.*, vol. 6, no. c, pp. 7–10, 2018.

[75] M. Khalily, M. K. a Rahim, and A. a. Kishk, “Planar Wideband Circularly Polarized Antenna Design with Rectangular Ring Dielectric Resonator and Parasitic Printed Loops,” *IEEE Antennas Wirel. Propag. Lett.*, vol. 11, pp. 905–908, 2012.

[76] H. Nguyen-bich, H. Chu-ba, and C. Dao-ngoc, “All GPS Bands Dielectric Resonator Antenna with Circular Polarization for GPS Application,” in *The 2012 International Conference on Advanced Technologies for Communications*, 2012, pp. 65–68.

[77] G. Massie, M. Caillet, M. Clénet, and Y. M. M. Antar, “A New Wideband Circularly Polarized Hybrid Dielectric Resonator Antenna,” *IEEE Antennas Wirel. Propag. Lett.*, vol. 9, pp. 347–350, 2010.

[78] S. Jovic, M. Clenet, and M. M. Yahia Antar, “Novel Wideband Antenna for GNSS and Satellite Communications,” in *14th European Conference on Antennas and Propagation, EuCAP 2020*, 2020.

[79] G. Mazingue, B. Byrne, M. Romier, and N. Capet, “3D Printed Ceramic Antennas for Space Applications,” in *14th European Conference on Antennas*

and Propagation, EuCAP 2020, 2020.

[80] A. Sharma, G. Das, S. Gupta, and R. K. Gangwar, “Quad-Band Quad-Sense Circularly Polarized Dielectric Resonator Antenna for GPS/CNSS/WLAN/WiMAX Applications,” *IEEE Antennas Wirel. Propag. Lett.*, vol. 19, no. 3, pp. 403–407, Mar. 2020.

[81] U. Illahi, J. Iqbal, M. I. Sulaiman, M. Alam, M. S. Mazliham, and M. H. Jamaluddin, “A Conformal Metal Strip Fed Circularly Polarized Rectangular Dielectric Resonator Antenna,” in *APACE 2019 - 2019 IEEE Asia-Pacific Conference on Applied Electromagnetics, Proceedings*, 2019.

[82] Y. Liu, Y. Jiao, Z. Weng, C. Zhang, and H. Zhang, “A high-gain dielectric resonator antenna array fed by back-cavity,” in *2018 IEEE International Workshop on Antenna Technology, iWAT2018 - Proceedings*, 2018, pp. 1–3.

[83] Son Xuat Ta, Ikmo Park, and R. W. Ziolkowski, “Crossed Dipole Antennas: A review,” *IEEE Antennas and Propagation Magazine*, vol. 57, no. 5. IEEE Computer Society, pp. 107–122, 01-Oct-2015.

[84] L. Zhang *et al.*, “Single-Feed Ultra-Wideband Circularly Polarized Antenna With Enhanced Front-to-Back Ratio,” *IEEE Trans. Antennas Propag.*, vol. 64, no. 1, pp. 355–360, Jan. 2016.

[85] J. A. Kasemodel, C.-C. Chen, I. J. Gupta, and J. L. Volakis, “Miniature Continuous Coverage Antenna Array for GNSS Receivers,” *IEEE Antennas Wirel. Propag. Lett.*, vol. 7, pp. 592–595, 2008.

[86] R. Joshi *et al.*, “Dual-Band, Dual-Sense Textile Antenna with AMC Backing for Localization Using GPS and WBAN/WLAN,” *IEEE Access*, vol. 8, pp. 89468–89478, 2020.

[87] A. J. OBrien and I. J. Gupta, “Mitigation of Adaptive Antenna Induced Bias

Errors in GNSS Receivers," *IEEE Trans. Aerosp. Electron. Syst.*, vol. 47, no. 1, pp. 524–538, Jan. 2011.

[88] Y. Zhou, C. Chen, and J. L. Volakis, "Single-fed Circularly Polarized Antenna Element with Reduced Coupling for GPS Arrays," *IEEE Trans. Antennas Propag.*, vol. 56, no. 5, pp. 1469–1472, 2008.

[89] M. Chen and C. C. Chen, "A Compact Dual-band GPS Antenna Design," *IEEE Antennas Wirel. Propag. Lett.*, vol. 12, pp. 245–248, 2013.

[90] Y. Zhou, C.-C. Chen, and J. L. Volakis, "A Compact 4-Element Dual-band GPS Array," in *2009 IEEE Antennas and Propagation Society International Symposium*, 2009, pp. 1–4.

[91] B. A. Kramer, M. Lee, C.-C. Chen, and J. L. Volakis, "A Miniature Conformal Spiral Antenna Using Inductive and Dielectric Loading," in *2007 IEEE Antennas and Propagation International Symposium*, 2007, pp. 1004–1007.

[92] Y. Zhou, S. Koulouridis, G. Kiziltas, and J. L. Volakis, "A Novel 1.5" Quadruple Antenna for Tri-Band GPS Applications," *IEEE Antennas Wirel. Propag. Lett.*, vol. 5, pp. 224–227, 2006.

[93] A. S. C. Svendsen and I. J. Gupta, "Adaptive Antenna for Handheld GPS Receivers," in *IEEE/ION Position, Location and Navigation Symposium*, 2010, pp. 436–442.

[94] H. Sedighy, "Null Steering GPS Array in the Presence of Mutual Coupling," *Iran. J. Electr. Electron. Eng.*, vol. 14, no. 2, pp. 116–123, 2018.

[95] S. X. Ta, H. H. Tran, and I. Park, "Wideband Circularly Polarized Antenna for GNSS Applications," in *2014 IEEE Conference on Antenna Measurements & Applications (CAMA)*, 2014, pp. 1–3.

[96] M. A. Fiddy and R. Tsu, "Understanding metamaterials," *Waves in Random*

and Complex Media, vol. 20, no. 2, pp. 202–222, May 2010.

[97] Fan Yang and Y. Rahmat-Samii, “Reflection Phase Characterizations of the EBG Ground Plane for Low Profile Wire Antenna Applications,” *IEEE Trans. Antennas Propag.*, vol. 51, no. 10, pp. 2691–2703, Oct. 2003.

[98] D. Sievenpiper, L. Zhang, R. F. Jimenez Broas, N. G. Alexöpolous, and E. Yablonovitch, “High-impedance electromagnetic surfaces with a forbidden frequency band,” *IEEE Trans. Microw. Theory Tech.*, vol. 47, no. 11, pp. 2059–2074, 1999.

[99] S. Clavijo, R. E. Diaz, and W. E. McKinzie, “Design Methodology for Sievenpiper High-Impedance Surfaces: An Artificial Magnetic Conductor for Positive Gain Electrically Small Antennas,” *IEEE Trans. Antennas Propag.*, vol. 51, no. 10, pp. 2678–2690, Oct. 2003.

[100] H. Mosallaei and K. Sarabandi, “Antenna Miniaturization and Bandwidth Enhancement Using a Reactive Impedance Substrate,” *IEEE Trans. Antennas Propag.*, vol. 52, no. 9, pp. 2403–2414, Sep. 2004.

[101] S. Zhu and R. Langley, “Dual-Band Wearable Textile Antenna on an EBG Substrate,” *IEEE Trans. Antennas Propag.*, vol. 57, no. 4, pp. 926–935, Apr. 2009.

[102] O. Folayan and R. Langley, “Dual Frequency Band Antenna Combined with A High Impedance Band Gap Surface,” *IET Microwaves, Antennas Propag.*, vol. 3, no. 7, p. 1118, 2009.

[103] N. A. Abbasi and R. J. Langley, “Multiband-Integrated Antenna/Artificial Magnetic Conductor,” *IET Microwaves, Antennas Propag.*, vol. 5, no. 6, p. 711, 2011.

[104] D. Chen, W. Yang, W. Che, Q. Xue, and L. Gu, “Polarization-Reconfigurable

and Frequency-Tunable Dipole Antenna Using Active AMC Structures," *IEEE Access*, vol. 7, pp. 77792–77803, 2019.

[105] E. George and C. Saha, "An AMC Backed Slotted Ground Antenna for Broadside Radiation and High Gain," in *Proceedings of the 2019 IEEE Recent Advances in Geoscience and Remote Sensing: Technologies, Standards and Applications, TENGARSS 2019*, 2019, pp. 61–63.

[106] H. Yi and S.-W. Qu, "A Novel Dual-Band Circularly Polarized Antenna Based on Electromagnetic Band-Gap Structure," *IEEE Antennas Wirel. Propag. Lett.*, vol. 12, pp. 1149–1152, 2013.

[107] D. Qu, L. Shafai, and A. Foroozesh, "Improving microstrip patch antenna performance using EBG substrates," *IEE Proc. Microwaves, Antennas Propag.*, vol. 153, no. 6, pp. 558–563, 2006.

[108] D. N. Elsheakh, H. A. Elsadek, E. A. Abdallah, H. Elhenawy, and M. F. Iskander, "Enhancement of microstrip monopole antenna bandwidth by using EBG structures," *IEEE Antennas Wirel. Propag. Lett.*, vol. 8, pp. 959–962, 2009.

[109] W. Wan, Q. Wang, and T. Ye, "Research of Low-profile High Performance new AMC Antenna for 5G mm-Wave AiP Application," in *2019 20th International Conference on Electronic Packaging Technology, ICEPT 2019*, 2019.

[110] M. Xue, W. Wan, Q. Wang, and L. Cao, "Wideband Low-Profile Ka-Band Microstrip Antenna with Low Cross Polarization Using Asymmetry AMC Structure," in *Proceedings - Electronic Components and Technology Conference*, 2019, pp. 2318–2323.

[111] M. E. de Cos, Y. Álvarez, and F. Las-Heras, "On The Influence of Coupling

AMC Resonances for RCS Reduction in The SHF Band," *Prog. Electromagn. Res.*, vol. 117, pp. 103–119, 2011.

[112] C. C. Chiau, X. Chen, and C. Parini, "Multiperiod EBG Structure for Wide Stopband Circuits," *IEE Proc. Microwaves, Antennas Propag.*, vol. 150, no. 6, pp. 489–492, Dec. 2003.

[113] L. Akhoondzadeh-Asl, "Wideband Dipoles on Electromagnetic Bandgap Ground Planes," in *IEE Wideband and Multi-band Antennas and Arrays 2005*, 2006, pp. 41–45.

[114] Y. Zhang, J. Von Hagen, M. Younis, C. Fischer, and W. Wiesbeck, "Planar Artificial Magnetic Conductors and Patch Antennas," *IEEE Trans. Antennas Propag.*, vol. 51, no. 10, pp. 2704–2712, 2003.

[115] A. P. Feresidis, G. Goussetis, S. Wang, and J. C. Vardaxoglou, "Artificial magnetic conductor surfaces and their application to low-profile high-gain planar antennas," *IEEE Trans. Antennas Propag.*, vol. 53, no. 1 I, pp. 209–215, Jan. 2005.

[116] S. Wang, A. P. Feresidis, G. Goussetis, and J. C. Vardaxoglu, "Low-Profile Resonant Cavity Antenna with Artificial Magnetic Conductor Ground Plane," *Electron. Lett.*, vol. 40, no. 7, pp. 405–406, Apr. 2004.

[117] S. H. Kim, T. T. Nguyen, and J. H. Jang, "Reflection Characteristics of 1-D EBG Ground Plane and Its Application to A Planar Dipole Antenna," *Prog. Electromagn. Res.*, vol. 120, pp. 51–66, 2011.

[118] L. Li *et al.*, "Frequency-Reconfigurable Quasi-Sierpinski Antenna Integrating with Dual-Band High-Impedance Surface," *IEEE Trans. Antennas Propag.*, vol. 62, no. 9, pp. 4459–4467, Sep. 2014.

[119] E. J. Rothwell and R. O. Ouedraogo, "Antenna Miniaturization: Definitions,

Concepts, and A Review with Emphasis on Metamaterials," *J. Electromagn. Waves Appl.*, vol. 28, no. 17, pp. 2089–2123, Nov. 2014.

[120] J. McVay, N. Engheta, and A. Hoorfar, "High Impedance Metamaterial Surfaces Using Hilbert-Curve Inclusions," *IEEE Microw. Wirel. Components Lett.*, vol. 14, no. 3, pp. 130–132, Mar. 2004.

[121] G. Goussetis, A. P. Feresidis, and J. C. Vardaxoglou, "Tailoring the AMC and EBG Characteristics of Periodic Metallic Arrays Printed on Grounded Dielectric Substrate," *IEEE Trans. Antennas Propag.*, vol. 54, no. 1, pp. 82–89, 2006.

[122] S. B. Glybovski, S. A. Tretyakov, P. A. Belov, Y. S. Kivshar, and C. R. Simovski, "Metasurfaces: From Microwaves to Visible," Elsevier B.V., May 2016.

[123] R. Dewan, S. K. A. Rahim, F. Malek, S. F. Ausordin, A. A. Yusuf, and S. N. Azemi, "A Dual-Band Array Antenna Using Dome-Shaped Radiating Patches," *Microw. Opt. Technol. Lett.*, vol. 55, no. 11, pp. 2680–2686, Nov. 2013.

[124] R. T. Ioannides, T. Pany, and G. Gibbons, "Known Vulnerabilities of Global Navigation Satellite Systems, Status, and Potential Mitigation Techniques," *Proc. IEEE*, vol. 104, no. 6, pp. 1174–1194, 2016.

[125] A. Pinker and C. Smith, "Vulnerability of the GPS Signal to Jamming," *GPS Solutions*, vol. 3, no. 2, Wiley, pp. 19–27, Oct-1999.

[126] M. M. Casabona and M. W. Rosen, "Discussion of GPS Anti-Jam Technology," *GPS Solutions*, vol. 2, no. 3, Wiley, pp. 18–23, Jan-1999.

[127] A. Konovaltsev, D. S. De Lorenzo, A. Hornbostel, and P. K. Enge, "Mitigation of Continuous and Pulsed Radio Interference with GNSS Antenna

Arrays," in *Proceedings of the 21st International Technical Meeting of the Satellite Division of The Institute of Navigation (ION GNSS 2008)*, 2008, pp. 2786–2795.

[128] Y. Guo, M. Fan, X. DIng, F. Yan, W. Xie, and M. Kong, "Analysis and Application of CNR Performance of STAP Anti-Jamming Method for GNSS Receiver," in *ICSIDP 2019 - IEEE International Conference on Signal, Information and Data Processing 2019*, 2019.

[129] X. Yang, F. Chen, W. Liu, and F. Wang, "Analysis of the Effect Jammer Types on GNSS Receiver Measurements," in *2019 2nd IEEE International Conference on Information Communication and Signal Processing, ICICSP 2019*, 2019, pp. 117–120.

[130] T. E. Humphreys, B. M. Ledvina, M. L. Psiaki, B. W. O'Hanlon, P. M. Kintner, and Jr., "Assessing the Spoofing Threat: Development of a Portable GPS Civilian Spoofer," in *Proceedings of the 21st International Technical Meeting of the Satellite Division of The Institute of Navigation (ION GNSS 2008)*, 2008, pp. 2314–2325.

[131] B. M. Ledvina, W. J. Bencze, B. Galusha, and I. Miller, "An In-Line Anti-Spoofing Device for Legacy Civil GPS Receivers," in *Proceedings of the 2010 International Technical Meeting of The Institute of Navigation*, 2010, pp. 698–712.

[132] Randolph G. Hartman, "US5557284A: Spoofing Detection System for A Satellite Positioning System," 03-Feb-1995.

[133] M. L. Psiaki, S. P. Powell, and B. W. O'Hanlon, "GNSS Spoofing Detection using High-Frequency Antenna Motion and Carrier-Phase Data," in *Proceedings of the 26th International Technical Meeting of the Satellite*

Division of The Institute of Navigation (ION GNSS+ 2013), 2013, pp. 2949–2991.

[134] S. Daneshmand, A. Jafarnia-Jahromi, A. Broumandon, and G. Lachapelle, “A Low-Complexity GPS Anti-Spoofing Method Using a Multi-Antenna Array,” in *Proceedings of the 25th International Technical Meeting of the Satellite Division of The Institute of Navigation (ION GNSS 2012)*, 2012, pp. 1233–1243.

[135] T. Humphreys, J. Bhatti, D. Shepard, and K. Wesson, “A Testbed for Developing and Evaluating GNSS Signal Authentication Techniques,” in *Proc. Int. Symp. Certification of GNSS Systems Services (CERGAL)*, 2014, pp. 1–5.

[136] J. L. Volakis, A. J. O’Brien, and C.-C. Chen, “Small and Adaptive Antennas and Arrays for GNSS Applications,” in *Proceedings of the IEEE*, 2016, vol. 104, no. 6, pp. 1221–1232.

[137] C. Song, Y. Huang, Q. Xu, and U. U. Hussine, “A Broadband Circularly Polarized Cross-dipole Antenna for GNSS Applications,” in *2015 Loughborough Antennas and Propagation Conference, LAPC 2015*, 2015.

[138] J. L. Volakis, C.-C. Chen, and K. (Kyōhei) Fujimoto, *Small Antennas : Miniaturization Techniques Applications*. McGraw-Hill, 2010.

[139] S. Caizzone and A. Dreher, “An Uncoupled Rematching Technique for Coupled Receive Arrays,” in *Microwave Conference (GeMIC)*, 2014, pp. 1–3.

[140] H. Y. Yuan *et al.*, “Dual-Band Dual-Polarized Microstrip Antenna for Compass Navigation Satellite System,” *Prog. Electromagn. Res. C*, vol. 30, pp. 213–223, 2012.

[141] C. Martel, “Low profile and anti-jam GPS array,” in *IEEE Antennas and Propagation Society, AP-S International Symposium (Digest)*, 2013, pp. 1216–1217.

[142] Maysam Ibraheam, S. Irteza, S. Caizzone, A. Dreher, R. Stephan, and M. A. Hein, “Compact Dual-band Dual-Polarized Antenna Array for Robust Satellite Navigation Receivers,” in *2015 9th European Conference on Antennas and Propagation (EuCAP)*, 2015.

[143] C. Volmer, J. Weber, R. Stephan, K. Blau, and M. A. Hein, “An Eigen-Analysis of Compact Antenna Arrays and Its Application to Port Decoupling,” *IEEE Trans. Antennas Propag.*, vol. 56, no. 2, pp. 360–370, 2008.

[144] X. Shao *et al.*, “Compact Triple Band Antenna Array for GNSS Application,” in *2016 IEEE International Conference on Microwave and Millimeter Wave Technology (ICMMT)*, 2016, pp. 1–3.

[145] A. A. Gheethan, P. A. Herzig, and G. Mumcu, “Compact 2 x 2 Coupled Double Loop GPS Antenna Array Loaded With Broadside Coupled Split Ring Resonators,” *IEEE Trans. Antennas Propag.*, vol. 61, no. 6, pp. 3000–3008, Jun. 2013.

[146] K. N. Paracha *et al.*, “A Low Profile, Dual-band, Dual Polarized Antenna for Indoor/Outdoor Wearable Application,” *IEEE Access*, vol. 7, pp. 33277–33288, 2019.

[147] C. Abdelhamid, M. Daghari, H. Sakli, and C. Hamrouni, “A new UWB-MIMO Multi-Antennas with High Isolation for Satellite Communications,” in *2019 15th International Wireless Communications and Mobile Computing Conference, IWCMC 2019*, 2019, pp. 152–155.

[148] H. Evans, P. Gale, B. Aljibouri, E. G. Lim, E. Korolkeiwicz, and A. Sambell, "Application of Simulated Annealing to Design of Serial Feed Sequentially Rotated 2 × 2 Antenna Array," *Electron. Lett.*, vol. 36, no. 24, p. 1987, 2000.

Appendices

ROGERS
CORPORATION

Data Sheet

RO3200™ Series Circuit Materials

RO3203™, RO3206™ and RO3210™
High Frequency Circuit Laminates

RO3203™, RO3206™ and RO3210™ high frequency circuit materials are ceramic-filled laminates reinforced with woven fiberglass. These materials are engineered to offer exceptional electrical performance and mechanical stability at competitive prices. The RO3200™ series high frequency materials were designed as an extension of the RO3000® series high frequency circuit materials with one distinguishing characteristic - **improved mechanical stability.**

The dielectric constant of RO3203 high frequency circuit materials is 3.02. This, along with a dissipation factor of 0.0016, extends the useful frequency range beyond 40 GHz. The dielectric constant for RO3206 laminate is 6.15 and 10.2 for RO3210 laminate. The dissipation factor for RO3206 and RO3210 laminates is 0.0027.

RO3200 series laminates combine the surface smoothness of a non-woven PTFE laminate, for finer line etching tolerances, with the rigidity of a woven-glass PTFE laminate. These materials can be fabricated into printed circuit boards using standard PTFE circuit board processing techniques as described in the application note, "Fabrication Guidelines for RO3000 Series High Frequency Circuit Materials."

RO3200 series laminates are manufactured under an ISO 9002 certified quality system.

FEATURES AND BENEFITS

Woven glass reinforcement
  - Improves rigidity for easier handling

Uniform electrical and mechanical performance
  - Ideal for complex multi-layer high frequency structures

Low dielectric loss
  - High frequency performance (RO3203™ laminate) can be used in applications exceeding 20 GHz

Low in-plane expansion coefficient (matched to copper)
  - Suitable for use with epoxy multi-layer board hybrid designs
  - Reliable surface mounted assemblies

Excellent dimensional stability
  - High production yields

Economically priced
  - Cost effective volume manufacturing

Surface smoothness
  - Allows for finer line etching tolerances

SOME TYPICAL APPLICATIONS:
- Automotive collision avoidance systems
- Automotive global positions satellite antennas
- Wireless telecommunications systems
- Microstrip patch antennas for wireless communications
- Direct broadcast satellites
- Datalink on cable systems
- Remote meter readers
- Power backplanes
- LMDS and wireless broadband
- Base station infrastructure

Advanced Connectivity Solutions
100 S. Roosevelt Avenue, Chandler, AZ 85226
Tel: 480-961-1382 Fax: 480-961-4533 www.rogerscorp.com

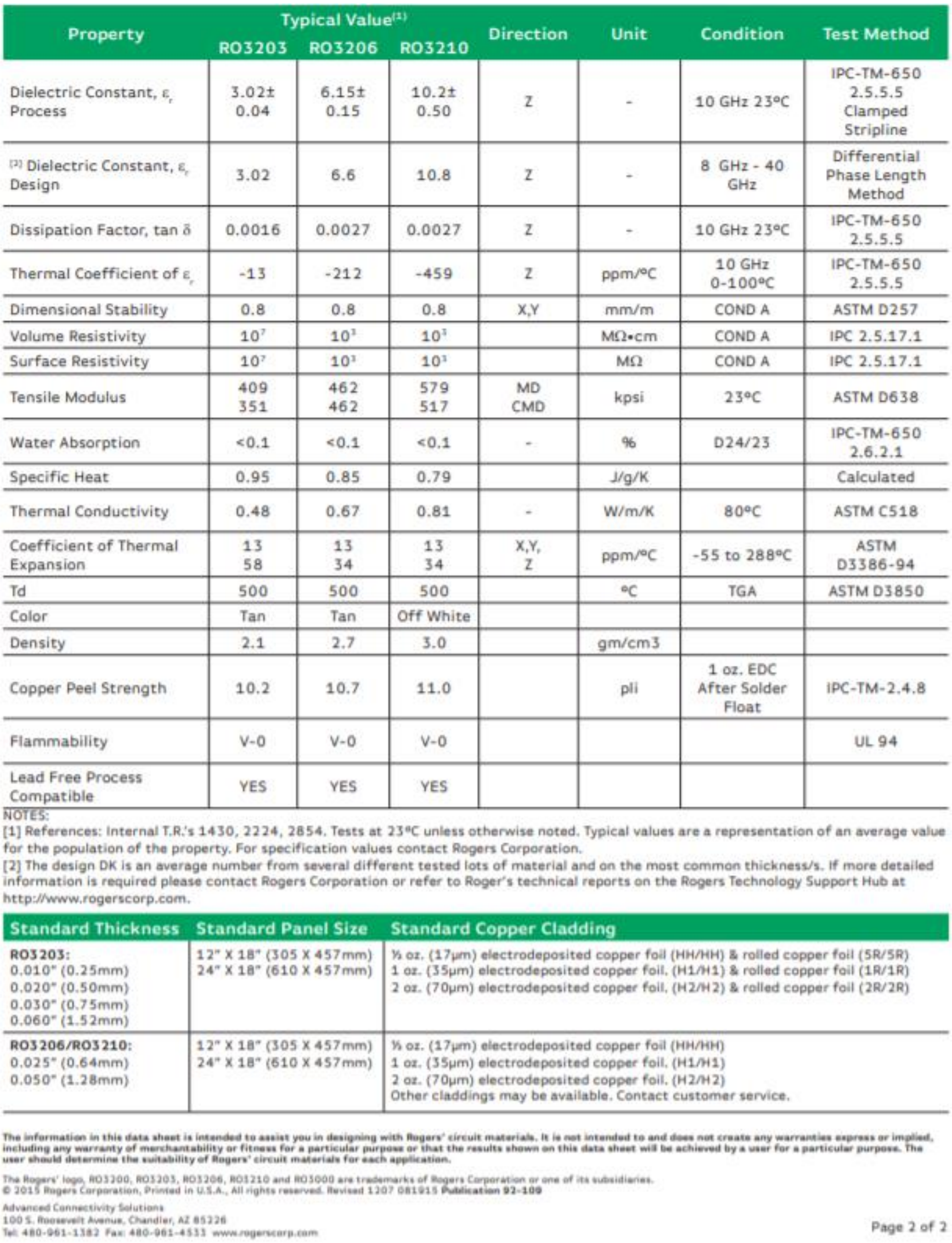

Property	Typical Value[1]			Direction	Unit	Condition	Test Method
	RO3203	RO3206	RO3210				
Dielectric Constant, ε_r Process	3.02± 0.04	6.15± 0.15	10.2± 0.50	Z	-	10 GHz 23°C	IPC-TM-650 2.5.5.5 Clamped Stripline
[2] Dielectric Constant, ε_r Design	3.02	6.6	10.8	Z	-	8 GHz - 40 GHz	Differential Phase Length Method
Dissipation Factor, tan δ	0.0016	0.0027	0.0027	Z	-	10 GHz 23°C	IPC-TM-650 2.5.5.5
Thermal Coefficient of ε_r	-13	-212	-459	Z	ppm/°C	10 GHz 0-100°C	IPC-TM-650 2.5.5.5
Dimensional Stability	0.8	0.8	0.8	X,Y	mm/m	COND A	ASTM D257
Volume Resistivity	10^7	10^3	10^3		MΩ•cm	COND A	IPC 2.5.17.1
Surface Resistivity	10^7	10^3	10^3		MΩ	COND A	IPC 2.5.17.1
Tensile Modulus	409 351	462 462	579 517	MD CMD	kpsi	23°C	ASTM D638
Water Absorption	<0.1	<0.1	<0.1	-	%	D24/23	IPC-TM-650 2.6.2.1
Specific Heat	0.95	0.85	0.79		J/g/K		Calculated
Thermal Conductivity	0.48	0.67	0.81	-	W/m/K	80°C	ASTM C518
Coefficient of Thermal Expansion	13 58	13 34	13 34	X,Y, Z	ppm/°C	-55 to 288°C	ASTM D3386-94
Td	500	500	500		°C	TGA	ASTM D3850
Color	Tan	Tan	Off White				
Density	2.1	2.7	3.0		gm/cm3		
Copper Peel Strength	10.2	10.7	11.0		pli	1 oz. EDC After Solder Float	IPC-TM-2.4.8
Flammability	V-0	V-0	V-0				UL 94
Lead Free Process Compatible	YES	YES	YES				

NOTES:

[1] References: Internal T.R.'s 1430, 2224, 2854. Tests at 23°C unless otherwise noted. Typical values are a representation of an average value for the population of the property. For specification values contact Rogers Corporation.

[2] The design DK is an average number from several different tested lots of material and on the most common thickness/s. If more detailed information is required please contact Rogers Corporation or refer to Roger's technical reports on the Rogers Technology Support Hub at http://www.rogerscorp.com.

Standard Thickness	Standard Panel Size	Standard Copper Cladding
RO3203: 0.010" (0.25mm) 0.020" (0.50mm) 0.030" (0.75mm) 0.060" (1.52mm)	12" X 18" (305 X 457mm) 24" X 18" (610 X 457mm)	½ oz. (17μm) electrodeposited copper foil (HH/HH) & rolled copper foil (5R/5R) 1 oz. (35μm) electrodeposited copper foil. (H1/H1) & rolled copper foil (1R/1R) 2 oz. (70μm) electrodeposited copper foil. (H2/H2) & rolled copper foil (2R/2R)
RO3206/RO3210: 0.025" (0.64mm) 0.050" (1.28mm)	12" X 18" (305 X 457mm) 24" X 18" (610 X 457mm)	½ oz. (17μm) electrodeposited copper foil (HH/HH) 1 oz. (35μm) electrodeposited copper foil. (H1/H1) 2 oz. (70μm) electrodeposited copper foil. (H2/H2) Other claddings may be available. Contact customer service.

Advanced Connectivity Solutions
100 S. Roosevelt Avenue, Chandler, AZ 85226
Tel: 480-961-1382 Fax: 480-961-4533 www.rogerscorp.com

ROGERS
CORPORATION

Data Sheet

RT/duroid® 6006/6010LM

High Frequency Laminates

RT/duroid® 6006/6010LM microwave laminates are ceramic-PTFE composites designed for electronic and microwave circuit applications requiring a high dielectric constant. RT/duroid 6006 laminate is available with a dielectric constant value of 6.15 and RT/duroid 6010LM laminate has a dielectric constant of 10.2.

RT/duroid 6006/6010LM microwave laminates feature ease of fabrication and stability in use. They have tight dielectric constant and thickness control, low moisture absorption, and good thermal mechanical stability.

RT/duroid 6006/6010LM laminates are supplied clad both sides with 1/2 oz. to 2 oz./ft^2 (18 to 70 µm) standard and reverse treated electrodeposited copper foil. Thick aluminum, brass, or copper plate on one side may be specified.

Standard tolerance dielectric thicknesses of 0.010", 0.025", 0.050", 0.075", and 0.100" (0.254, 0.635, 1.270, 1.905, 2.54 mm) are available. When ordering RT/duroid 6006 and RT/duroid 6010LM laminates, it is important to specify dielectric thickness and weight of copper foil required.

Features and benefits:

- High dielectric constant for circuit size reduction
- Low loss. Ideal for operating at X-band or below
- Low Z-axis expansion for RT/duroid 6010LM. Provides reliable plated through holes in multilayer boards
- Low moisture absorption for RT/duroid 6010LM. Reduces effects of moisture on electrical loss
- Tight ε_r and thickness control for repeatable circuit performance

Some Typical Applications:

- Patch Antennas
- Satellite Communications Systems
- Power Amplifiers
- Aircraft Collision Avoidance Systems
- Ground Radar Warning Systems

Advanced Connectivity Solutions
100 S. Roosevelt Avenue, Chandler, AZ 85226
Tel: 480-961-1382 Fax: 480-961-4533 www.rogerscorp.com

Page 1 of 2

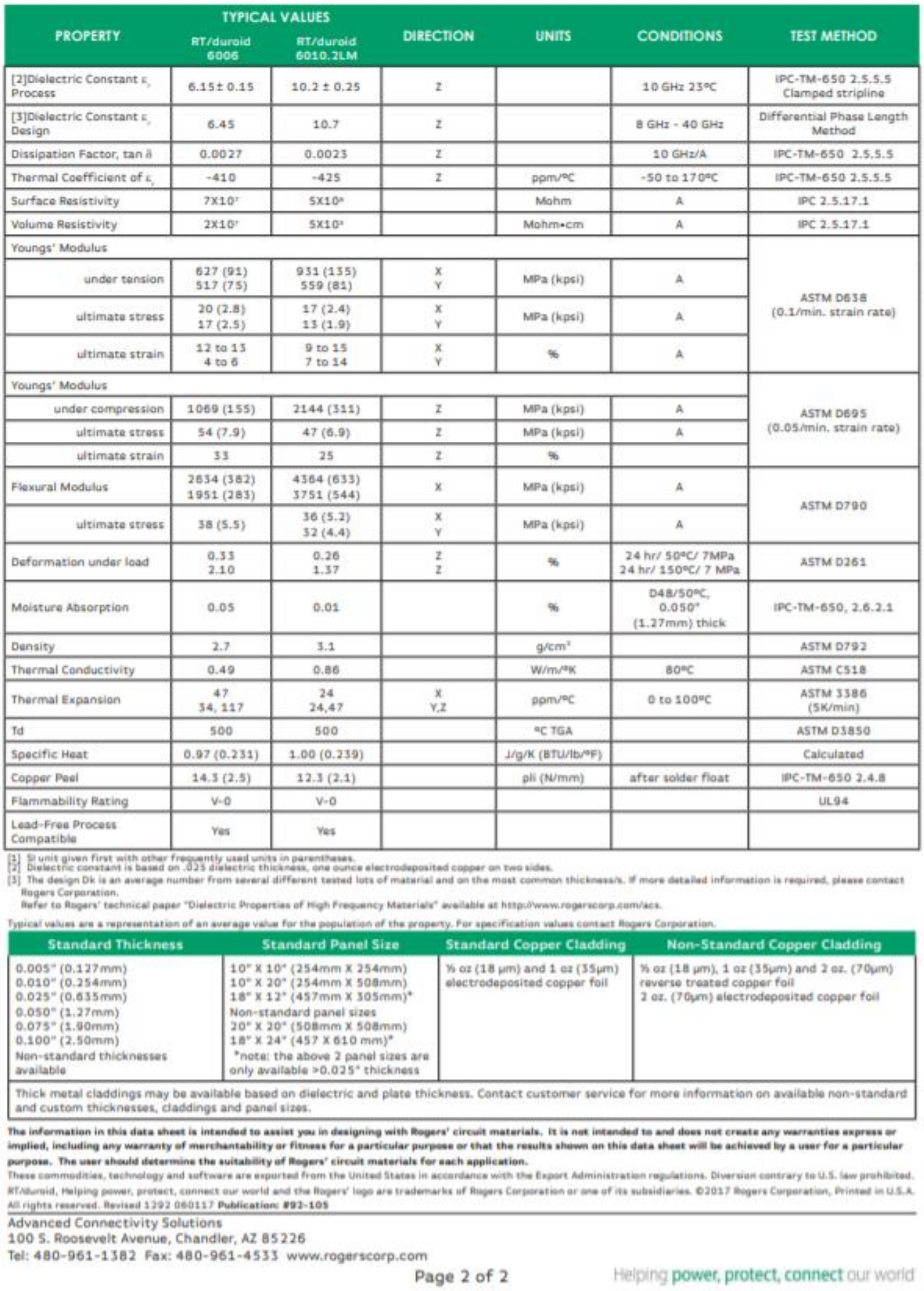

PROPERTY	TYPICAL VALUES		DIRECTION	UNITS	CONDITIONS	TEST METHOD
	RT/duroid 6006	RT/duroid 6010.2LM				
[2]Dielectric Constant ε_r Process	6.15± 0.15	10.2 ± 0.25	Z		10 GHz 23°C	IPC-TM-650 2.5.5.5 Clamped stripline
[3]Dielectric Constant ε_r Design	6.45	10.7	Z		8 GHz - 40 GHz	Differential Phase Length Method
Dissipation Factor, tan δ	0.0027	0.0023	Z		10 GHz/A	IPC-TM-650 2.5.5.5
Thermal Coefficient of ε_r	-410	-425	Z	ppm/°C	-50 to 170°C	IPC-TM-650 2.5.5.5
Surface Resistivity	$7X10^7$	$5X10^6$		Mohm	A	IPC 2.5.17.1
Volume Resistivity	$2X10^7$	$5X10^5$		Mohm•cm	A	IPC 2.5.17.1
Youngs' Modulus						ASTM D638 (0.1/min. strain rate)
under tension	627 (91) 517 (75)	931 (135) 559 (81)	X Y	MPa (kpsi)	A	
ultimate stress	20 (2.8) 17 (2.5)	17 (2.4) 13 (1.9)	X Y	MPa (kpsi)	A	
ultimate strain	12 to 13 4 to 6	9 to 15 7 to 14	X Y	%	A	
Youngs' Modulus						ASTM D695 (0.05/min. strain rate)
under compression	1069 (155)	2144 (311)	Z	MPa (kpsi)	A	
ultimate stress	54 (7.9)	47 (6.9)	Z	MPa (kpsi)	A	
ultimate strain	33	25	Z	%		
Flexural Modulus	2634 (382) 1951 (283)	4364 (633) 3751 (544)	X	MPa (kpsi)	A	ASTM D790
ultimate stress	38 (5.5)	36 (5.2) 32 (4.4)	X Y	MPa (kpsi)	A	
Deformation under load	0.33 2.10	0.26 1.37	Z Z	%	24 hr/ 50°C/ 7MPa 24 hr/ 150°C/ 7 MPa	ASTM D261
Moisture Absorption	0.05	0.01		%	D48/50°C, 0.050" (1.27mm) thick	IPC-TM-650, 2.6.2.1
Density	2.7	3.1		g/cm³		ASTM D792
Thermal Conductivity	0.49	0.86		W/m/°K	80°C	ASTM C518
Thermal Expansion	47 34, 117	24 24,47	X Y,Z	ppm/°C	0 to 100°C	ASTM 3386 (5K/min)
Td	500	500		°C TGA		ASTM D3850
Specific Heat	0.97 (0.231)	1.00 (0.239)		J/g/K (BTU/lb/°F)		Calculated
Copper Peel	14.3 (2.5)	12.3 (2.1)		pli (N/mm)	after solder float	IPC-TM-650 2.4.8
Flammability Rating	V-0	V-0				UL94
Lead-Free Process Compatible	Yes	Yes				

[1] SI unit given first with other frequently used units in parentheses.
[2] Dielectric constant is based on .025 dielectric thickness, one ounce electrodeposited copper on two sides.
[3] The design Dk is an average number from several different tested lots of material and on the most common thickness/s. If more detailed information is required, please contact Rogers Corporation.
Refer to Rogers' technical paper "Dielectric Properties of High Frequency Materials" available at http://www.rogerscorp.com/acs.

Typical values are a representation of an average value for the population of the property. For specification values contact Rogers Corporation.

Standard Thickness	Standard Panel Size	Standard Copper Cladding	Non-Standard Copper Cladding
0.005" (0.127mm) 0.010" (0.254mm) 0.025" (0.635mm) 0.050" (1.27mm) 0.075" (1.90mm) 0.100" (2.50mm) Non-standard thicknesses available	10" X 10" (254mm X 254mm) 10" X 20" (254mm X 508mm) 18" X 12" (457mm X 305mm)* Non-standard panel sizes 20" X 20" (508mm X 508mm) 18" X 24" (457 X 610 mm)* *note: the above 2 panel sizes are only available >0.025" thickness	½ oz (18 µm) and 1 oz (35µm) electrodeposited copper foil	½ oz (18 µm), 1 oz (35µm) and 2 oz. (70µm) reverse treated copper foil 2 oz. (70µm) electrodeposited copper foil
Thick metal claddings may be available based on dielectric and plate thickness. Contact customer service for more information on available non-standard and custom thicknesses, claddings and panel sizes.			

The information in this data sheet is intended to assist you in designing with Rogers' circuit materials. It is not intended to and does not create any warranties express or implied, including any warranty of merchantability or fitness for a particular purpose or that the results shown on this data sheet will be achieved by a user for a particular purpose. The user should determine the suitability of Rogers' circuit materials for each application.

These commodities, technology and software are exported from the United States in accordance with the Export Administration regulations. Diversion contrary to U.S. law prohibited.

Revised 1292 060117 **Publication: #92-105**

Advanced Connectivity Solutions
100 S. Roosevelt Avenue, Chandler, AZ 85226
Tel: 480-961-1382 Fax: 480-961-4533 www.rogerscorp.com

Page 2 of 2

Helping power, protect, connect our world